ELECTROCHEMICAL AND OXYGEN/WATER PERMEATION BEHAVIOR OF FLUORINATED SILOXANE COPOLYMERS SYNTHESIZED VIA INITIATED CHEMICAL VAPOR DEPOSITION

A Thesis Submitted to
The Graduate School of Engineering and Sciences of
Izmir Institute of Technology
In Partial Fulfillment of the Requirements for the Degree of

DOCTOR OF PHILOSOPHY

in Chemical Engineering

by
Gizem CİHANOĞLU

December 2021
İZMİR

ACKNOWLEGEMENTS

I am heartily thankful to my supervisor, Assoc. Prof. Dr. Özgenç EBİL whose knowledge, encouragement, valuable advice and sincerity have broadened my mind and supported me to complete my PhD thesis.

I wish to thank to thesis committee members Prof.Dr. Mustafa DEMİRCİOĞLU, Prof. Dr. Sacide ALSOY ALTINKAYA and Assoc. Prof. Dr. Yaşar AKDOĞAN for their valuable contributions. Throughout the study, I have benefited a lot from their valuable and most constructive suggestions. I also thank for accepting to be in my defense jury. I would like to express my appreciation for Dr. Ogan OCALI for his great help, valuable suggestions, and knowledge. I ought to thank Prof. Dr. Funda TIHMINLIOĞLU and Assist. Prof Dr. Erdal UZUNLAR for letting me use some of the equipment in their laboratories.

I would like to thank Aylin KARA for her help in laboratory work. I wish to thank the Center for Materials Research staff at Izmir Institute of Technology (İYTE-MAM) for their help with SEM analysis.

I would also like to thank all my friends the Department of Chemical Engineering. I am thankful to my friend and lab-mate Merve KARABIYIK for her support and contributions during my experiments. She really became very close to my heart by her love and care.

This journey would not have been possible without the support of my family. First, I would like to express my gratitude to my mother and my father, for their devotion, understanding, and support throughout my life. My special thanks to my husband Aydın CİHANOĞLU for his endless devotion, understanding, and support at the beginning and during my PhD thesis. They always encouraged me in my graduate endeavor.

ABSTRACT

ELECTROCHEMICAL AND OXYGEN/WATER PERMEATION BEHAVIOR OF FLUORINATED SILOXANE COPOLYMERS SYNTHESIZED VIA INITIATED CHEMICAL VAPOR DEPOSITION

Metal-air batteries are considered as one of the best alternatives to current Li-ion batteries with their high energy densities (1000-13000 Wh/kg) also, they are lightweight, cheap and safe. However, secondary alkaline metal-air batteries suffer from catalyst corrosion, anode passivation and corrosion, electrolyte loss and pore clogging leading to performance loss and reduced cycle life. This thesis aims to evaluate the feasibility of highly cross-linked, hydrophobic, and oxygen selective thin homopolymers and copolymers films as potential candidates for Gas Diffusion Layer (GDL) materials in Gas Diffusion Electrodes (GDEs) for alkaline metal-air batteries. Homopolymers of 2,4,6,8-tetramethyl-2,4,6,8-tetravinylcyclotetrasiloxane (V4D4), 2-(perfluorohexyl)ethyl acrylate (PFHEA) and 2-(perfluoroalkyl)ethylmethacrylate (PFEMA) and their copolymers were synthesized via initiated chemical vapor deposition (iCVD).

iCVD deposited fluoropolymer thin films exhibited low water transmission rates and excellent oxygen diffusion with a high oxygen/water selectivity up to 13.6. GDEs with iCVD GDLs exhibited higher oxygen reduction current density (228.2 mA cm^{-2}) when compared to commercial counterparts (132.7 mA cm^{-2}).

In addition, the chemical stability, durability and corrosion protection aspects of these films were investigated by substrate adhesion and immersion tests in organic solvents and NaCl solution. The results of corrosion test together with chemical stability and durability evaluation indicate that iCVD deposited copolymers exhibit excellent adhesion, good solvent resistance and offer an effective physical and chemical protection without the need for surface pretreatment. iCVD copolymer films provide better anti corrosion barrier with lower corrosion efficiency (85-99 %) for metal surface compared to homopolymer counterparts. By combining siloxane and fluorinated matrix, the copolymer films provide enhanced oxygen transport and reduce moisture entrance significantly as a GDLs and also improve physical, chemical, corrosion protection.

Keywords: Metal-Air Batteries, Gas Diffusion Electrode, Gas Diffusion Layer

ÖZET

BAŞLATICILI KİMYASAL BUHAR BİRİKTİRME YÖNTEMİ İLE SENTEZLENEN FLORLU SİLOKSAN KOPOLİMERLERİN ELEKTROKİMYASAL VE OKSİJEN/SU GEÇİRGENLİK DAVRANIŞI

Yüksek enerji ve güç yoğunluğuna sahip, üretim maliyeti ve hafiflik kriterleri ile metal-hava bataryaları uzun vadede enerji depolama sistemlerinde en önemli teknoloji olarak görülmeye başlanmıştır. Sahip olduğu üstün özelliklere rağmen metal-hava bataryalarında ortaya çıkan katalizör kirlenmesi, anot malzemesinin pasivasyonu ve korozyonu, elektrolitin buharlaşması, sistem gözeneklerinin tıkanması gibi ciddi sorunlar batarya performansının düşmesine ve kullanım ömrünün azalmasına neden olmaktadır. Bu tez, metal-hava bataryalarında kullanmak üzere gaz difüzyon elektrotlarında (GDE) gaz difüzyon katmanı malzemeleri için dayanıklılığı yüksek, su geçirmeyen ve oksijen seçiciliği yüksek ince homopolimer ve kopolimer filmlerin yapılabilirliğini değerlendirmeyi amaçlamaktadır.

Başlatıcılı Kimyasal Buhar Biriktirme (BKBB) yöntemi ile 2,4,6,8-tetrametil-2,4,6,8-tetravinilsiklotetrasiloksan (V4D4), 2-(perfloro heksil)etil akrilat (PFHEA) ve 2-(perfloroalkil)etilmetakrilat (PFEMA) homopolimerleri ve kopolimerleri sentezlenmiştir. Sentezlenen filmler düşük su geçirgenliği, yüksek oksijen/su seçiciliği (13.6) ve mükemmel oksijen geçirgenliği sergilemişlerdir. Kaplanan gaz difüzyon elektrotlarının (228,2 mA cm^{-2}) ticari olanlarla (132.7 mA cm^{-2}) kıyaslandığında yüksek oksijen indirgeme akım yoğunluğuna sahip oldukları gösterilmiştir.

Filmlerin organik çözücüler içindeki kimyasal stabiliteleri, dayanıklılıkları, NaCl çözeltisindeki korozyona karşı koruma kapasiteleri ve yüzeye yapışma özellikleri incelenmiştir. Kimyasal stabilite ve dayanıklılık değerlendirmesi ile birlikte korozyon testinin sonuçları, kopolimerlerin mükemmel yapışma özelliği, yüksek solvent direnci sergilediklerini ve herhangi bir işleme gerek olmaksızın etkili bir fiziksel ve kimyasal koruma sunduklarını göstermiştir. Kopolimer filmlerin homopolimer filmlerine kıyasla metal yüzey için düşük korozyon verimliliği (% 85-99) ile etkili bariyer görevi sağladığını gözler önüne koymaktadır.

Bu çalışma, siloksan ve florlu grupların oluşturduğu yapı sayesinde, kopolimer filmlerin yüksek oksijen aktarımı sağladığı, nem girişini önemli ölçüde azaltığını ve ayrıca fiziksel ve kimyasal dayanıma ile birlikte korozyon koruma özelliğini üst seviyeye taşıdığını göstermiştir.

Anahtar Kelimeler: Metal-Hava Bataryaları, Gaz Difüzyon Elektrodu, Gaz Difüzyon Tabakası

TABLE OF CONTENTS

LIST OF FIGURES

Figure **Page**

LIST OF TABLES

CHAPTER 1

INTRODUCTION

In the last century, energy consumption has dramatically increased due to rapid population growth. According to the International Energy Agency, energy consumption will continue to grow approximately 296 % between the years 1970 and 2040. Specifically, energy consumption started at 207 quadrillion Btu (British thermal unit) in the year 1970 and is predicted to reach 820 quadrillion Btu in 2040 (Mainar et al., 2017; Payer, 2014). In this context, worldwide policies closely related to the use of renewals as sustainable energy sources including solar, wind, wave and hydropower must be modified due to the fluctuation of fossil fuel prices and global warming. The demand for renewable energy sources for portable, automotive and grid stationary applications has resulted in increased research on new-generation energy storage and conversion system technologies such as battery technologies as an effective and feasible solution. Lithium-ion batteries (LIBs) are considered as a better energy storage technology for portable consumer electronics due to their power density and cyclability. However, lithium-ion batteries cannot fully satisfy requirements for large-scale applications due to insufficient energy density (200-250 Wh kg^{-1}) and catastrophic thermal runaway (Pan et al., 2018; Mainar et al., 2018; Clark et al., 2020). Therefore, the development of cost-effective and environmentally safe battery technologies for a variety of applications ranging from small portable electronic devices to electric vehicles is also driven by increased public awareness of fire, explosion and toxicity risks associated with today's Li-ion batteries. Metal-air batteries are a promising attractive solution to fulfill such requirements for various applications due to higher energy density compared to other rechargeable batteries. In addition, the paramount feature of metal-air batteries is the open cell structure of cathode which allows the oxygen gas to access from the air, thus providing to reduce both their volume and weight (Clark et al., 2018; Lee et al., 2011).

Metal-air batteries are made of various metal electrodes (e.g., Zn, Li, Mg, Al, Na), electrolyte (aqueous and non-aqueous), and gas diffusion electrode (GDE). The electrochemistry of metal-air batteries is mainly dependent on the metal species for anode material (Li, Ca, Mg, Al, Fe, Zn, etc.). Scientific research has focused on the different

metal species used at anode in metal-air systems. Figure 1.1 compares various metal-air systems in terms of energy density and specific density.

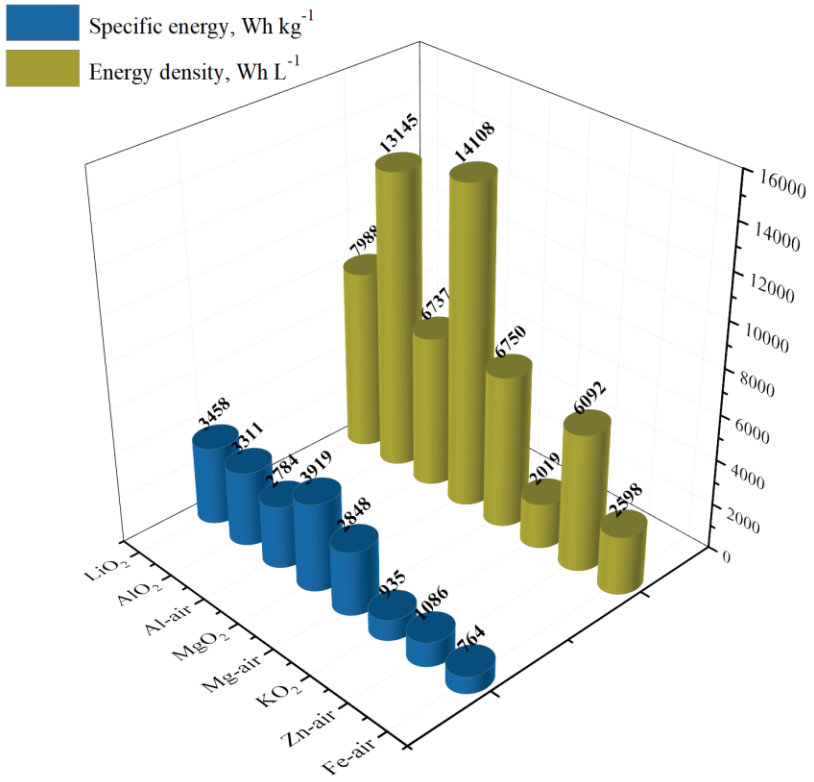

Figure 1.1. Theoretical energy density and specific energy of commonly researched metal-air batteries.

Mg-air battery is considered a promising technology because Mg is the most abundant element in the earth's crust, it has high energy density and reaction activity, and it's lightweight and potentially safe. However, there are still scientific and technical challenges such as corrosion, high polarization, and low Coulombic efficiency, which result in electrochemical instability and low shelf-life (Chen et al., 2015; Rahman et al., 2013; Zhang et al., 2014b). Al-air batteries also captured scientific interest in the past few decades due to Al's high theoretical energy density, specific energy value, abundance and nontoxicity of Al. However, there are also drawbacks of Al-air batteries such as corrosion, inadequate cycling stability and short run time which limit their performance (Davydova et al., 2016; Nestoridi et al., 2008; Li et al., 2007). Li-air batteries have drawn much attention over the past few decades, and their development has become a hot topic since the early 2000s due to their extremely high theoretical specific energy (5200 Wh kg^{-1}). However, lithium-air batteries present inevitable challenges such as high cost (≈60 \$ lb^{-1}), the limitations of lithium metal, and potential safety concerns related to lithium

including thermal instability, which result in explosive reactivity of lithium with air (Mainar et al., 2018; Ma et al., 2015; Peng et al., 2012; Slater et al., 2013). Despite all the above shortcomings of Li-air batteries, they are still in a promising development stage for large-scale practical commercialization. The scientific community has been focused on the innovation and commercialization of Zn-air battery technologies due to abundant global assets of zinc (Zn is the 24th most abundant element in the earth's crust, approximately 300 times more abundant than lithium), economically feasibility (≈0.9 \$ lb^{-1}), and its environmental-friendly value chain (Toussaint et al., 2010; Arise et al., 2011; Polu et al., 2014; Kim et al., 2013). Despite the lower theoretical energy density (1084 Wh kg^{-1}) compared to that of Li-air batteries, Zn-air batteries possess a powerful potential due to all the above paramount features, making them an alternative to Li-air batteries for the huge market of energy demands (Xu et al., 2015).

1.1. Zinc-Air Batteries

Among various metal-air battery technologies, the zinc-air battery stands out as the most promising candidate. The history of Zn-air batteries in which a silver wire was used to act as an air electrode dates back to 1878s. However, the first commercialized primary Zn-air battery was fabricated by George W. Heise and Erwin A. Schumacher for remote railway signaling and navigation aid systems in the 1930s (Harting et al., 2012; Linden and Reddy, 2001). The interest in the concept of the Zn-air battery somewhat diminished between the 1930s and 1960s. In the 1950s, the improvement of the primary Zn-air cell with a real gas diffusion electrode consisting of porous carbon black with suitable electrolyte and nickel current collector was reported by Winckler and co-workers (Winckler et al., 1953). The demands in Zn-air batteries increased with their use in hearing aids in the late 1960s and early 1970s. In recent years, Zn-air batteries have become the standards for many applications such as seismic telemetry, railroad signaling, navigational buoys, remote communications, and even electric vehicles and power grids. Many companies are focusing on the development of a Zn-air battery to replace traditional secondary batteries such as Li-ion and Ni-MH batteries. Several companies (EOS Energy Storage, Fluidic Energy, ZincNyx Energy solution, EDF, ZAF Energy Systems) have begun to commercialize Zn-air technology, but the commercial production of Zn-air batteries remains in the early stage for large-scale applications (Mainar et al., 2017; Pan

et al., 2018). Therefore, the development of Zn-air batteries with outstanding electrochemical performance has become a hot and promising topic in the scientific community for electronic devices, electric vehicles and grid-scale energy storage applications.

1.1.1. Operating Principle of Zn-Air Battery

Zinc-air batteries mainly consist of three parts; a metallic zinc electrode as anode, an electrolyte and an air electrode as cathode, as presented in Figure 1.2. The main parts of Zn-air batteries should fulfill some basic requirements for optimal performance. The zinc electrode should have a sustainable capacity with increasing charge/discharge cycle count. In addition, the electrolyte should have high ionic conductivity, high solubility of zinc salts, high oxygen solubility, low vapor pressure, and excellent contact with the air electrode. This thesis will present the design of an air electrode to overcome the main challenges of air electrodes (Mainar et al, 2017; Pan et al., 2018; Mainar et al., 2018; Clark et al., 2020). An air electrode or Gas Diffusion Electrode (GDE) is made of a porous hydrophobic membrane (Gas Diffusion Layer, GDL), a catalytic layer (active layer) and a current collector as a conductive mesh made of electrically conductive materials like nickel and stainless steel. GDE enables a gas reactant to be in contact with a liquid reaction medium (Park and Park, 2012; Lu et al., 2011). GDL which is described as an oxygen channel, should have high surface area and water permeation resistance (Rocha et al., 2013).

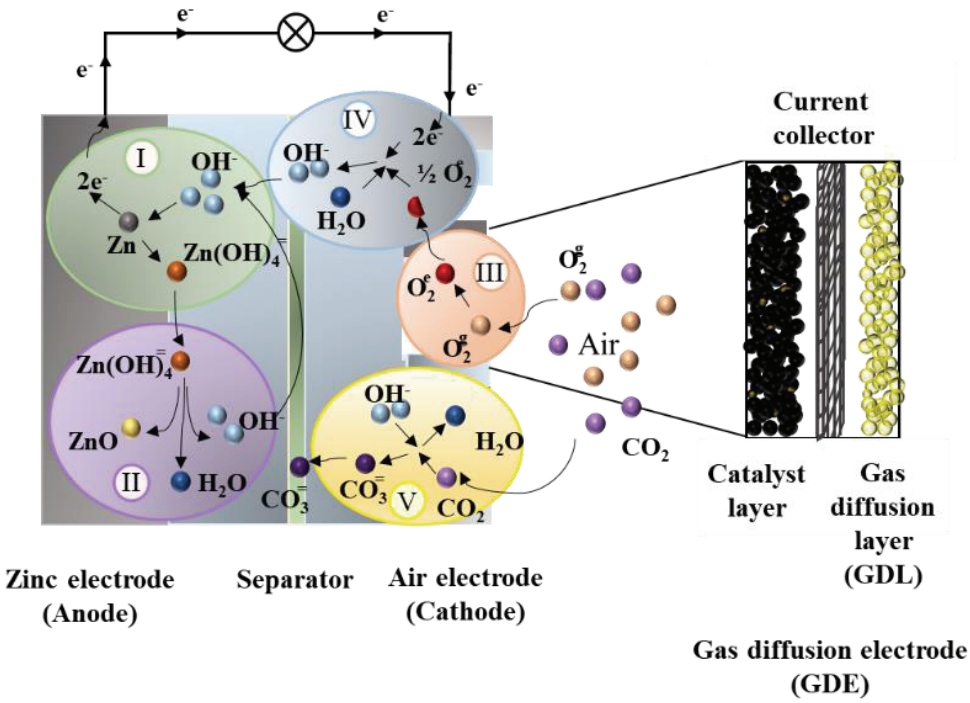

Figure 1.2. Schematic illustration of Zn-air battery and gas diffusion electrode.

In a Zn-air battery, the reactions include zinc oxidation at the anode and oxygen reduction reaction (ORR) at the cathode, as shown in Figure 1.2. During the discharge process, the oxygen from the air spreads into the air electrode driven by the concentration gradient and is reduced to hydroxide ions by ORR. The resultant hydroxide ions in electrolyte both migrate and diffuse from the reaction site to the zinc anode. At the same time, the metallic zinc is oxidized and reacts with the generated hydroxide ions (OH^-) to form zincate ions ($Zn(OH)_4^{2-}$). Next, zincate ions spontaneously decompose to insoluble zinc oxide (ZnO) when these zincate ions reach their supersaturation concentrations (Lee et al., 2011; Gu et al., 2017; Fu et al., 2017a). The electrochemical reactions of anode and cathode can be written as:

The positive electrode : $Zn \longrightarrow Zn^{2+} + 2e^-$ (2.4)

$Zn^{2+} + 4OH^- \longrightarrow Zn(OH)_4^{2-}$ $E^o = 1.25V$ (2.5)

$Zn(OH)_4^{2-} \longrightarrow ZnO + 2OH^- + H_2O$ (2.6)

The negative electrode : $O_2 + 2H_2O + 4e^- \longrightarrow 4OH^-$ $E^o = 0.4V$ (2.7)

Overall reaction : $2Zn + O_2 \longrightarrow 2ZnO$ $E^o = 1.65V$ (2.8)

1.1.2. Challenges, Progress, and Opportunities

Current reviews provide an overview of components, the fundamental mechanism, and future challenges of Zn-air batteries. They also focus on the development of each component of Zn-air batteries (zinc electrode, electrolyte, and especially air electrode) (Read et al., 2003; Sumboja et al., 2017; Hao et al., 2017; Duan et al., 2017; Fu et al., 2017b; Li, 2010; Clark et al., 2019).

A common challenge for Zn-air battery systems is related to the electrolyte which determines its energy and power density. The electrolyte should have a non-flammable nature, low viscosity, high electrochemical and thermal stability, high solubility of zinc salts, and excellent conductivity. Recent publications present the development of alternative electrolytes to inhibit some severe challenges such as the formation of carbonate, and evolution of hydrogen gas that is known as corrosion of zinc anode. One approach is to increase the concentration of potassium hydroxide (KOH) to lead to higher ionic conductivity (Read et al., 2003), to use the zinc salts such as zinc acetate and zinc chloride in KOH electrolyte (Sumboja et al., 2017; Hao et al., 2017; Duan et al., 2017; Fu et al., 2017b), and to add special chemicals containing fluoride (KF), borate (K_2BO_3), phosphate (K_3PO_4), arsenate (K_3AsO_4), and carbonate (K_2CO_3) to reduce zinc solubility in the electrolyte (Li et al., 2010). Another one is to use the aqueous electrolytes with near-neutral pH values ($ZnCl_2$-NH_4Cl, $ZnCl_2$-NH_4OH or $ZnSO_4$ based electrolytes) (Clark et al., 2017; Clark et al., 2019). The application of various surfactants (anodic, cathodic and nonionic) such as dodecyl trimethylammonium bromide (DTAB), sodium dodecyl sulfate (SDS), sodium dodecylbenzene sulfonate (SDBS), and cetyltrimethylammonium bromide (CTAB) is also common as corrosion inhibitors (Hosseini et al., 2018).

Metal electrodes are mainly responsible for the battery capacity. However, the short lifetime of metal-air batteries mainly results from the shape change of zinc electrode, electrode passivation, dendritic growth of zinc, and hydrogen evolution (Geng, 2003; Huang et al., 2008; Yang et al., 2009). These phenomena can induce a decrease in zinc anode stability, volume expansion, reduced cycle life of the cell, early battery failure or capacity loss. The uneven redistribution of zinc on the electrode surface during the charge process causes shape-change of the zinc electrode resulting in loss of usable capacity and dendritic diffusion controlled-deposition causes short-circuit of the

electrodes. Passivation is described as the deterioration of the zinc electrode due to the formation of zinc oxide film as an insulating layer on its surface, leading to the decline of battery capacity, electrolyte depletion, volume expansion, porosity reduction, and conductivity loss (Mainar et al., 2017; Zhang, 1996). Recently, many attempts have been made to overcome these challenges of zinc electrodes and to pinpoint the underlying mechanisms. The majority of these attempts included the use of additives in either electrodes (Geng, 2003; Huang et al., 2008; Yang et al., 2009) or electrolytes (Shivkumar et al., 1995; Adler et al., 1993; Braam et al., 2012; Iwakura et al., 2005), and the use different morphologies for electrodes (Ito et al., 2011; Yuan et al., 2005; Payer and Ebil, 2016).

The battery cycling stability is significantly dependent on a bifunctionally active and durable gas diffusion electrode (GDE). The life-time limitations of secondary metal-air batteries arise from the reversibility and performance of GDE. Oxygen reduction reaction (ORR) and oxygen evolution reaction (OER) take place in GDE during discharge and charge process, respectively. Both ORR and OER suffer from overpotential, thus leading to a decline in cycle count and a battery capacity. The penetration of moisture from the air is a serious challenge for metal-air batteries because it leads to the formation of the insoluble products, reduced oxygen diffusion, and fast cell degradation, thus causing deteriorating cycle life (Cao et al., 2015; Crowther et al., 2011). The electrolyte evaporation and flooding of electrolyte during long-term operation is another serious challenge related to the discharge reactions of GDE due to the decline in ionic conductivity (Fu et al., 2012). The insufficient oxygen transportation and sluggish oxygen reduction reaction in GDE at high current density are also serious issues (Shen et al., 2013; Gu et al., 2017). The search for the ideal gas diffusion electrode has mainly focused on alternatives such as the impregnation of a proton conductor (such as Nafion) into the catalyst layer (Qi et al., 1998; Antolini et al., 1999) and changing chemical composition (Cao et al., 2015) and thickness (Lin and Nguyen, 2005) of the GDL.

An ideal GDL should have high electrochemical conductivity, provide physical and conductive support for the catalyst, exhibit a uniform oxygen diffusion to/from the catalyst and a wet-proof surface (Fu et al., 2017a). Several studies have reviewed the progress GDL materials to achieve long-term stable operation. GDL should have a fast air diffusion with low water diffusion from/to catalyst, high mechanical stability, excellent electrical conductivity, and reliable electrochemical-oxidation stability and chemical durability in harsh environments (Fu et al., 2017a). The selection of specific

material groups for GDL is vital for the overall performance of GDE. One approach is to use polysiloxanes, silicone oils, polyethers and their copolymers due to excellent O_2 solubility and high thermal stability (Crowther and Salomon, 2012). Another materials group is perfluorinated polymers such as fluorinated hydrocarbons, fluorinated polysiloxanes, and fluorinated polysiloxane copolymer with alkyl methacrylates, which provide high chemical and thermal stability, high O_2 solubility, and ability to alleviate electrolyte evaporation and resist electrolyte flooding (Ruan et al., 2018; Xie et al., 2019). Despite the utilization of copolymers of these specific materials for the fabrication GDL, the technical issue of a low-cost and scalable technique for fabrication of GDE is yet to be addressed.

1.2. Motivation

The performance of gas diffusion electrode is crucial for secondary zinc-air batteries as their cycle and service lives are mostly limited by gas diffusion electrodes. Insufficient oxygen input and intrusion of moisture are the main obstacles to achieving the theoretical performance of GDEs. An ideal GDL should not only prevent moisture from entering the GDE but also have high oxygen permeability. Although non-solvent induced phase separation and evaporation deposition are applied to make oxygen selective and hydrophobic GDLs for metal-air batteries, both methods still suffer from poor conformality and limited thickness control. The main motivation in this thesis study was to contribute to the efforts in the development of gas diffusion electrodes using iCVD technique. iCVD technique is used for forming a thin GDL and obtaining conformal films on GDEs with fast air diffusion with low water diffusion from/to catalyst. Furthermore, the constraints listed above regarding the oxygen permeabilities, and hydrophobicity of GDL were also considered.

1.3. Thesis Overview

The main objective of this PhD thesis was to evaluate the feasibility of iCVD fabricated crosslinked hydrophobic copolymer coatings as GDLs in GDEs.

The details of each chapter were described below:

i. In Chapter 2, the information related to gas diffusion electrodes for metal-air battery is presented in detail. The chapter includes overview of GDEs in metal-air battery system, GDE reactions in metal-air battery, and a literature survey related to significant problems of gas diffusion layer on GDEs in batteries.

ii. In Chapter 3, general information on iCVD which is used for the fabrication of GDLs is presented. Research related to the iCVD coatings in wide range of applications was also investigated in detail.

iii. In Chapter 4, thin copolymer films of 2,4,6,8-tetramethyl-2,4,6,8-tetravinylcyclotetrasiloxane (V4D4), 2-(perfluorohexylethylacrylate) (PFHEA) and 2-(perfluoroalkylethylmethacrylate) (PFEMA) synthesized via iCVD is investigated. The main aim is to improve oxygen permeability and hydrophobicity of GDLs for battery applications. The effect of the fluorinated monomer concentration on the oxygen permeability and oxygen diffusion of GDLs is investigated in detail through electrochemical studies.

iv. In Chapter 5, the chemical stability and durability of iCVD homopolymers and copolymers are investigated. The corrosion protection performance of iCVD homopolymer and copolymers on zinc and copper substrates is investigated in detail.

1.4. Contributions to the Literature

The contributions of this PhD thesis to the literature are listed below:

i. Chapter 4: Hydrophobic and oxygen permeable membranes are generally manufactured as gas diffusion layers via either non-solvent induced phase separation (Amici et al., 2016a; Amici et al., 2016b; Cao et al., 2015) or evaporation-deposition (Xie et al., 2019) techniques. These membranes need to be resistant to moisture when exposing atmospheric condition and maintain a thickness less than 1 μm to enhance the mass transfer through the GDE. It is difficult to control the thickness of these membranes. In Chapter 4, for the first time in literature, fluorinated siloxane copolymer poly(V4D4-co-PFHEA) as an alternative to conventional GDLs used in today's alkaline metal-air batteries was fabricated via iCVD method. The study demonstrates that iCVD GDLs with improved oxygen mass transport, extremely low water vapor transmission and

excellent chemical stability will enable the fabrication of gas diffusion electrodes with enhanced electrochemical performance for primary and secondary metal-air batteries.

ii. Chapter 5: In recent years, research on polymer coatings for protecting metal surfaces against physical damage and corrosion attracted interest for functional films for sensing, biomedical applications, encapsulation, dielectric barrier layers, hydrophobic surfaces, etc. A trade-off was observed between improved hydrophobicity and robustness. In Chapter 5, iCVD process to finely control of process parameters to tailor the chemical composition, physical and chemical properties of fluorinated siloxane copolymer for corrosion protection of metals was investigated in detail. This work is a part of our ongoing experimental and computational research on functionalized polymer thin films fabricated via iCVD and addresses synthesis, characterization, and evaluation of corrosion protection performance using specific surface analytical techniques. It is the first study in the literature that uses iCVD fabricated coatings for corrosion protection and the first study that demonstrates the feasibility of fluorinated siloxane copolymer poly(V4D4-co-PFHEA) as an effective physical and chemical protected alternative.

CHAPTER 2

GAS DIFFUSION ELECTRODES

In this chapter, the effect of moisture and CO_2 intake from air on metal-air batteries is evaluated. The chapter contains a brief overview of GDEs, and a literature survey related to significant problems of GDEs in metal-air batteries and the use of oxygen selective membranes as GDL.

2.1. General View for Gas Diffusion Electrodes

Electrical-energy-storage systems play an important role in a wide range of applications to balance supply with energy demands. Metal-air batteries are considered as one of the most promising energy storage options for grid-scale energy storage and support renewable energy sources. In recent years, metal-air batteries have gained a lot of attention due to their energy densities, theoretical specific capacities, lower materials cost and high recyclability (Lee et al., 2011; Wang et al., 2014; Ugalde and Nauib, 2017). Lithium-air battery, for instance, is one of the most attractive energy storage options due to high theoretical energy density (5,200 Wh kg^{-1} including oxygen; 11,140 Wh kg^{-1} excluding oxygen) which may be convenient for providing enough energy storage capability for electrical devices to drive more than 500 miles (per charge) compared to gasoline vehicles (Ma et al., 2015; Lu et al., 2015).

A conventional state of the art GDE in a metal-air battery consists of a gas diffusion layer (GDL, porous hydrophobic membrane), a current collector which can also act as support, and catalysts where oxygen reduction reaction takes place (Sun et al., 2016). Figure 2.1 shows the main reactions for discharge process in a zinc-air battery. The reaction mechanism in zinc-air cells includes; (I) dissolution of Zn, (II) the precipitation of ZnO, (III) oxygen absorption into the electrolyte, (IV) reduction of oxygen, (V) dissolution of carbon dioxide and carbonate formation.

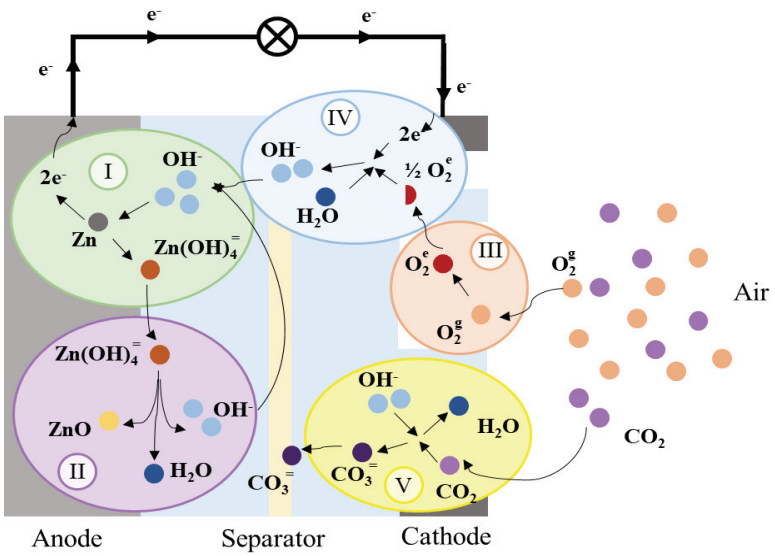

Figure 2.1. Reaction mechanism of zinc-air battery system.

In a Zn-air battery, the reactions includes the zinc oxidation at the anode and oxygen reduction reaction (ORR) at the cathode, as shown in Figure 2.1. During the discharge process, the oxygen from the air spreads into the air electrode driven by the concentration gradient and is reduced to hydroxide ions by ORR. The resultant hydroxide ions in electrolyte migrate from the reaction site to the zinc anode. At the same time, the metallic zinc is oxidized and reacts with the generated hydroxide ions (OH^-) to form zincate ions ($Zn(OH)_4^{2-}$). Next, zincate ions spontaneously decompose to insoluble zinc oxide (ZnO) when these zincate ions reach their supersaturation concentrations (Lee et al., 2011; Gu et al., 2017; Fu et al., 2017a). The electrochemical reactions at anode and cathode can be written as:

$$Zn + 4OH^- \rightleftharpoons Zn(OH)_4^{=} + 2e^- \quad (2.1)$$

Equations (2.2)-(2.5) explain how the overall reaction is summarized by adding order reactions.

$$Zn + OH^- \rightleftharpoons ZnOH + e^- \quad (2.2)$$

$$ZnOH + OH^- \rightleftharpoons Zn(OH)_2^- \quad (2.3)$$

$$Zn(OH)_2^- + OH^- \rightleftharpoons Zn(OH)_3^- + e^- \quad (2.4)$$

$$Zn(OH)_3^- + OH^- \rightleftharpoons Zn(OH)_4^{=} \quad (2.5)$$

The zinc oxide precipitation starts when the solubility limit of zincate is reached. Due to convective forces, this process occurs near the bottom of the zinc electrode, leading to non-uniform electrode thickness. At the same time, the solubility of zincate in

electrolyte close to the surface of the zinc electrode is exceeded and then barrier (passivation) layer can be formed.

$$Zn(OH)_4^{=} \rightleftharpoons ZnO + H_2O + 2OH^- \quad (2.6)$$

Oxygen from air is dissolved at the gas-liquid phase boundary in the gas diffusion electrode, and then dissolved oxygen is transformed to hydroxide at the cathode surface. The kinetics of oxygen reduction is dependent on the catalyst used.

$$O_2^g \rightleftharpoons O_{2.}^e \quad (2.6)$$

$$0.5\ O_{2.}^e + H_2O + 2e^- \rightleftharpoons 2OH^- \quad (2.7)$$

Carbonate formation occurs as a result of reaction of carbon dioxide from air with hydroxide ions.

$$CO_2 + 2OH^- \rightleftharpoons CO_3^{=} + H_2O \quad (2.8)$$

$$CO_2 + OH^- \xrightarrow{k_{OH}} HCO_3^- \quad (2.9)$$

$$HCO_3^- + OH^- \rightleftharpoons CO_3^{=} + H_2O \quad (2.10)$$

The formation of carbonate results in lower battery performance due to reduced hydroxide concentration in aqueous electrolyte, and accelerate passivation layer formation.

The reduction mechanism at the catalyst-electrolyte boundary in Li-O_2 cell is shown in Figure 2.2. In the first step, oxygen is dissolved in the electrolyte solution at the electrode surface to form LiO_2. There is an equilibrium between LiO_2 dissolved in the electrolyte solution and LiO_2^* adsorbed on the electrode surface (Johnson et al., 2014; Aurbach et al., 2016).

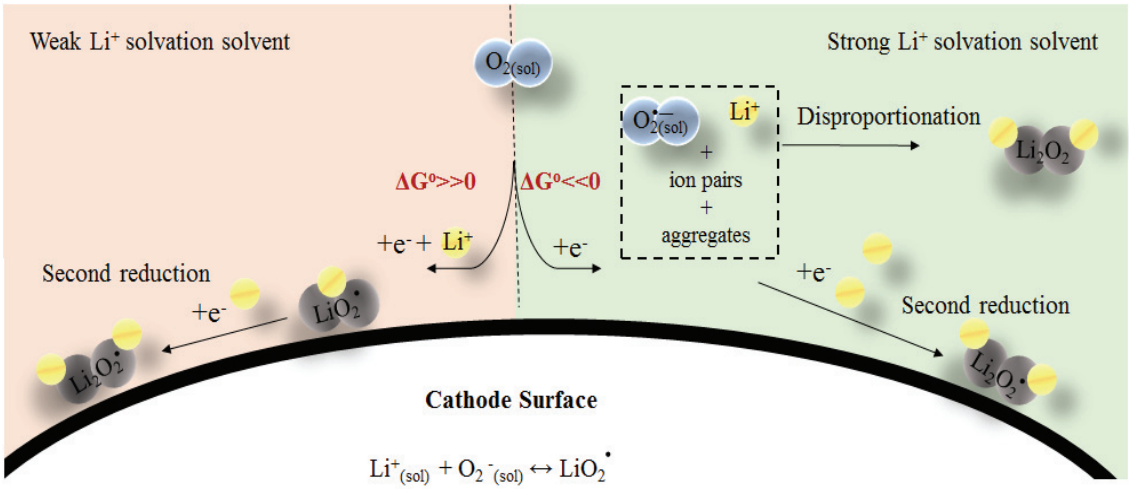

Figure 2.2. Reduction mechanisms in a Li-O_2 cell at low over potentials.

The process at electrolyte and electrode surface in Li-O_2 cells takes place as follows (Johnson et al., 2014; Aurbach et al., 2016):

Solution mechanism;

$$Li^+_{(sol)} + e^- + O_{2(sol)} \rightleftharpoons Li^+_{(sol)} + O_2^-{}_{(sol)} \quad (2.11)$$

$$2(Li^+_{(sol)} + O_2^-{}_{(sol)}) \rightleftharpoons Li_2O_2 + O_2 \quad (2.12)$$

$$2Li^+_{(sol)} + O_2^-{}_{(sol)} + e^- \rightleftharpoons Li_2O_2 \quad (2.13)$$

Surface mechanism;

$$Li^+ + e^- + O_{2(sol)} \rightleftharpoons LiO_2^{\bullet} \quad (2.14)$$

$$Li^+ + LiO_2{}^{\bullet} + e^- \rightleftharpoons Li_2O_2{}^{\bullet} \quad (2.15)$$

$$2LiO_2^{\bullet} \rightleftharpoons Li_2O_2^{\bullet} + O_2 \quad (2.16)$$

The electrochemical performance is dependent on the design of electrode in hydrogen fuel cells and metal-air batteries. In the hydrogen fuel cells, H^+ protons from electrolyte reacts with oxide ions at catalyst surface in order to form water, whereas in metal air batteries M_2O_2 is formed by the reaction between M^+ ions from electrolyte and oxide ions at air cathode surface. However, there is a striking difference in the reduction product and the reduced product of oxygen between metal-air batteries and hydrogen fuel cells. Non-catalyzed reduction reactions of oxygen are possible for metal air batteries, but reduction reactions of oxygen take place with catalysts in fuel cells. The accumulation of the reduced product of oxygen in metal-air batteries is observed in the pores of the cathode electrode, while the product in the fuel cells is not accumulated due to water transformation (Lee et al., 2011).

2.1.1. Problems with Gas Diffusion Electrodes

There are critical challenges related to air cathode in metal-air batteries limiting their effective use in a wide range of applications. Catalyst loss, catalyst poisoning or carbon corrosion, water intake from air, blockage and leakage of electrolyte after hundreds of charge/discharge cycles Carbon dioxide capture, insufficient oxygen input, O_2 transport limitations, and charge transport limitations are important factors for the cycling-life of metal-air batteries. A GDL must have a high oxygen permeability and low water vapor transfer rate to prevent degradation in cell power capability and service life. Catalyst poisoning, flooding and carbonate formation still remain as main obstacles for achieving theoretical performance of air electrodes (Lee et al., 2011; Zhang et al, 2004).

The flooding of the air electrode is caused by slow penetration of electrolyte into GDL. The diffusion resistance of oxygen is thus increased, resulting in a lower oxygen reduction rate. One approach to solve this problem is to use hydrophobic materials such as polytetrafluoroethylene powder as an additive. Dissolution of the catalyst especially at high current densities during charging is another issue for GDEs. In catalyst layer, hydroxyl ions are oxidized, forming oxygen which leads to a local pressure buildup within the air electrode, and in turn mechanical degradation of air electrode. Another problem is the formation of carbonate and pore plugging within the air electrode due to reaction of carbon dioxide with alkaline solution (Pei et al., 2014).

In general, the discharge product of metal-air batteries is considered as an electronic insulator, insoluble or very sparingly soluble in organic liquid-based electrolytes and a strong oxidizer. Stability in an alkaline environment, high gas permeability, good electronic conductivity, good elastic compression and controlled porous structure are crucial factors for the performance and service-life of gas diffusion electrode. Therefore, an air electrode has to be designed to provide an adequate electronic conductivity and M^+/O_2 transport, be resistant to the M_2O_2–induced oxidation (M: metal) and avoid to preform parasitic processes related to electrolyte and M_2O_2 (Aurbach et al., 2016). There are many studies aimed at improving GDE performance by using (i) different support materials (carbon paper or carbon cloth) with various morphologies, (ii) different bifunctional catalysts (Mn_xO_y, CeO_2, Ag-based, Pt alone, Pt with other metals), (iii) chemically stable polymeric materials (polyethylene, polyvinylidene fluoride, polytetrafluoroethylene and Nafion as impregnation of a proton conductor), (iv) different binder materials, (v) various GDE microstructures, and (vi) different electrode preparation procedures (Giorgi et al., 1998; Sasikumar et al., 2004; Zhang et al., 2004; Indayaningsih et al., 2016; Sun et al., 2016).

2.1.2. Challenges for Performance of Metal-Air Batteries

The unique advantage of metal-air batteries is the supply of unlimited amount of oxygen from the ambient air. However, the intake of other constituents of air (N_2, Ar, H_2O and CO_2) may prevent achieving theoretical performance of air electrodes. Although inert gases such as N_2 and Ar are more abundant in the atmosphere, the side electrochemical reactions on the air cathode (for example, $3Li + ½\ N_2 \rightarrow Li_3N$) with these gases are eliminated due to its theoretical formation of Li_3N is approximately 0.444V

[$\Delta_f G^o$ (Li_3N) = -10.25 kcal/mol/Li]. In contrast, CO_2 composition in the atmosphere accounts for approximately 0.035% rather than N_2 (78%), but it is thermodynamically possible to form carbonate species in the presence of CO_2 in the air cathode. The electrochemical decomposition of discharge product with carbonate form (i.e. Li_2CO_3) is chemically more stable compared to the other discharge product (i.e. Li_2O_2) according to their standard Gibbs free energies of formation [$\Delta_f G^o$ (Li_2CO_3) = -135.30 kcal/mol Li; $\Delta_f G^o$ (Li_2O_2) = -68.26 kcal/mol Li] (Lim et al., 2013; Sahapatsombut et al., 2014; Geng et al., 2016).

While the introduction of small amount of CO_2 into GDE can increase the specific discharge capacity of an metal-air battery, carbonates formed from the decomposition of cathode/electrolytes during battery operations cause adverse effects such as pore blocking, electrolyte loss, deterioration of the cell capacity etc. (Takechi et al., 2011; Zhu et al., 2017a). Preventing moisture intake from ambient air must be considered as another significant challenge for metal-air batteries as it leads to a degradation in cell power capability, severe safety issues and cycle life (Lee et al., 2011; Zhang et al., 2004). A promising method to avoid moisture intake is to use an O_2-selective water barrier membrane with greater oxygen solubility and/or diffusivity water. However, the separation of O_2 and H_2O is very challenging for such a membrane with Knudsen diffusion due to the higher diffusivity and smaller kinetic diameter of H_2O molecule (2.65 Å for H_2O vs. 3.46 Å for O_2). The diffusion of H_2O molecule is faster than that of O_2 molecule in porous membrane as the Knudsen separation factor of O_2/H_2O (K_{O_2/H_2O}=√(18/32) =0.75) is less than 1 (Szostak, 1992; Zhang et al., 2010a; Shao et al., 2013).

In the following sections, a brief information on the effects of moisture (water) and carbon dioxide on the performance of metal-air batteries, especially Li-air battery, is given in detail.

2.2. Oxygen Selective Membrane in Metal-Air Batteries

One of the methods tried in literature to overcome water vapor and CO_2 intake from air is the incorporation of mixed matrix membranes for gas diffusion layer which reduce moisture and CO_2 intake and also possess high O_2 selectivity (Zhang et al., 2010a; Sahapatsombut et al., 2014; Amici et al., 2016a). The porous membranes such as Teflon,

Celgard or polyhethylene sulfide (PPS) or membranes including perfluorocarbons, ethers, polyfluoroethers, polysiloxanes, acrylmethacrylates, silicone rubbers, or the functional groups of $–NH_2$, -OH, -C=O are favorable for preventing CO_2 problem by adsorbing CO_2. Additionally, the intrinsic hydrophobic behavior for membrane seems to be a promising factor in air cathode for reducing the moisture diffusion (Crowther et al., 2011; Cao et al., 2015). The effect of various parameters of Li-air batteries (the selection of gas-diffusion membrane, preparation of air electrodes, and battery-assembly methods) on their performances was examined by Zhang et al. (Zhang et al., 2010b). Li-air cell with commercial oxygen-diffusion membrane and a moisture barrier (DuPont Melinex® 301H) was found to be better than the other ones with high density polyethylene (HDPE) membrane, and PTFE membrane in terms of discharge capacity and specific energy. The results indicated that its discharge capacity (Zhang et al., 2010b). Li-air batteries with O_2-selective membranes were tested in ambient condition with 20-30% relative humidity by Zhang et al. (Zhang et al., 2010a). The effect of porous substrates (fresh porous metal sheet, surface-modified porous metal sheet, silicate membrane-coated porous metal sheet and commercial PTFE film) and supporting material for catalyst (Darco® G-60 activated carbon, DC, or Ketjen black EC600JD carbon, KB) and type of silicone oils with different viscosity (Dow Corning 200 fluids, polydimethylsiloxane-PDMS, or Shin-Etsu DM-fluid (dimethylpolysiloxane)) on the performances of Li-air batteries were investigated. It was concluded that the fresh metal substrate exhibited a high air permeance of $2.85x10^{-4}$ mol $m^{-2}Pa^{-1}s^{-1}$ while silicone oil loaded into porous metal sheet had air permeance of 1.62×10^{-6} mol $m^{-2}Pa^{-1}s^{-1}$. GDE including immobilized liquid oil membrane with KB was found to improve specific energy, discharge capacity and discharge time compared to GDE with PTFE membrane. In addition the performance of battery with ketjen black carbon was better than that with Darco® G-60 activated carbon (Zhang et al., 2010a). Crowther et al. reported the influence of O_2-selective membrane thickness on electrochemical performance for Li-air batteries (Crowther et al., 2011). The oxygen selective membranes consisting of polysiloxane and methacrylate-polysiloxane copolymers with various thicknesses were compared. The discharge capacity of polysiloxane-methacrylate membrane (on polyphenylene sulfide, PPS) with 330 μm of thickness (947 mAh g^{-1}) was found to be better than that with 432 μm of thickness (818 mAh g^{-1}) at 0.1 mA cm^{-2} (Crowther et al., 2011). In a study by Fu et al., highly conductive polyaniline (PANI) membrane as waterproof barrier was synthesized to evaluate the electrochemical performance of Li-air batteries in high relative humidity conditions (Fu et al., 2012). The

results showed that the cell without PANI-doped membrane delivered a capacity of 1700 mAh g^{-1} in high humidity condition (RH>20%), while the capacity of the cell with PANI-doped membrane was measured as 2453 mAh g^{-1}. It was also found that PANI membrane protected air electrode and showed more stable interfacial impedance (Fu et al., 2012). Poly(vinylidene fluoride co-hexafluoropropylene) (PVDF-HFP)-based membranes were developed by Amici et al. (Amici et al., 2016a). The results indicated that as-prepared membrane was a good compromise with acceptable oxygen diffusion (the water permeability of 28.875 g $m^{-2}day^{-1}$) and oxygen permeability (0.487 Barrer). The battery assembled with the membrane exhibited higher discharge capacity (640 mAh g^{-1}) in comparison to that without membrane (220 mAh g^{-1}) (Amici et al., 2016a). In another study, Amici et al. proposed a highly hydrophobic oxygen selective membrane based on a dextrin-nanosponge (NS) incorporated PVDF-HFP polymer to prevent the moisture from air (Amici et al., 2016b). The incorporation of the NS into PVDF-HFP membrane led to higher O_2/H_2O selectivity (α_{O_2/H_2O}= 9.078) when compared to Si oil-based into the same polymer membrane (α_{O_2/H_2O}= 0.564). As-prepared membrane exhibited a high O_2 permeability of 3.147 Barrer which resulted in 145 charge/discharge cycles at a curtailed capacity of 100 mAh/g for 1450 h cell operation (Amici et al., 2016b). Despite many studies focused on oxygen selective water barrier membrane, there are only a few studies in literature related to incorporation of materials with CO_2 capture capability in GDEs for alkaline metal-air batteries. In one of these studies, Cao and co-workers fabricated a novel mixed matrix membrane (MMM) by incorporating polydopamine-coated MOF crystals of CAU-1-NH_2 into PMMA to enhance O_2 selectivity of air cathode for Li-air batteries (Cao et al., 2015). In that study, the effect of MMM and polydopamine on electrochemical performance for Li-air cell was investigated. The O_2/CO_2 ideal selectivity of the MMM with and without coating PDA on the MOF were found to be α= 5.5, P_{CO2} = 0.38x10^{-8} mol $m^{-2}Pa^{-1}s^{-1}$ and α= 2.7, P_{CO2} = 0.78x10^{-8} mol m^{-2} $Pa^{-1}s^{-1}$, respectively. In addition, the capacity of the Li-air battery with MMM layer was found to be higher (1480 mAh g^{-1}) than that without MMM layer (1100 mAh g^{-1}) and electrode with MMM layer showed better reversibility and superior stability.

CHAPTER 3

INITIATED CHEMICAL VAPOR DEPOSITION TECHNIQUE

In this chapter, general information on iCVD technique used to fabricate GDLs for battery systems are presented. Studies on iCVD coatings in wide range applications are also examined in detail. Additionally, the research on fluorinated and siloxane polymer films are presented.

3.1. Initiated Chemical Vapor Deposition (iCVD)

Chemical Vapor Deposition (CVD) is a versatile technique for surface engineering in semiconductor industry, electronics, biotechnology, nanotechnology, optoelectronics, photonics, microfluids, sensing, and separations. CVD systems have been used to fabricate solid thin-film coatings to a variety of surfaces and produce high-purity bulk materials and powders as well as composite materials by infiltration techniques.

CVD systems have advantages over physical vapor deposition (PVD) systems such as sputtering or evaporation in which solid or liquid source is converted into vapor phase to form atom or molecules under a vacuum and deposited on the substrate. One of the advantages is capability for obtaining a conformal coverage with uniform thickness profile on complex geometries. CVD can also provide higher material purity in deposited films due to ultra-pure gaseous precursors. Some CVD methods do not need high vacuum levels and can handle substrates in larger batches than PVD methods (Park and Sudarshan, 2001; Rocket 2008; Gleason, 2015). The successful films deposition via CVD is usually associated with medium to high temperatures. However, traditional CVD techniques are not compatible with the deposition of polymeric film on the temperature sensitive substrate such as polymer, papers or fabrics. Therefore, iCVD is an excellent alternative to overcome this issue (Parker et al., 2011).

3.1.1. Mechanism of iCVD

iCVD method is a promising pathway for the synthesis and deposition of polymer thin films with its ability to provide conformal and pinhole-free coatings with a high deposition rate and nanoscale thickness control in a solvent-free process and low thermal budget (Yang et al., 2011; Gleason, 2015). A typical iCVD system includes vapor delivery, reaction chamber, temperature control, pressure control, exhaust management, vacuum pump system, and process monitoring components.

iCVD follows the same kinetics as free radical polymerization. The free radicals attack active monomer molecules that carry unpaired electrons. Next, the activated monomer attacks other unactivated monomers. The unpaired electron is transferred to the growing chain end to complete free radical polymerization. Free radical polymerization includes initiation, propagation, and termination steps. In the initiation step, the reactive molecules with active site are formed, and the initiator is decomposed in the gas phase. Free radicals and monomer molecules are adsorbed on cooled substrate surface, and monomer radicals form free radicals. The initiation process occurs on the substrate surface, not in the gas phase (Lau and Gleason, 2006). In the propagation step, activated monomer molecules attack other monomers with no active sites (chain growth). The unpaired electron is delivered to the chain end. The transfer of this electron is continuous during the chain growth process on the substrate surface. The propagation process occurs by adding a monomer unit to the polymer chains (Allcock et al., 2003; Lau and Gleason, 2006). In the termination step, the polymer is formed by capping the active polymer chain ends. The termination process may occur either by adding free radicals to the growing chain ends or by bonding two polymer chains. All free radical polymerization steps take place on the substrate surface except initiator decomposition that takes place either via thermal or light induced decomposition in the gas phase to form free radicals (Lau and Gleason, 2006).

As shown in Figure 3.1, the mechanism of iCVD involves the following four main steps (Gleason, 2015):

- Transport of precursors in vapor phase; monomer and initiator into reaction chamber
- Adsorption of monomer onto cooled substrate surface
- Decomposition of initiator over resistively heated filaments to form free radicals

- Polymerization via initiation, propagation and termination at the substrate surface

The free radical polymerization mechanism of iCVD system are given below where R represents the radical, M is the monomer, and I is the initiator.

Gas phase

Initiator decomposition: $I_{(g)} \xrightarrow{k_d} 2R\cdot_{(g)}$ (3.1)

Gas-to-surface processes

Primary radical adsorption: $R\cdot_{(g)} \xrightarrow{k_{ad.R}} R\cdot_{(ad)}$ (3.2)

Monomer adsorption: $M\cdot_{(g)} \xrightarrow{k_{ad.M}} M\cdot_{(ad)}$ (3.3)

Surface reactions

Initiation: $R\cdot_{(ad)} + M_{(ad)} \xrightarrow{k_i} M_I\cdot_{(ad)}$ (3.4)

Propagation: $M_n\cdot_{(ad)} + M_{(ad)} \xrightarrow{k_p} M_{n+1}\cdot_{(ad)}$ (3.5)

Termination: $M_n\cdot_{(ad)} + M_{an}\cdot_{(ad)} \xrightarrow{k_t} M_{a+m}\cdot_{(ad)}$ and $M_{a+m}\cdot_{(ad)}$ (3.6)

Primary radical recombination: $R\cdot_{(ad)} + R\cdot_{(ad)} \xrightarrow{k_1''} R_{2(ad)}$ (3.7)

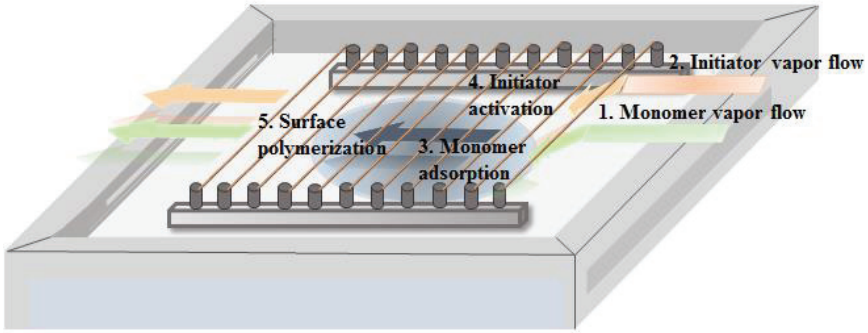

Figure 3.1. General process in iCVD system.

3.2. iCVD Coatings

There are many studies in literature where antifouling, self-cleaning, antimicrobial, and stimuli-responsive polymer thin films fabricated via iCVD were evaluated. These thin-films are suitable for many applications such as drug delivery, biomedical implants, tissue engineering, biosensor fabrication and sea water desalination etc. and there are excellent literature sources providing details for these applications (Gleason, 2015). Below, a brief literature survey of related to iCVD polymeric materials used in this study is given.

3.2.1. Organosilicon Polymers

iCVD method is an excellent alternative pathway for fabrication of semiconductor materials as dielectric films in integrated circuits and as biocompatible coatings in medical implants, as barrier films for food packaging. In semiconductor industry, the interlayer dielectric (ILD) materials have been attracting interest to meet the demands of ever developing integrated circuit design. ILD materials with low dielectric constant, k, lead to reduced power consumption, lower cross talk and delay time of signal distribution and heat spread. Several strategies on this topic using organosilicon polymer have been described. Organosilicon polymers are identified as a class of low-k materials with attractive electrical, mechanical and thermal properties. In addition, copolymerization of fluoropolymers with silicon-based polymers can improve chemical stability of the deposited layer due to C–F and Si–O bonds.

Among many others, poly(tetravinyltetramethylcyclotetrasiloxane) (poly(V4D4)) is considered as one of the best candidates for barrier application. Many approaches have been employed to fabricate robust polymer films consisting of organosilicon crosslinked networks via iCVD methods. The fabrication of tetravinyltetramethyl cyclotetrasiloxane films using iCVD method was reported by Trujillo and co-workers to improve mechanical properties of films and to reduce its dielectric constant (Trujillo et al., 2010). The results indicated that iCVD method is capable of producing low-k films with high mechanical and electrical properties (Trujillo et al., 2010). Yoo investigated stacked polymer films composed of poly(1,3,5,7-tetravinyl-1,3,5,7- tetramethylcyclotetra siloxane) (poly(V4D4)) layer and a poly(1H,1H,2H,2H-perfluorodecylacrylate) (poly(PFDA))

layer for robust superhydrophlobic fabrics (Yoo et al., 2013). It was pointed out that the durability of mechanical and chemical stresses of superhydrophobic fabric undergoes positive change by adding poly(V4D4) layer that strongly binds superhydrophobic poly(PFDA) in iCVD method (Yoo et al., 2013).

Crosslinked siloxane- fluoro copolymer films can improve conduction and long-term stability while preventing the direct contact between the metal and medium, thus inhibiting aggressive corrosion. Seok et al. synthesized a crosslinked organosilicon-acrylate copolymer thin film that includes V4D4 and cyclohexyl methacrylate (CHMA) via iCVD process to prevent a water permeation with enhanced mechanical stability (Seok et al., 2018). Achyuta et al. used iCVD to fabricate a copolymer film with V3D3 monomer and hexavinyldisiloxane (HVDS). They reported improved chemical durability in both polar and nonpolar solvents such as tetrahyrofuran, acetone, isopropyl alcohol, and dimethyl sulfoxide due to its cross-linked network (Achyuta et al., 2009). Lee et al. synthesized a copolymer of poly(V4D4) and poly(PFDMA) (poly-perfluorodecyl methacrylate) via iCVD to enhance its mechanical durability (Lee et al., 2019). However, only a few studies exist related to iCVD poly(V4D4) films and their physical properties such as passivation performance in literature (Zhao et al., 2019). Gleason and co-workers investigated chemical stability and corrosion resistance of iCVD homopolymer films of polydivinylbenzene (poly(DVB)), poly(V3D3), poly(V4D4), and poly(1H,1H,2H,2H-perfluorodecyl acrylate) (poly(PFDA)). It is reported that poly(V3D3) and poly(V4D4) films showed a good stability and low surface corrosion due to crosslinked nature (Zhao et al., 2019).

3.2.2. Fluorinated Polymers

In recent years, research related to fluorine-containing polymers has been gaining more attention due to their unique water repellent properties, outstanding thermal and chemical stability, as well as excellent mechanical properties. Therefore, fluoropolymers are promising candidates in a wide range of applications as hydrophobic modification with water and oil repellency of textile and building materials, membrane distillation and fabrication of superhydrophobic surfaces. In the past decade, there have been exciting developments of fluorinated acrylates for fabrication of hydrophobic surfaces. 1*H*, 1*H*, 2*H*, 2*H*-perfluorodecyl acrylate (PFDA) is a typical hydrophobic monomer to fabricate membranes with a low-energy surface. Gupta et al. focused on the optimization of the

PFDA polymerization by iCVD method in terms of its mechanistic aspects for coating more complex geometries (Gupta and Gleason, 2006). They also investigated the effect of both substrate temperature and monomer partial pressure on the deposition rate. The deposition rate of poly(PFDA) thin films was found to be 350 nm/min at 0.28 of P_m/P_{sat} which was the highest value for this experiment study (Gupta and Gleason, 2006). In 2008, Gupta and co-workers studied the internal surface coating of high-aspect-ratio structures by using iCVD technique (Gupta et al., 2008). In this study, they fabricated poly(PFDA) coatings on the capillary pore membrane due to low-surface-energy property. It was concluded that the hydrophobicity increases with porosity based on contact angle measurements (Gupta et al., 2008). Other research related to poly(PFDA) thin film deposition on membrane with 3 μm of pore diameter and pore lengths of either 120 μm or 240 μm and the nominal porosity of either 30% or 50% by using iCVD technique was examined by Gupta and Gleason (Gupta and Gleason, 2009). It was concluded that the inner walls of pores for membrane coated with poly(PFDA) had aspect ratios as high as 80:1 (Gupta and Gleason, 2009). Karaman et al. demonstrated poly(PFDA) thin films on the stainless steel meshes via iCVD methods to fabricate superhydrophobic-superoleophilic membranes in oil-water separation application (Bayram et al., 2021). According to the results of the tests, it was concluded that the coating film had a high separation efficiency of 98.5% for oil-water mixture. Mao and Gleason fabricated copolymers using glycidyl methacrylate (GMA) with 2,2,3,3,4,4,5,5,6,6,7,7-dodecafluoroheptyl acrylate (DFHA) and with (perfluoroalkyl)ethyl methacrylate (PFEMA) via iCVD process and evaluated their mechanical properties, surface energies, and optical properties (Mao and Gleason, 2006). They synthesized copolymer films by tuning the flow rate ratio of monomer pairs and reported hardness, modulus, and transparency in the cross linked fluorinated thin films. Mao et al. demonstrated polymer coatings with poly(caprolactone) (PCL) bottom layer and perfluoroalkyl ethyl methacrylate (PPFEMA) top layer on the fabrics via a combination of electrospinning and iCVD methods to develop the superhydrophobic fabrics (Ma et al., 2005).

CHAPTER 4

CVD DEPOSITED OXYGEN SELECTIVE FLUORINATED SILOXANE COPOLYMERS AS GAS DIFFUSION LAYERS

4.1. Introduction

As the worldwide demand for energy storage grows rapidly, electrochemical energy storage technologies, mainly batteries have attracted a lot of interest. The primary requirement for energy storage systems ranging from small portable electronic devices to large electric vehicles is stable electrochemical performance with high energy and power density, long cycle life and high depth of discharge (Clark et al., 2020; Linden and Reddy, 2001; Schröder et al., 2016). Rechargeable batteries including Pb-acid, Ni-Cd, NiMH and Li-ion are the most commonly used battery technologies for stationary energy storage applications. Due to higher energy and power densities, Li-ion batteries are in a better position to compete with other battery technologies that are commercially available today. However, Li-ion batteries suffer from several issues including safety, availability and cost of raw materials used in manufacturing, and environmental impact. Therefore, new approaches and considerable efforts to develop efficient, scalable, sustainable, and environmentally friendly ‘‘beyond Li-ion’’ storage solutions are needed. In recent years, metal-air batteries have received much attention as the next-generation energy storage solution due to their higher theoretical energy density (1000-13000 Wh kg^{-1}) and lower weight compared to current energy storage systems (Clark et al., 2020). Today’s metal-air batteries are mostly primary batteries in which the capacity of the battery usually depends on the capacity of the metal electrode. However, electrochemical stability of Gas Diffusion Electrode (GDE) is also important for overall performance of metal-air batteries. Metal air batteries did not reach their full potential due to problems associated with electrode reversibility and electrochemical stability. Even today’s commonly used metal-air battery is a century old alkaline Zinc-Air Battery (ZAB) found only limited use in medical and tele-communication applications. In addition to problems associated with specific metal electrodes, the development of metal-air batteries is largely hindered by critical challenges related to the reversibility and lifetime of GDEs in which a gas reactant

comes in contact with a liquid reaction medium. A typical GDE is made of a porous hydrophobic membrane (gas diffusion layer, GDL), a catalytic layer (active layer) and a current collector. Although most efforts are focused on synthesis of bifunctional catalysts and carbon-free catalytic layers, the role of GDL layer on GDE performance should not be overlooked (Ikezawa et al., 2021). Moisture penetration from atmosphere is one of the major problems for alkaline metal-air batteries since it leads to formation of insoluble products. The moisture also restricts oxygen diffusion through the electrode which can severely reduce electrochemical activity of cathode (Amici et al., 2016a; Amici et al., 2016b). In addition, water uptake through the cell leads to decreased electrolyte concentration, considerably reducing ionic conductivity and deteriorating cycling life (Crowther et al., 2011; Mainar et al., 2018). Therefore, most of the current studies in literature related to metal-air batteries have reported cycling ability and rate ability in dry O_2 atmosphere (Kim et al., 2016; Chang et al., 2015; Zhu et al., 2017b; Yang et al., 2017; Flegler et al., 2017; Mainar et al., 2016). Another problem associated with metal-air batteries is excessive water loss from electrolyte negatively affecting discharge reactions during long-term operation (Ruan et al., 2018; Xie et al., 2019; Wang et al., 2021). The thickness of the air electrode may also hinder mass transfer of oxygen as well as the capacity and rate of performance of the metal-air batteries (Lin and Nguyen, 2005; Zhang et al., 2010c). Oxygen transport limitation and oxygen starvation during cathode reactions at high current density results in serious charge/discharge polarization and poor rate performance (Fu et al., 2012; Zhang et al., 2010a).

To enhance oxygen permeability and reduce the permeation of moisture and electrolyte evaporation, different approaches with varying success have been studied such as impregnation of a proton conductor (such as Nafion) into catalyst layer (Qi et al., 1998; Antolini et al., 1999) and changing chemical composition (Zhang et al., 2010a; Cao et al., 2015) and thickness (Lin and Nguyen, 2005) of GDL. Zhang et al. fabricated Li-air batteries with an O_2 selective air electrode for operation in ambient air (20-30% RH) for more than a month (Zhang et al., 2010a; Zhang et al., 2010d). Yue et al. employed proton-doped conductive polyaniline (PANI) films for Li-air batteries to restrict the moisture intake and electrolyte evaporation through the cell (Fu et al., 2012). Crowther at al. applied an O_2 selective membrane based on polysiloxane and methacrylate-polysiloxane copolymers for Li-air batteries to preclude water transport from atmosphere (Crowther et al., 2011). In a similar study, Bodoardo et al. reported that silicone oil wetted poly(vinylidene fluoride co-hexafluoropropylene) (PVDF-HFP) film as oxygen selective

membrane was effective to retain moisture and prevent membrane dehydration (Amici et al., 2016a). A PVDF-HFP matrix consisting of dextrin-nanosponge to entrap moisture from air was also investigated (Amici et al., 2016b). Lu et al. applied oxygen selective membranes based on polymers and Metal-Organic Framework (MOF) containing -OH and -NH_2 groups to effectively trap H_2O and CO_2 (Cao et al., 2015). Non-solvent induced phase separation (Cao et al., 2015; Amici et al., 2016a; Amici et al., 2016b), solution deposition (Xie et al., 2019; Zhang et al., 2010a) and evaporation-deposition (Labbe et al., 2021) are commonly used methods to fabricate GDLs with oxygen selectivity and water permeation resistance. However, both methods suffer from poor conformality and limited thickness control on the surface. Most GDL layers in today's GDEs for metal air batteries cannot separate O_2 and H_2O based on bulk or Knudsen diffusion due to higher diffusivity and smaller molecular diameter of H_2O (Cao et al., 2015; Crowther and Salomon, 2012; Ruan et al., 2018). An ideal GDL should have high oxygen permeability and serve as a moisture barrier. Two specific material groups seem to be promising candidates for fabrication of the ideal GDL: (1) Polymer membranes containing siloxane with extremely high O_2 solubility and thermal stability, (2) hydrophobic perfluorinated polymers with high chemical and thermal stability in addition to high O_2 solubility to suppress moisture uptake and electrolyte evaporation. Although copolymers of these specific materials could meet the requirements for GDL, it is also necessary to employ a low-cost and scalable technique that can fabricate GDL layers in various geometries and dimensions.

Here we report the synthesis of thin copolymer films of 2,4,6,8-tetramethyl-2,4,6,8-tetravinylcyclotetrasiloxane (V4D4), 2-(perfluorohexylethylacrylate) (PFHEA) and 2-(perfluoroalkylethylmethacrylate) (PFEMA) via initiated Chemical Vapor Deposition (iCVD) for potential candidates as GDL materials. Due to the high oxygen solubility of V4D4 and excellent hydrophobic behavior of PFHEA and PFEMA, their copolymers can effectively promote the diffusion of oxygen and restrict moisture intake. Although we did not attempt to address any issues related to bifunctional catalyst layer and current collector, we also report the electrochemical performance of GDEs fabricated using commercially available catalyst and current collector as active layer and iCVD deposited copolymer GDLs. To the best of our knowledge, this is the first study in literature where poly(V4D4-co-PFHEA) and poly(V4D4-co-PFEMA) copolymer coatings are fabricated and implemented as GDL in battery applications.

4.2. Material and Methods

4.2.1. Materials

Analytical grade chemicals, 2,4,6,8-tetramethyl-2,4,6,8 tetravinylcyclotetra siloxane (V4D4, Sigma-Aldrich, 97%), 2-(perfluorohexylethyl) acrylate (PFHEA, Fluoryx Inc., >99%), and 2-(perfluoroalkyl) ethylmethacrylate (PFEMA, Fluoryx Inc., >93%) as monomers and tert-Butyl peroxide (TBPO, Sigma-Aldrich, 98%) as initiator were used for the fabrication of copolymer thin-films. Polysulfone (Psf) (Sigma Aldrich, MW 26000) and chloroform (Sigma Aldrich) were used for the preparation of support membrane used during Water Vapor Permeability (WVP) measurements due to high water permeability of Psf (Choi et al, 2019; Ravishankar et al., 2018).

4.2.2. Preparation of Support Membranes

Polysulfone (Psf) was used as supporting membrane/substrate for water vapor and oxygen permeability measurements. To fabricate support membranes, Psf was heated at 140 ^{o}C for 3 h under vacuum to remove absorbed water. To obtain 12 wt.% Psf solution, 2.05 g of Psf was dissolved in 10 mL chloroform and stirred for 24 h to obtain a viscous solution. About 10 mL of Psf solution was dispensed on a glass substrate (2.5 cm x 2.5 cm), which was then spun at 1500 rpm for 30 s in a spin coater (Laurell, Model WS-650MZ-23NPPB0), followed by drying at 70 ^{o}C for 1 h to evaporate any residual solvent.

4.2.3. Synthesis of GDLs

A custom-built CVD reactor with a square bottom 31.6 cm in length and a height of 4 cm was used for the fabrication of copolymer GDLs. The top of the reactor was covered with a 2.5 cm thick quartz plate. A filament array (80% Ni/20% Cr, AWG 26) suspended 2.5 cm above the bottom of the reactor was resistively heated to desired temperature. Filament temperature was controlled via a thermocouple (Type K, Omega Engineering) connected to a PID controller (Model SSRL24ODC25, Omega Engineering). Substrate temperature was controlled by an external circulator (WiseCircu - refrigerated bath circulator) connected to the bottom part of the reactor. The pressure

inside the reactor was adjusted with a throttling butterfly valve (Model 253B, MKS type) and a pressure sensor (MKS 627D11TDC1B). Vacuum was provided with a rotary vane pump (BSV10, Baosi) with a cold trap attached on the exhaust line. Poly(V4D4), poly(PFHEA), poly(PFEMA) homopolymers and their poly(V4D4-co-PFHEA) and poly(V4D4-co-PFEMA) copolymers were deposited on crystalline silicon (c-Si) wafer, on 9.5 μm thick Psf support membranes for oxygen and water vapor permeability tests, and on commercial GDEs (Ocali A.S.) after their original GDLs were removed for electrochemical characterization. Fluorinated monomers PFHEA and PFEMA in stainless steel containers were heated to 65 ºC and 95 ºC, respectively. Monomer vapors were metered into the chamber through Mass-Flow Controller (MFC) (Model 1479A, MKS). TBPO was kept at room temperature and delivered to the reactor through an MFC (Model 1479A, MKS). V4D4 monomer was heated to 90 ºC and fed into the chamber through a special MFC (Model 1150C, MKS). Reactor pressure was maintained at 250 mTorr throughout the study. The substrate and filament temperature were adjusted for optimum deposition rate for homopolymers and copolymers. The filament temperature was set to 250 ºC for PFEMA homopolymer and fixed at 300 ºC for all other homopolymer and copolymer film depositions. A final film thickness of 350 ± 50 nm was targeted.

4.2.4. Characterization of GDLs

Fourier Transform Infrared Spectroscopy (FTIR) analysis was performed using a Perkin Elmer Inc.-Spectrum BX FTIR Spectrometer to investigate the quality and chemical composition of fabricated GDLs. The spectra were measured from 4000 to 650 cm^{-1} with a 4 cm^{-1} step size accumulating 20 scans. All spectra were baseline corrected and thickness normalized. Peak deconvolutions were performed using C=O stretching band in PFHEA and PFEMA (1700-1770 cm^{-1}) and asymmetric Si-O-Si stretching band (1010-1100 cm^{-1}) in V4D4 for chemical composition evaluation. The thickness measurements for iCVD deposited GDLs were performed using an Mprobe-Vis20 reflectometer with a spectral range of 400-1100 nm and TF Companion software. The surface morphologies of GDLs were investigated using an FEI Quanta250 Scanning Electron Microscopy (SEM) system with a field emission gun. A Theta Optical Tensiometer system was used for Water Contact Angle (WCA) measurements to investigate the hydrophobicity of the surface. Static contact angle measurements were

performed by dropping 5 μL ultrapure water on the film surface. Water Vapor Transmission Rates (WVTR) of poly(V4D4), poly(PFHEA), poly(PFEMA) homopolymers and their copolymers, and Psf support membranes were determined using a Mocon Permatran-W Model 3/33 instrument. Measurements were performed at 37.8 °C and at 90% relative humidity with 100 cm^3 min^{-1} nitrogen flow rate as described in ASTM F1249 standard. Permeance and permeability were calculated using Eqs. (4.1) and (4.2):

$$\text{Permeance} = \frac{\text{WVTR}}{S(R_1 - R_2)} \tag{4.1}$$

$$\text{Permeability} = \text{Permeance} \times \text{Thickness} \tag{4.2}$$

where:

R_1 = Relative humidity at the source expressed as a fraction

(R_1 = 1.00 for a 100% RH chamber, and for 90% RH chamber R_1 = 0.90)

R_2 = Relative humidity of the vapor sink expressed as a fraction

(R_2 = 0 for the 0% RH chamber (dry side))

S = Vapor pressure of water at the test temperature

Oxygen permeability measurements of iCVD deposited homopolymer and copolymer films were performed on Psf support membranes following ASTM D3985 standard using a Dansensor Lyssy L-100-5000 Manometric Gas Permeability Tester. Measurements were performed at 23 °C and 0% relative humidity with 5-10 cm^3 min^{-1} pure oxygen gas flow rate. Gas transmission rates for samples were calculated using Eq. (4.3);

$$\frac{L}{P} = \frac{L_s}{P_s} + \frac{L_c}{P_c} \tag{4.3}$$

where P is the apparent permeability of the structure, L is the total thickness $L_s + L_c$, and P_s and P_c are the permeability of support (s) and coating (c) respectively (Chatman, 1996; Chen et al., 2019).

4.2.5. Fabrication of GDEs

Commercial GDEs used in this study consists of three parts: catalyst layer, nickel mesh as a current collector, and gas diffusion layer (GDL). GDL of commercially

available GDE was carefully removed without damaging catalysts layer and nickel current collector. Poly(V4D4), poly(PFHEA), poly(PFEMA) homopolymers and their poly(V4D4-co-PFHEA) and poly(V4D4-co-PFEMA) copolymers were deposited via iCVD to serve as GDL only on the surface facing outside.

4.2.6. Electrochemical Measurements

All electrochemical measurements were performed using a Potentiostat/ Galvanoostat/ZRA (Gamry Model 22162) with tripolar electrode measurement apparatus. Electrochemical tests were performed in a custom-made three-electrode cell with 6 M KOH as electrolyte, a Pt wire as counter electrode, and a saturated Ag//AgCl reference electrode at 25 ± 2 ^{o}C. GDEs (8 mm in diameter) with iCVD GDL layers (V4D4, PFHEA or PFEMA and their copolymers) were used as working electrodes. Measurements were carried out after 15 min N_2 purge and under constant potential mode similar to previous studies in literature (Yatagai et al., 2016; Tada et al., 2017). Cyclic voltammetry (CV) was carried out between -0.8 V to 1.2 V at a scan rate of 5 mV s^{-1}. AC impedance measurements of half-cells were also performed from 10 kHz to 10^{-1} Hz at room temperature. All electrochemical measurements were carried out under atmospheric condition. Chronoamperometry (CA) measurements were performed at 1.5 V to evaluate diffusion coefficients.

4.3. Results and Discussion

Two different series of copolymer films containing a highly oxygen permeable V4D4 and hydrophobic PFHEA and PFEMA were fabricated as GDLs via iCVD. Copolymer films with various composition of fluorinated monomer (PFHEA or PFEMA):V4D4 ratios were obtained by adjusting the flow rates of monomers during polymerization. Similar deposition conditions reported in our previous work were used for iCVD GDL fabrication as summarized in Table 4.1 (Cihanoğlu and Ebil, 2021).

Table 4.1. Summary of process conditions for iCVD GDLs.

Sample name	F_{V4D4} (sccm)	F_{PFHEA} (sccm)	F_{PFEMA} (sccm)	F_{TBPO} (sccm)	P_{total} (mTorr)	$T_{substrate}$ (^oC)	$T_{filament}$ (^oC)	Deposition rate (nm min^{-1})
V4D4 homopolymer	0.32	-	-	0.16	250	45	300	6.13
HCO-1	0.22	0.044	-	0.44	250	45	300	3.84
HCO-2		0.088						4.37
HCO-3		0.132						5.75
HCO-4		0.176						6.84
HCO-5		0.22						9.78
PFHEA homopolymer	-	0.32		0.11	250	25	300	89.87
ECO-1	0.22	-	0.044	0.44	250	45	300	2.64
ECO-2			0.088					2.85
ECO-3			0.132					3.11
ECO-4			0.176					3.29
ECO-5			0.22					3.72
PFEMA homopolymer	-	-	0.2	0.025	250	35	250	18.82

In iCVD process, the deposition rate of polymer strongly depends on the concentration of adsorbed monomers on substrate surface (Kwak et al., 2015; Gleason, 2015). In case of copolymerization, at a fixed substrate temperature, the surface concentrations of monomers will vary depending on their partial vapor pressures on the gas phase and their saturation pressures. Therefore, copolymer composition was controlled by adjusting the flowrates of monomer during polymerization. Figure 4.1 shows copolymer deposition rate as a function of monomer flow rate ratios. Copolymer deposition rate increases exponentially with F_{PFHEA}/F_{V4D4} ratio, however, this increase is linear with F_{PFEMA}/F_{V4D4} due to the difference of absorbed monomer surface concentration. iCVD copolymerization rate depends on the monomer surface concentration, monomer reactivity ratios, and copolymerization temperature. The monomer surface concentration is related to saturation ratio (the ratio of monomer partial vapor pressure to the monomer saturation vapor pressure) (Gleason, 2015). At 25 ^oC, V4D4 has a much lower vapor pressure (~40 mTorr) (Kwak et al., 2015) compared to PFHEA (~332 mTorr) (Wang et al., 2010). On the other hand, there is no experimental data for the vapor pressure of PFEMA in the literature (Tsibouklis et al., 2000).

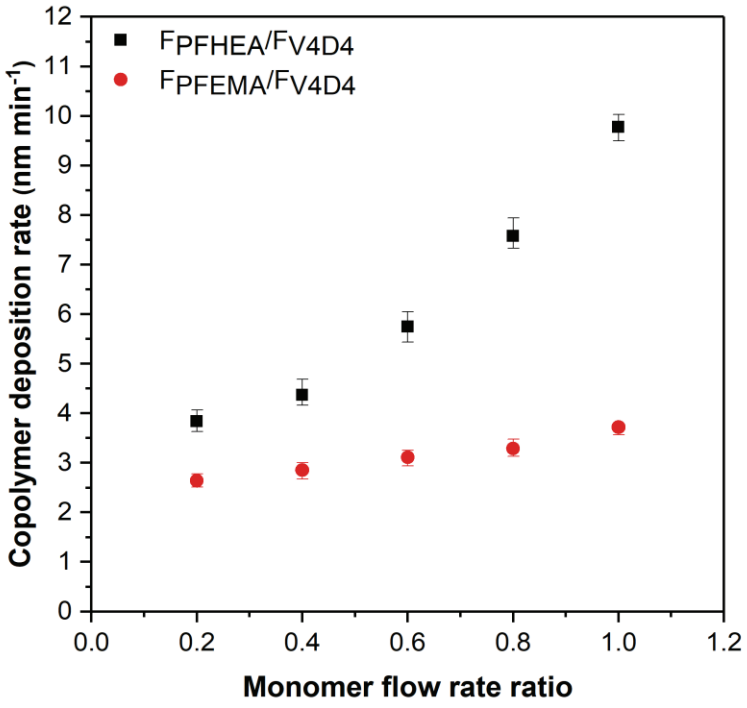

Figure 4.1. Deposition rates as a function of flow rate ratio of monomers.

FTIR measurements were performed for all homo and copolymer films to evaluate chemical composition of copolymers and crosslinking between vinyl groups in V4D4 and acrylic groups in fluoropolymers (see in Table 4.2). Figure 4.2 shows FTIR spectra of homo and copolymer films deposited via iCVD.

Table 4.2. FTIR absorption frequencies and peak intensities for PFHEA, PFEMA and V4D4 monomers

Group	**iCVD film (cm^{-1})**	**Literature (cm^{-1})**	**Intensity**	**Ref.**
Si-O-Si stretch	1010	1010-1070	Strong	(Achyuta et al., 2009)
Si-CH_3	1261	1255-1280	Strong	(O'Shaughnessy et al., 2006)
Si-CH_2 deformation	1410	1390-1410	Medium	(Trujillo et al., 2010)
CH stretch of vinyl bond	3000	2995-3020	Medium	(O'Shaughnessy et al., 2006)
CH_2 symmetric stretch vinyl group	3059	3075-3090	Medium	(Achyuta et al., 2009)
-CF_3 stretch	1143	1142	Medium	(Ma et al., 2005)
-CF_2 absorption vibration stretch	1232	1200-1240	Medium	(Yin et al., 2017)
C=O stretch in ester group	1741	1735-1750	Strong	(Chan and Gleason., 2005)

Figure 4.2(b) and (c) are enlargements of a portion of Figure 4.2(a) emphasizing the absorption peaks ranging from 1700 to 1770 cm^{-1}. This enlarged view provides vital information about the changes in relative intensities of absorption peaks related to C=O stretching in acrylic groups for copolymers with increasing PFHEA and PFEMA content. Fluorinated monomer fraction in copolymers is directly related to area of this individual peak. As expected, the highest peak intensity (and peak area) was observed when fluorinated monomer/V4D4 flow rate ratio is 1 and decreases with increasing V4D4 in copolymer composition.

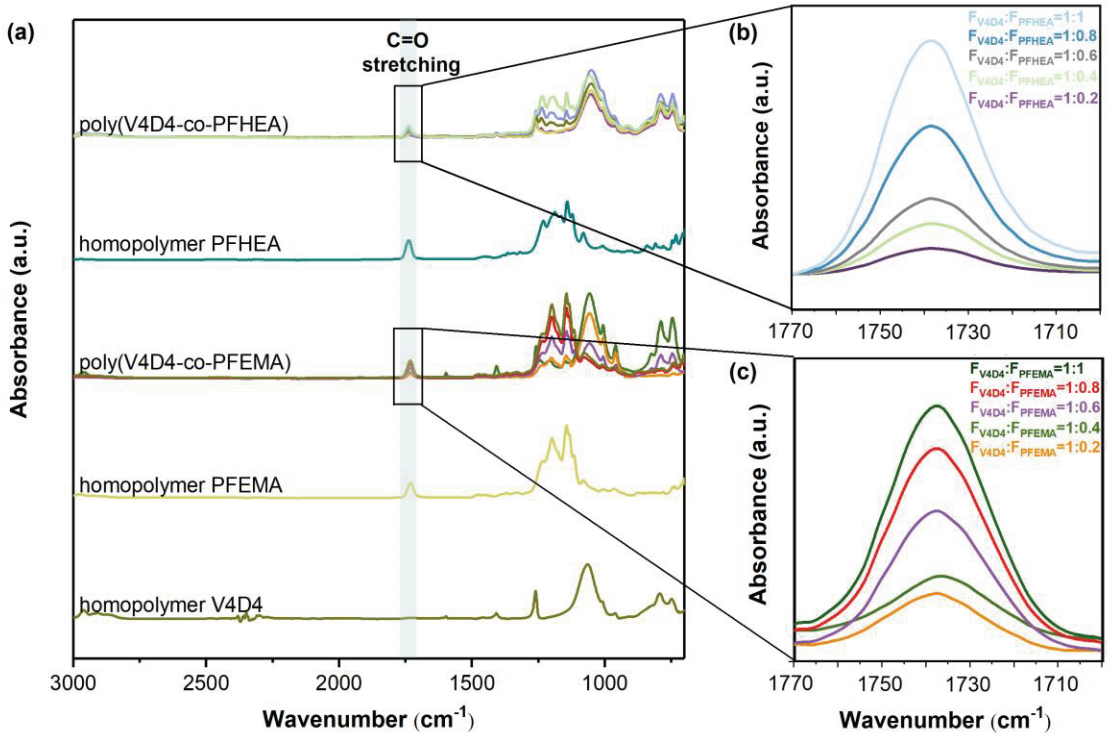

Figure 4.2. FTIR spectra of (a) V4D4, PFHEA, PFEMA homopolymers and their copolymers, (b) and (c) enlargement of C=O stretching region for poly(V4D4-co-PFHEA) and poly(V4D4-co-PFEMA) copolymers, respectively.

A gas diffusion layer in alkaline metal-air battery should have low water/electrolyte permeability to prevent corrosion of metal anode by moisture. Especially in a humid environment, water uptake by GDE leads to reduced electrochemical activity and ionic conductivity due to dilution of the electrolyte (Amici et al., 2016a; Amici et al., 2016b; Ruan et al., 2018; Xie et al., 2019; Mladenova et al., 2021)). Therefore, ideal GDL layer should be superhydrophobic, have high oxygen and very low water permeability. Figure 4.3 shows WCA measurement performed on iCVD

copolymer films fabricated on c-Si and Psf support membranes. Higher contact angles for poly(V4D4-co-PFHEA) copolymers compared to poly(PFHEA) homopolymer on bare Psf membrane (57.96° ± 1.15°) and bare Si wafer (56.25° ± 1.15°) are mainly due to the existence of fluorinated groups in PFHEA. As expected WCA values increase with the increase in fluorinated groups in copolymer composition. In addition, an increase in the surface roughness of copolymer films can also contribute to hydrophobicity (Kwak et al., 2015; Seok et al., 2018). WCA values of poly(PFEMA) homopolymer on Si wafer and Psf membrane measured as 145.4 ± 0.3° and 131.5° ± 0.4°, respectively, are significantly higher than that of poly(PFHEA) homopolymer as seen on Figure 4.3(b). Interestingly, WCA values of poly(V4D4-co-PFEMA) copolymers did not show any significant change on Psf support membrane, but showed considerable change on c-Si substrate as PFEMA:V4D4 ratio increased. In addition, WCA value of poly(V4D4) homopolymer on Psf support membrane was found to be higher than that on c-Si. This can be attributed to the roughness of Psf membrane surface (Nabe et al., 1997).

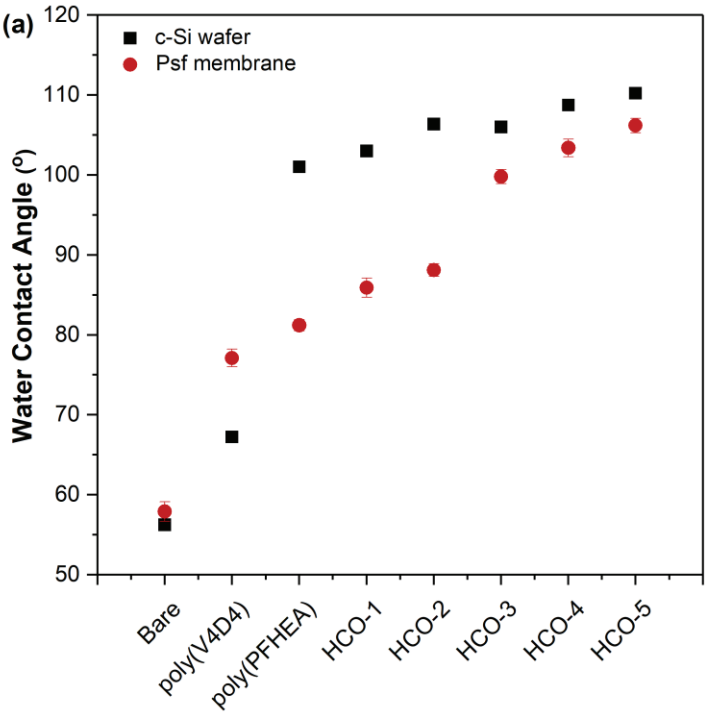

Figure 4.3. WCA measurements of iCVD poly(V4D4), (a) poly(PFHEA); (b) poly(PFEMA), and their copolymers.

(Cont. on next page)

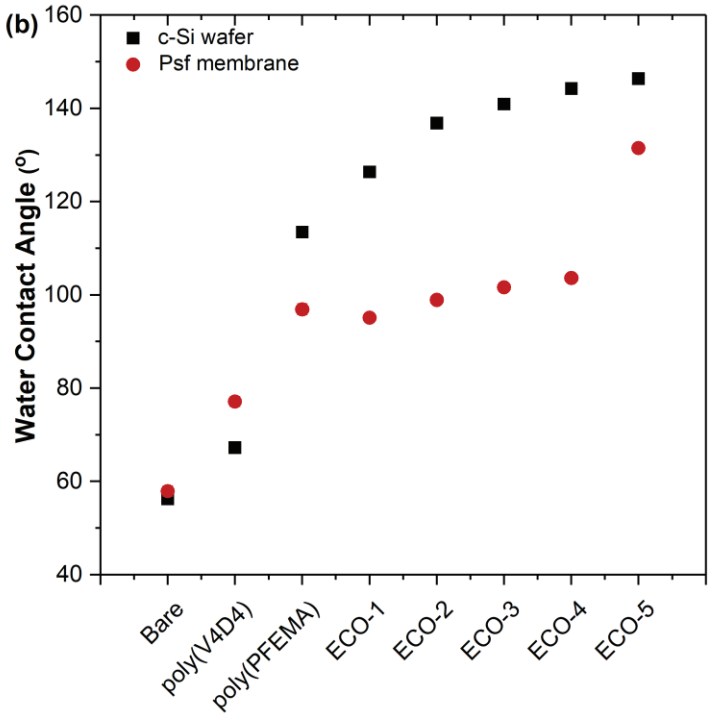

Figure 4.3. Cont.

SEM images of poly(V4D4-co-PFHEA) copolymers with different PFHEA:V4D4 ratios are shown on Figures 4.4(a-e). SEM images show slightly increased surface roughness with an increasing PFHEA:V4D4 ratio similar to aggregation behaviors observed in many copolymers (Lee et al., 2019; Seok et al., 2018; Ma et al., 2007). SEM images of poly(V4D4-co-PFEMA) copolymer reveal a smoother surface compared to poly(V4D4-co-PFHEA) as seen on Figures 4.4(f-j). As PFEMA in copolymer composition increase, surface morphology changes visibly, surface roughness increases and become similar to previously reported iCVD copolymers (Seok et al., 2018; Ozpirin and Ebil, 2018).

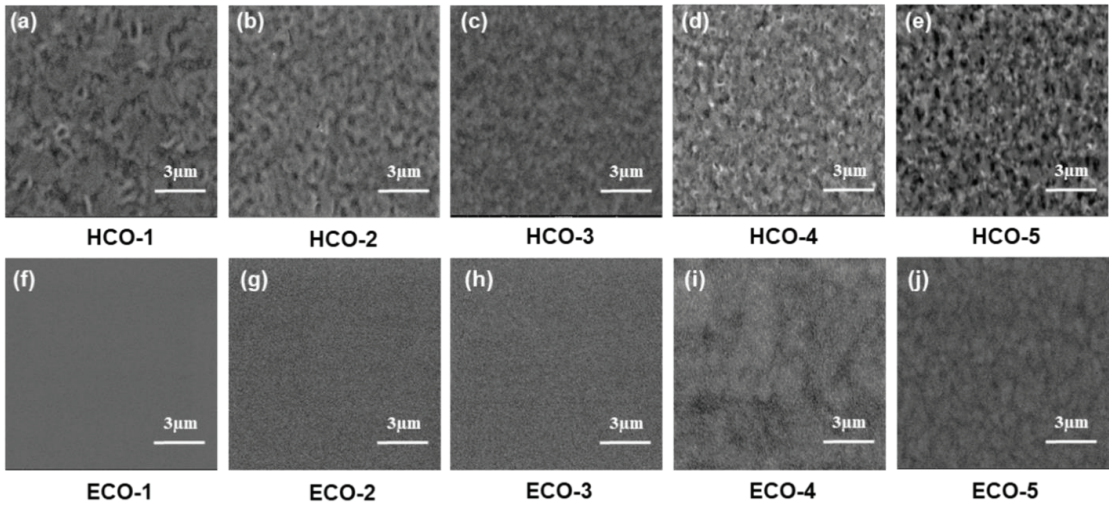

Figure 4.4. SEM images of (a-e) poly(V4D4-co-PFHEA) copolymer and (f-j) poly(V4D4-co- PFEMA) copolymers with increasing fluorinated monomer ratio.

WCA measurements are consistent with surface free energies reported in the literature and there is a significant difference in surface energies between V4D4 monomer (36.6 mJ m^{-2}) and fluorinated PFHEA and PFEMA (10.5 mJ m^{-2} and 6-8 mJ m^{-2}, respectively) monomers making them immiscible to each other, as seen in Table 4.3.

The relationship between contact angles and surface free energy components of a solid can be determined by Van Oss-Chaudhury-Good (OCG) equation (Onoe et al., 2004).

$$\gamma_L = (1 + cos\theta) = 2\sqrt{\gamma_S^{LW}\gamma_L^{LW}} + 2\sqrt{\gamma_S^{+}\gamma_L^{-}} + 2\sqrt{\gamma_S^{-}\gamma_L^{+}} \quad (4.4)$$

where γ_s and γ_L are the surface energy of solid and liquid components, respectively. γ_s^{LW} is the surface energy of a solid combining the Liftshitz/van der Waals component, + and – represents the electron-acceptor (Lewis acid) and the electron-donor (Lewis base) components, respectively. Table 4.3 shows surface free energy components of iCVD polymers used in this study.

Table 4.3. Surface free energies of iCVD polymers

Sample	Surface free energy, mJ m^{-2}			Ref.
	γ_s^{LW}	γ_s^{p}	γ_s	
V4D4	36.56	0	36.56	(Kwak et al., 2015)
PFHEA	10.24	0.29	10.53	(Wang et al., 2010)
PFEMA	6-8	0.1-0.3	6-8	(Tsibouklis et al., 2000)

γ_s^{p} the surface energy of a polar solid component

However, in iCVD process these monomers are vaporized and mixed in vapor phase where the effect of surface tension is very small before actual polymerization occurs on the substrate surface. Therefore, iCVD enables fabrication of homogenous films without phase segregation problems (Kwak et al., 2015). In a metal-air battery, water intake through GDE should be minimum for electrochemical stability. Electrode corrosion and capacity loss due to water is a serious problem, especially for alkaline metal-air batteries. Since iCVD fabricated GDL layers were very thin (~300-400 nm), Psf membranes were used to mechanically support homo and copolymer iCVD films during WVP measurements. As prepared, Psf support membranes have a water permeability of 3.38×10^{-9} mol m $m^{-2}Pa^{-1}s^{-1}$ and a water vapor transmission rate approximately 9.84×10^{2} g $m^{-2}day^{-1}$ making Psf a very suitable support material to measure oxygen and water permeabilities of iCVD fabricated GDL layers (Baldo et al., 2020; Choi et al., 2019). WVP and WVTR values of poly(V4D4), poly(PFHEA), poly(PFEMA) homopolymers and their copolymers are given in Table 4.4.

Table 4.4. Oxygen permeability, water vapor permeability, water vapor transmission rate and selectivity of Psf support membrane, poly(V4D4), poly(PFHEA), poly(PFEMA) homopolymers and their copolymers

	Oxygen Permeability x 10^{15} mol m $m^{-2}s^{-1}Pa^{-1}$	**Water Vapor Permeability x 10^{15} mol m $m^{-2}s^{-1}Pa^{-1}$**	**Water Vapor Transmission Rate x 10^{-1} g $m^{-2}day^{-1}$**	**Selectivity, α_{O_2/H_2O}**
Psf support membrane	0.5	3.38 x 10^{6}	98.4	1.47x10^{-7}
Poly(V4D4)	1.801±0.288	0.412±0.011	1.186±0.063	4.36
Poly(PFHEA)	0.204±0.048	0.327±0.001	0.686±0.111	0.62
HCO-1	0.741±0.007	0.475±0.031	1.132±0.134	1.56
HCO-2	1.162±0.229	0.379±0.038	0.859±0.184	3.06
HCO-3	1.414±0.205	0.345±0.007	0.818±0.039	4.09
HCO-4	1.895±0.009	0.283±0.001	0.673±0.073	6.71
HCO-5	3.531±0.761	0.268±0.008	0.592±0.073	13.16
Poly(PFEMA)	0.608±0.023	0.339±0.006	0.461±0.011	1.79
ECO-1	1.243±0.228	0.581±0.026	0.807±0.029	2.14
ECO-2	1.146±0.232	0.426±0.025	0.684±0.009	2.69
ECO-3	0.772±0.139	0.363±0.006	0.709±0.041	2.13
ECO-4	1.072±0.188	0.353±0.007	0.634±0.033	3.03
ECO-5	1.125±0.139	0.261±0.004	0.548±0.061	4.33

*Selectivity (α_{O_2/H_2O}) is described as $\alpha_{O_2/H_2O} = P_{O_2}/P_{H_2O}$ (the unit of permeability is mol m $m^{-2}s^{-1}Pa^{-1}$) [22].

**1 Barrer =3.35 x 10^{-16} molm $m^{-2}s^{-1}Pa^{-1}$

Commercially available thick GDLs that are used in fuel-cells and metal-air batteries exhibit water vapor transmission rates between 11.16 - 811.99 g m^{-2} day^{-1}. (Amici et al., 2016a; Amici et al., 2016b; Xie et al., 2019). Water tranmission rate values for poly(V4D4-co-PFHEA) and poly(V4D4-co-PFEMA) copolymers varied between 5.48 g m^{-2} day^{-1} and 11.32 g m^{-2} day^{-1}; between 2 and 150 times lower than commercial GDLs. Increasing fluorinated monomer in copolymer composition resulted in a slight reduction in water vapor permeability. HCO and ECO series GDLs showed comparable water vapor permeabilities; however, a clear trend of decreasing water vapor permeability with increasing fluorinated monomer was observed for both series. The role of a GDL is to provide sufficient oxygen transfer from air to catalyst layer in GDE while limiting water intake from ambient. In the literature perfluorinated chemicals (PFCs) were used as oxygen selective membranes (Ruan et al., 2018; Xie et al., 2019) or electrolyte additives (Wijaya et al., 2015; Wan et al., 2017) in Li-O_2 batteries. Most commercially available GDLs thar are used in alkaline metal-air batteries are thick and highly porous membranes or non-woven polymeric materials with hydrophobic outer surface exhibiting very high oxygen and water vapor permeabilities. Reported oxygen permeabilities of thin film non-porous polymeric GDLs such as PET, HDPE, PTFE prepared via extrusion or other methods and thicknesses between 10 and 1000 μm, varies between 3.35 x 10^{-18} mol m m^{-2} s^{-1} Pa^{-1} (0.01 Barrer) and 3.35 x 10^{-15} mol m m^{-2} s^{-1} Pa^{-1} (10 Barrer) (Crowther and Salomon, 2012). For comparison, very thin (350 ± 50 nm) iCVD prepared homo and copolymer films showed oxygen permeabilities ranging from 0.204 x 10^{-15} to 1.895 x 10^{-15} mol m m^{-2} s^{-1} Pa^{-1} (from 0.61 to 5.66 Barrer) except for poly(V4D4-co-PFHEA) copolymer with a 1:1 ratio of V4D4:PFHEA having the highest oxygen permeability of 3.53 x 10^{-15} mol m m^{-2} s^{-1} Pa^{-1} (10.5 Barrer). iCVD prepared homo and copolymer films showed oxygen permeabilities ranging from 0.204 x 10^{-15} to 1.895 x 10^{-15} mol m $m^{-2}s^{-1}Pa^{-1}$ (from 0.61 to 5.66 Barrer) except for poly(V4D4-co-PFHEA) copolymer with a 1:1 ratio of V4D4:PFHEA having the highest oxygen permeability of 3.53 x 10^{-15} mol m $m^{-2}s^{-1}Pa^{-1}$ (10.5 Barrer), as seen in Figure 4.5. Fluorinated homopolymers exhibit lower oxygen permeabilities compared to poly(V4D4) homopolymer; however, oxygen permeability increases with the addition of PFHEA in HCO series. A similar trend is not observed for ECO series. Poly(PFEMA) homopolymer exhibited higher oxygen permeability than poly(PFHEA) homopolymer. Oxygen and water vapor permeabilities seem to be inversely related due to the higher water diffusion rate and smaller molecule size compared to oxygen (Wan et al., 2017; Amici et al., 2016a).

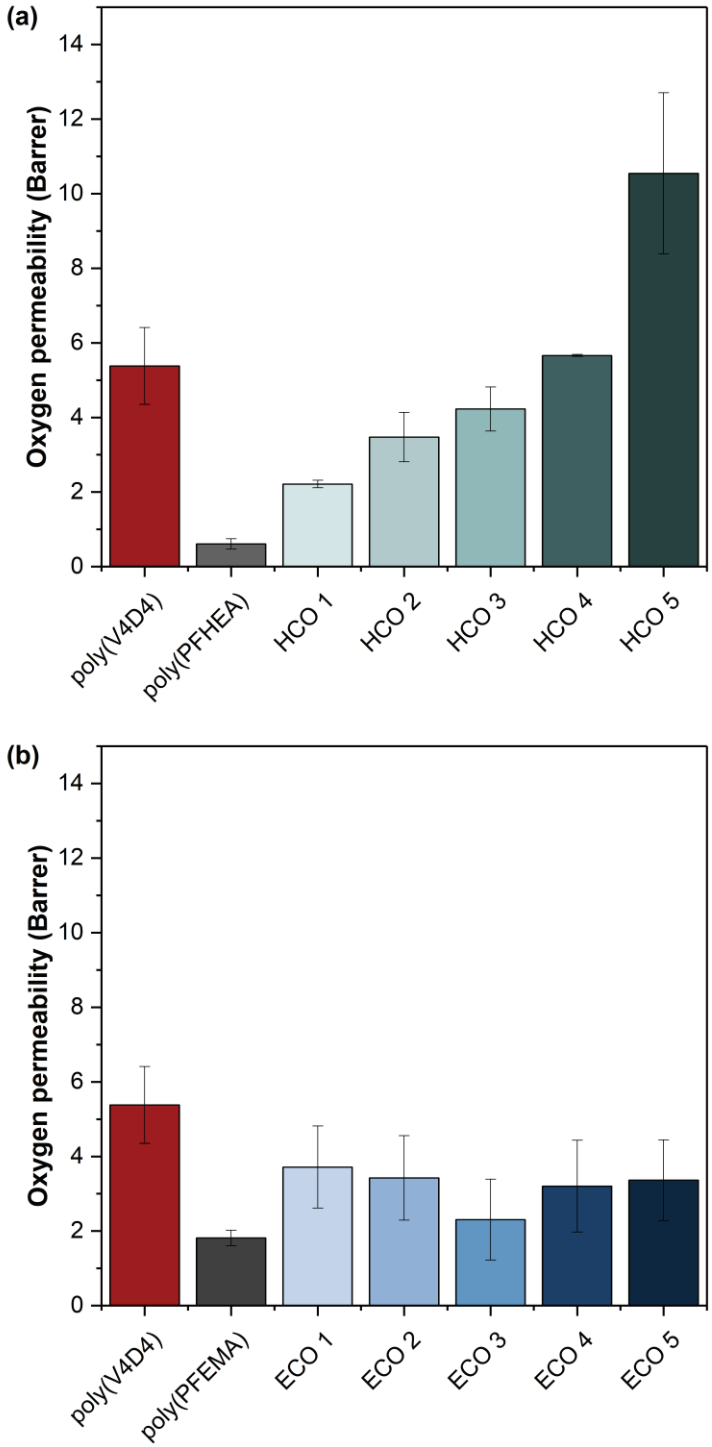

Figure 4.5. Oxygen permeabilities for poly(V4D4), poly(PFHEA), poly(PFEMA) and their copolymers.

In theory, the performance of gas diffusion electrode should increase using iCVD deposited copolymer GDLs due to enhanced O_2 and reduced H_2O permeabilities compared to conventional GDEs with relatively thick fluoropolymer GDLs. Poly(V4D4-co-PFHEA) copolymer (HCO-5) showed 17 times increase in O_2 permeability with more

than 1.2 times lower H_2O permeability (corresponding to an oxygen/water selectivity of 13.6) compared to poly(PFHEA) homopolymer. Poly(V4D4-co-PFEMA) copolymers did not show such drastic changes in oxygen and water permeabilities. These observations suggest poly(V4D4-co-PFHEA) copolymers are promising water barriers with enhanced oxygen permeabilities as GDLs.

Electrochemical properties of GDEs prepared with iCVD copolymer GDLs were evaluated by CV measurements with GDL exposed to air and the other side in contact with 6 M KOH solution. The area of GDE in contact with the solution was 0.502 cm^2. Figure 4.6 shows the effect of scan rate on electrochemical behavior of GDEs with poly(V4D4-co-PFHEA) (HCO-5) and poly(V4D4-co-PFEMA) (ECO-5) GDLs only. The peak related to oxygen reduction reactions can be observed in a wide potential range from -0.8 V to 1.2 V. Therefore, the voltage range of -0.8-1.2 V was selected during CV measurements.

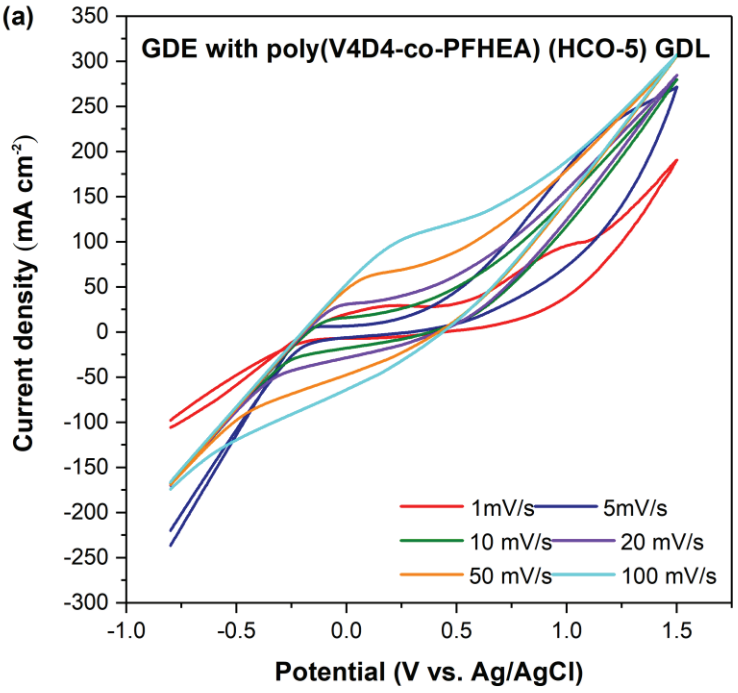

Figure 4.6. Effect of voltametric scan rate on current density for GDEs with (a) HCO-5 and (b) ECO-5 GDLs, and (c, d) corresponding relation of logarithm of peak current and logarithm of scan rate.

(Cont. on next page)

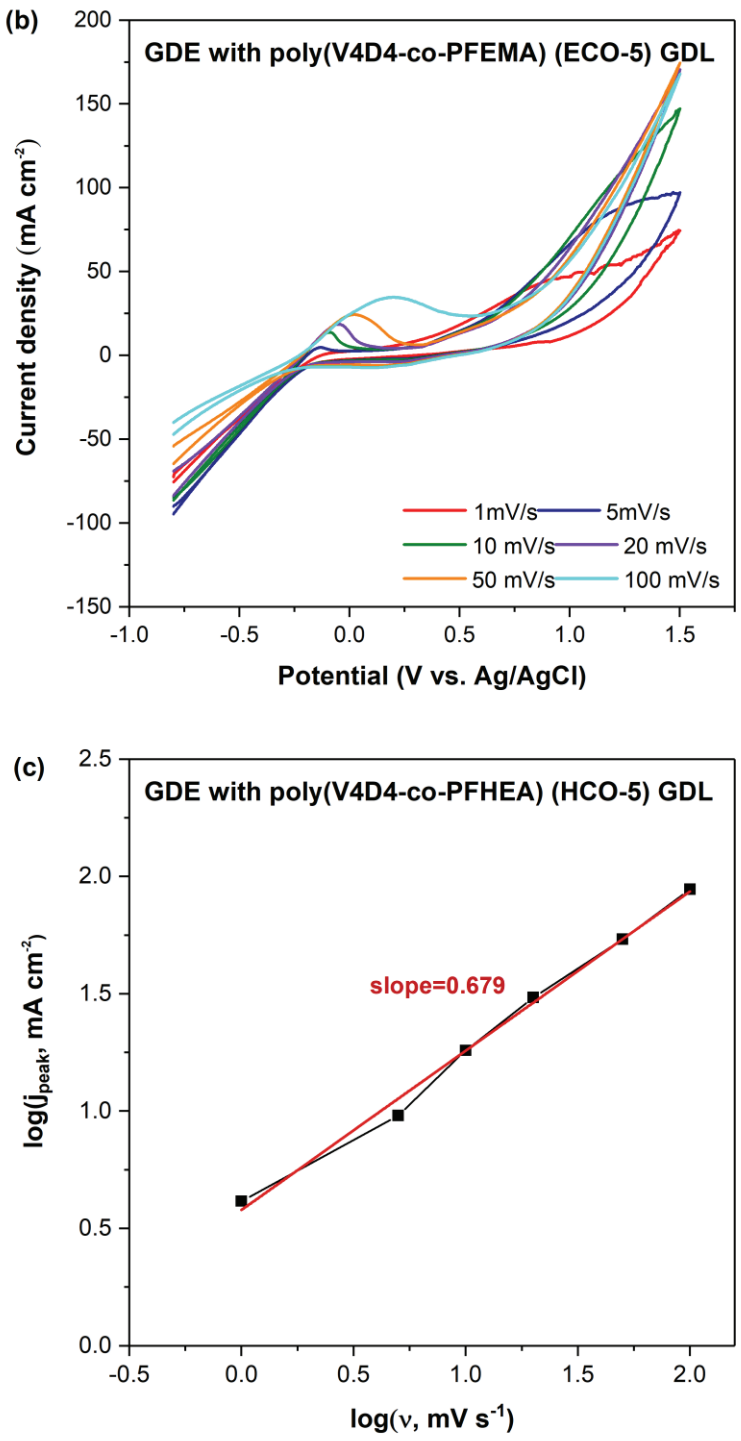

Figure 4.6. Cont.

(Cont. on next page)

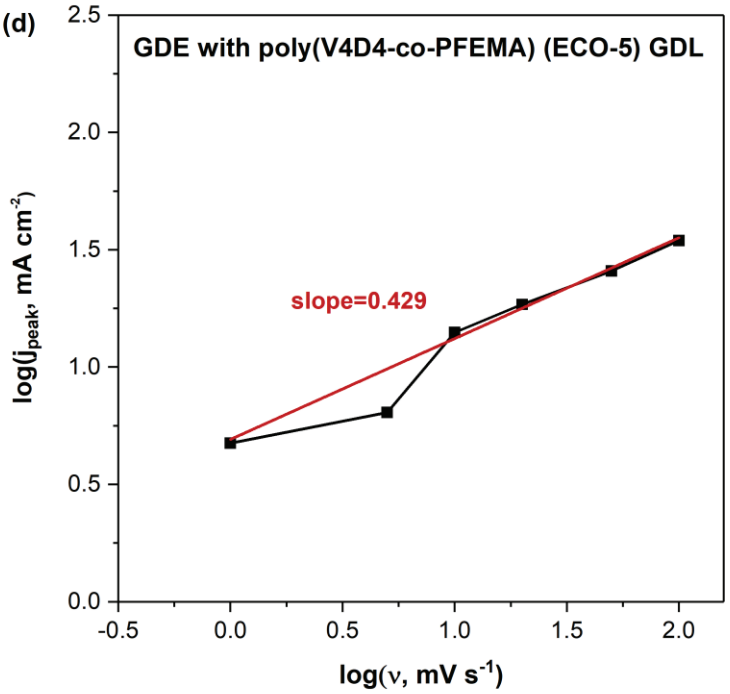

Figure 4.6. Cont.

The power-law dependence of the current density on scan rate can be expressed by the following equation (Opitz et al., 2015):

$$\log j = b \log \nu + \log a \qquad (4.4)$$

where j is current density, ν represents the scan rate, and a is a constant. The slope, b, describes charge transfer coefficient; a value close to 0.5 indicates a diffusion-controlled process while values close to 1 indicate pseudocapacitive case in which Faradaic charge transfer occurs by intercalation or adsorption of charge-compensating ions.

The oxidation peak current densities for GDEs with HCO-5 and ECO-5 GDLs increase with $\nu^{0.68}$ and $\nu^{0.43}$, respectively ($\log j_{peak} = 0.679 \log \nu + 0.706$ ($R^2=0.9939$) for HCO-5, and $\log j_{peak} = 0.429 \log \nu + 0.692$ ($R^2=0.9955$) for ECO-5 GDL). It seems the performance of both GDEs are mass transport limited (Li et al., 2019). Especially at higher scan rates, the charge flow decreases with increasing scan rate. Oxidation peaks for GDEs with poly(V4D4-co-PFHEA) and poly(V4D4-co-PFEMA) GDLs was more obvious at high scan rates. The peak was detected at the potential of 0.9 V related to 2+2-electron reduction reaction. The increase in peak broadening was observed when scan rate is increased from 1 mV s^{-1} to 5 mV s^{-1}. Additionally, there was a positive shift of

peak potentials with the increase of scan rate (Khairy et al., 2018). The peak broadening was not observed in higher scan rates since the peak was out of range due to peak position shift.

CV curves of the samples at 5 mV s^{-1} sweep rate are shown in Figure 4.7. The onset potential for oxygen evolution took place at 0.3 V vs. Ag//AgCl while the onset potential of oxygen reduction was below -0.2 V. GDE with HCO-5 GDL showed a higher current density when compared to commercial GDE with conventional thick GDL. The increase in current density is due to the higher oxygen transport in copolymer GDL. A lower reduction current density was observed for GDE with ECO-5 GDL (189.2 mA cm^{-2}) when compared to GDE with HCO-5 GDL (228.2 mA cm^{-2}) at -0.8 V. These observations are in good agreement with the oxygen and water permeability results considering especially high oxygen permeability of HCO-5 GDL.

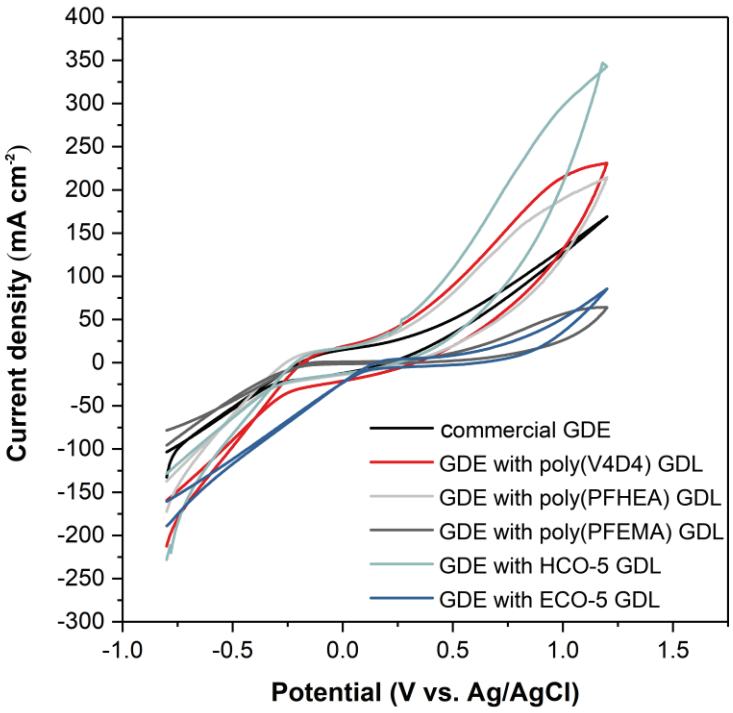

Figure 4.7. Cyclic voltammograms of GDEs with iCVD GDLs between -0.8 V and 1.2 V with a sweep rate of 5 mV s^{-1}.

In addition, stability of GDE is also an important parameter for evaluating battery performance. Stability tests were performed in 6 M KOH (at constant -0.8 V for ORR and 1.2 V for OER) for 240 h with a Pt wire counter electrode. The current densities obtained from cyclic voltammetry measurements were -229.7 mA cm^{-2} for ORR activity and 344.4 mA cm^{-2} for OER activity at the initial stage, as shown in Figure 4.8. The current density

for ORR did not change significantly after 240 h. However, the current density for OER was reduced to 208.9 mA cm^{-2}. It was observed that GDE with HCO-5 GDL was more stable for ORR activity and did not show a significant change in current density after 240 h immersion in 6 M KOH electrolyte.

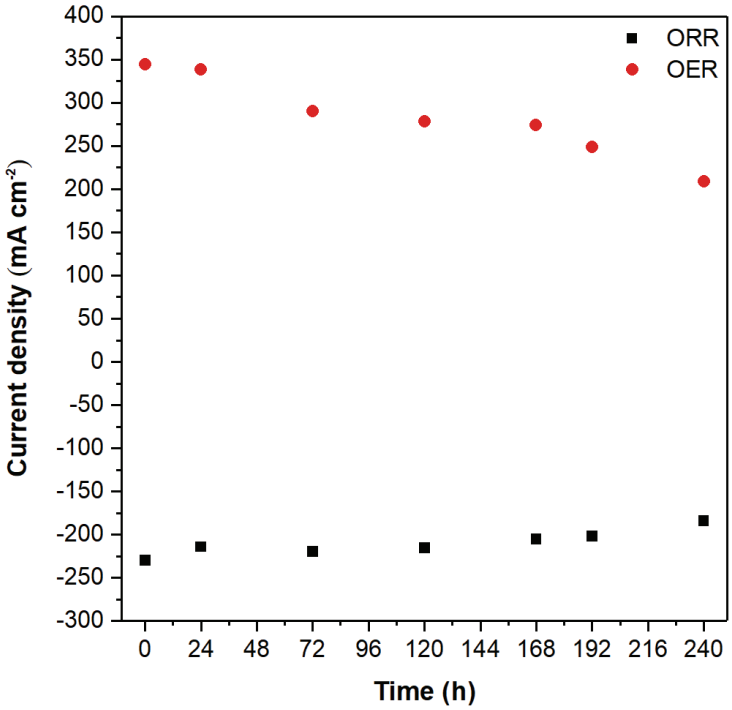

Figure 4.8. Stability test for GDE w/HCO-5 GDL.

The cathodic polarization behavior of GDEs with copolymer GDLs is shown in Figure 4.9. The polarization current density of GDE with HCO-5 GDL (-327 mA cm^{-2}) is greater than any other GDEs at the same potential. GDEs with poly(V4D4) and poly(PFEMA) GDLs had the lowest polarization current densities. As seen in Figure 4.9(a), the first region of the polarization curve shows an exponential dependence of current density over applied potential. In this region, defined as the mass-transport region, reaction kinetics is associated with limited oxygen supply (Aaron et al., 2011). In ohmic loss region (~ -0.3 to -0.6 V), the current density of commercial GDE is higher other samples except GDE with HCO-5 GDL. The polarization current density of GDE with HCO-5 is nearly double than that for the GDE with ECO-5 in transport loss region (< -0.6 V). HCO-5 GDL seems to be providing enhanced gas transport, exerting a positive effect on the performance of the GDE due to the sharp current density increase in the mass-transport loss region.

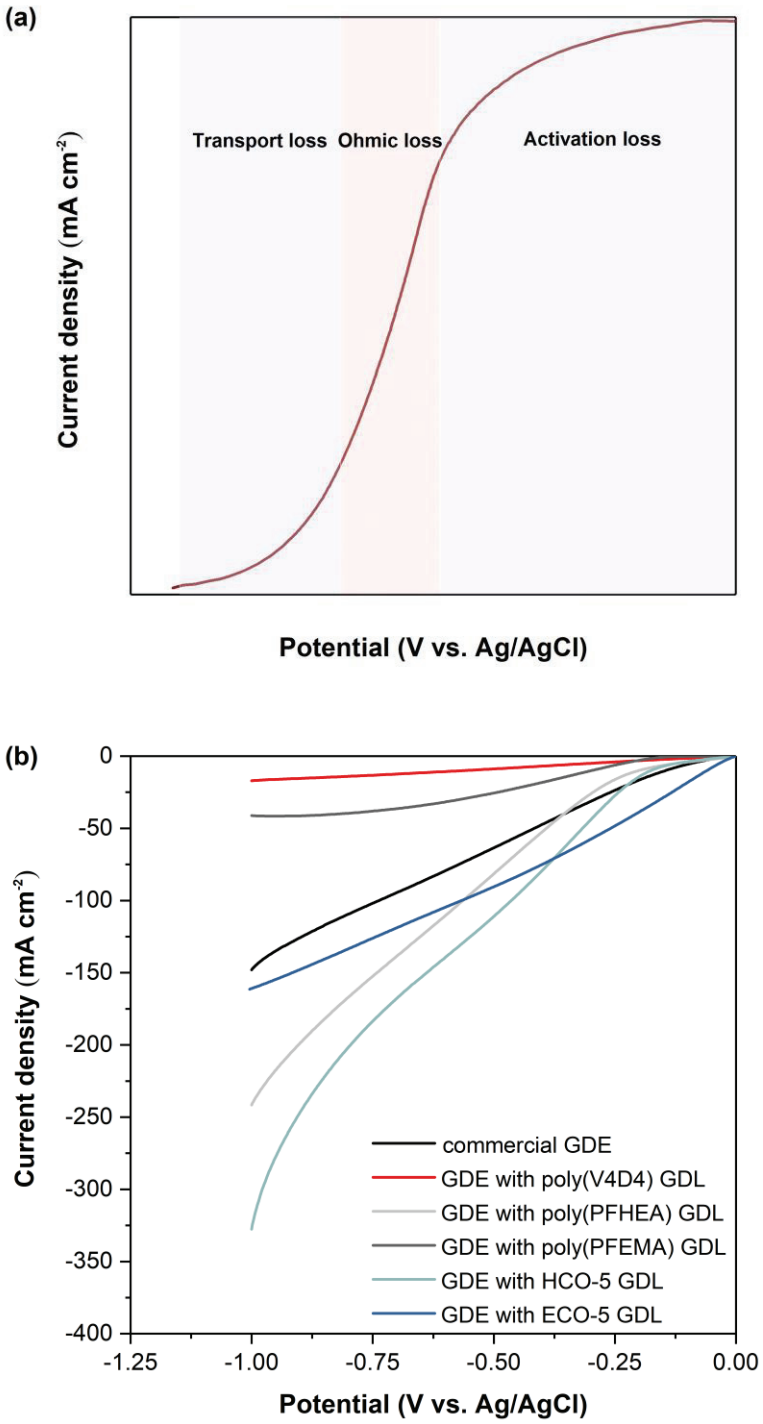

Figure 4.9. Polarization curves of GDEs with iCVD GDLs.

Tafel slopes calculated from Tafel plots also confirmed the results. Tafel slopes shown in Figure 4.10 were used to evaluate the oxidation-reduction reactions at current densities within the range of approximately 200 and 300 mA cm^{-2}. At low overpotentials ranging from 0.5 V to 0.75 V, Tafel slopes of GDEs with poly(V4D4), poly(PFHEA), and poly(PFEMA) homopolymer GDLs were smaller (79, 68, and 109 mV dec^{-1},

respectively) compared to commercial GDE (114 mV dec^{-1}). For GDEs with HCO-5 and ECO-5 copolymer GDLs, the Tafel slopes were determined as 89 and 118 mV dec^{-1}, respectively. iCVD GDEs with the exception of poly(PFEMA) GDL and ECO-5 GDL exhibited the low Tafel slope, which are close to the values of RT/F (~60 mV dec^{-1}) for ORR at low overpotential in alkaline solution (0.1 M-6 M KOH solution) as reported in the literature (Araújo et al., 2019).

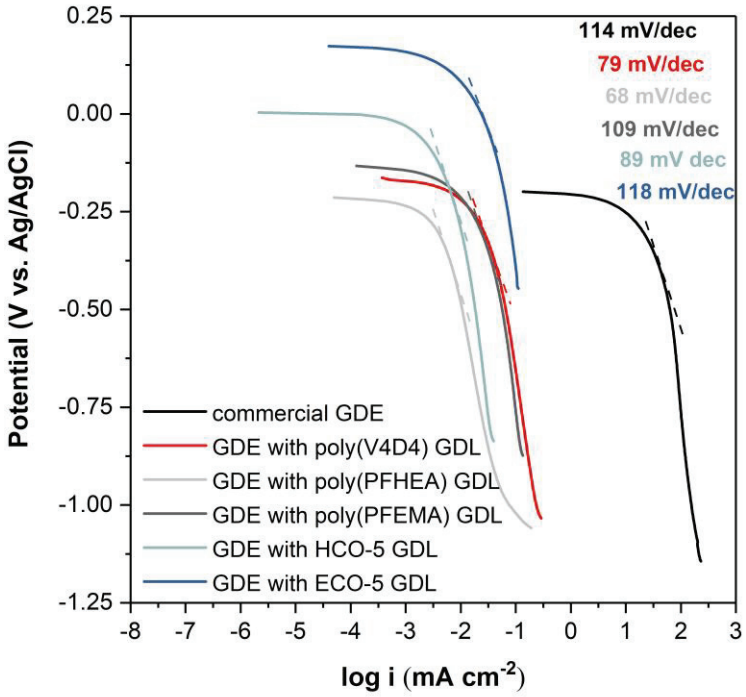

Figure 4.10. Tafel plots of commercial GDE, GDEs with homopolymer GDLs and their copolymers.

The low Tafel slope, in theory, indicates easy adsorption of the oxygen species on the surface during ORR process resulting in higher catalytic activity and lower polarization concentration (Araújo et al., 2019; Amin et al., 2015; Franzen et al., 2019). On the other hand, the Tafel slopes of GDEs with poly(PFHEA) GDL and ECO-5 GDL are close to the value of 2RT/F (~120 mV dec^{-1}), which is generally measured at high overpotentials (higher than 0.8V) in similar alkaline solutions (see in Table 4.5). This observation may be the result of mass-transport restriction during ORR process, which is consistent with the results reported in the literature for traditional GDEs (Jiang and Rajagopalan, 2011; Bursell and Björnbom, 1990). Therefore, a lower Tafel slope does not necessarily translate to higher oxygen permeability.

Table 4.5. Kinetic parameters of GDEs with iCVD GDLs

GDE	E_{corr}, mV	I_{corr}, mA	Tafel slope at low overpotentials, V dec^{-1}
commercial GDE	-200	21.2	1.14
GDE w/poly(V4D4) GDL	-165.4	40.24	0.79
GDE w/poly(PFHEA) GDL	-215	2.26	0.68
GDE w/poly(PFEMA) GDL	-0.13	3.88	1.09
GDE w/HCO-5 GDL	3.69	3.83	0.89
GDE w/ECO-5 GDL	173	2.54	1.18

EIS is a powerful tool to characterize impedances in a gas diffusion electrode. EIS analysis was performed at the Open Circuit Potential (OCP) from 10 kHz to 10^{-1} Hz in 6 M KOH solution. Nyquist plots, as shown in Figure 4.11(a), provide information on three types of GDE resistances; ohmic (solution), charge transfer, and diffusion resistances (Tada et al., 2017). Nyquist plots of GDEs consists of a single semi-circular curve and a diffusion drift which can be fitted using Randles and equivalent circuits model as shown in Figure 4.11(b). Randles model (Model 1) is generally used to describe simple electrochemical systems and includes only electrolyte resistance (R_e), charge-transfer resistance (R_{ct}) in medium-frequency region and Warburg impedance (Z_W) in the low-frequency region. The Warburg impedance is a key parameter to determine diffusion coefficients. The Warburg impedance is expressed as $Z_W=\sigma_w\omega^{-1/2}-j\sigma_w\omega^{-1/2}$ ($j^2 = -1$) and $Z_W= W^{-1}\sqrt{j\omega}$ where σ_w represents the Warburg impedance coefficient ($\Omega.s^{-1/2}$), ω is the angular frequency ($\omega = 2\pi f$) and W is Warburg impedance element ($S.s^{-1/2}$) (Choi et al., 2020). The Warburg impedance coefficient is related to the diffusion coefficient, and lower σ_w values indicate faster diffusion. In high-frequency region, the intercept in x-axis (Z_{real}) represents the ohmic (electrolyte) resistance (R_e), and the semicircle from high- to medium-frequency range is associated with the combination of charge transfer resistance (R_{ct}) and interfacial resistance (R_f). Model 2 expands Model 1 with the addition of interfacial resistance (R_f). Electrochemical parameters extracted from the fit to the equivalent circuit models are listed in Table 4.6. R_{ct} and R_f describe the kinetics of cell reaction. Lower values of R_{ct} and R_f indicate faster reaction kinetics (Cherian et al., 2013). As listed in Table 4.6, GDE with poly(V4D4) homopolymer GDL shows at least four orders of magnitude higher charge transfer resistance than other GDEs. The lowest value of $R_{ct} + R_f$ was obtained with HCO-5 GDL (1.50 Ω + 2.89 Ω), which is consistent with Nyquist plots as seen in Figure 4.11(a). For commercial GDE, W value describing the diffusion at the interface between the electrolyte and active material particles was determined to be 0.81. GDEs with poly(V4D4) GDL and HCO-5 GDL exhibited higher

W values (0.92 and 0.84, respectively) than commercial GDE indicating better oxygen transport.

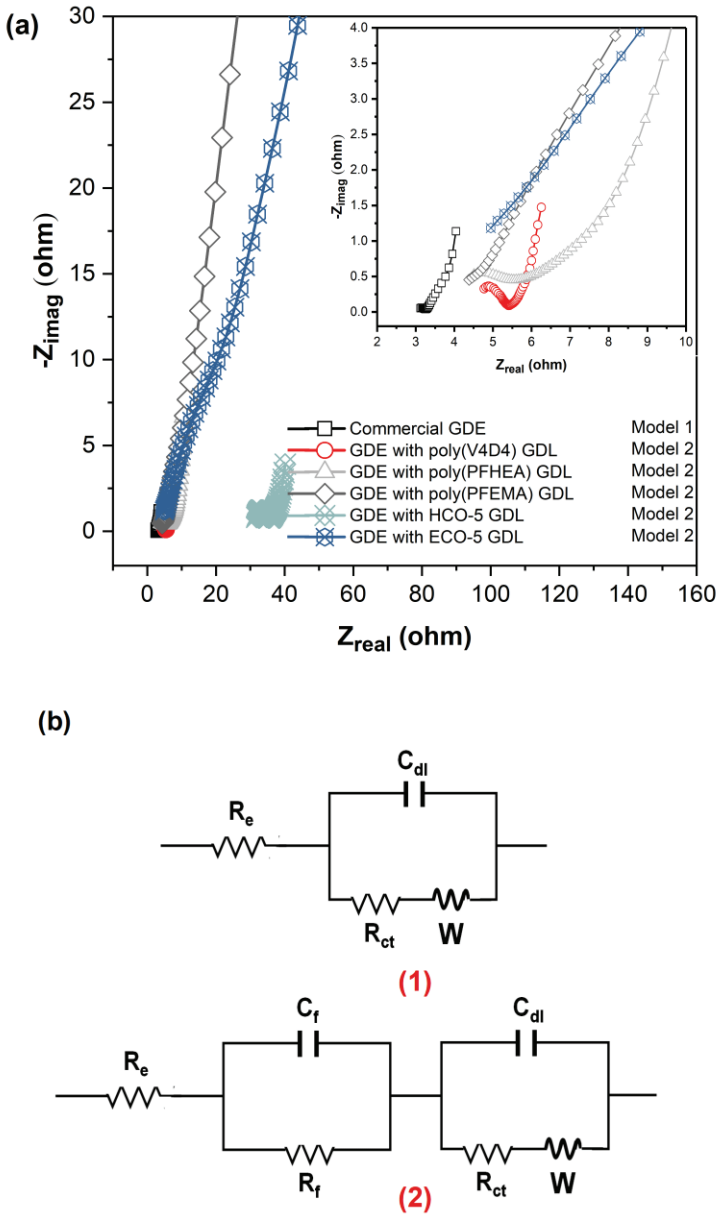

Figure 4.11. (a) Impedance spectra of GDEs, (b) equivalent electrical circuit models ((1) Model 1 (2) Model 2. Resistances (R_i), double layer capacitance (C_{dl}), Warburg impedance (W), electrolyte resistance (R_e), capacitance of film (C_i)).

The relation between real impedance (Z_{re}) and angular frequency (ω) in the low-frequency region is shown by using following equation (Liu et al., 2016; Khamsanga et al., 2019).

$$Z_{re} = R_e + R_{ct} + \sigma_w \omega^{-1/2} \quad (4.5)$$

$$D = R^2T^2/2A^2n^4F^4C^2\sigma_w^2 \quad (4.6)$$

where D is diffusion coefficient, R is the gas constant, T is the temperature, F is Faraday's constant, A is GDE area, n is the number of electrons per molecule, C is the molar concentration ion, and σ_w is the Warburg impedance coefficient. The Warburg impedance coefficient (σ_w) of GDE with HCO-5 GDL (0.32) is lower than that commercial GDE (0.37) indicating better diffusion as listed in Table 4.6.

Table 4.6. Electrochemical parameters extracted from the fit to the equivalent circuit models for EIS data

Sample	**R_e, Ω**	**R_{ct}, Ω**	**R_f, Ω**	**W, S.s$^{-1/2}$**	**Chi-square, χ^2**	**Warburg impedance coefficient, σ_w, Ω.s$^{-1/2}$**
Commercial GDE	3.55	0.14	-	0.81	0.8x10^{-4}	0.37
GDE w/poly(V4D4) GDL	4.67	6.55x10^4	0.71	0.92	1.84x10^{-4}	0.29
GDE w/poly(PFHEA) GDL	4.32	4.12	0.89	0.16	9.72x10^{-4}	1.52
GDE w/poly(PFEMA) GDL	4.84	4.42	0.68	0.79	4.1x10^{-4}	9.99
GDE w/HCO-5 GDL	32	1.50	2.89	0.84	5.53x10^{-5}	0.32
GDE w/ECO-5 GDL	4.85	3.28	7.79	1.5x10^{-2}	4.39x10^{-3}	12.32

For comparison, oxygen transport was also evaluated by Chronoamperometric method which is a useful tool to evaluate diffusion coefficients. Oxygen transport process in the electrode takes in three steps: (i) oxygen diffusion across GDL, (ii) dissolution of oxygen into the electrolyte film which create three-phase (gas-liquid-solid) boundary, (iii) diffusion of the dissolved oxygen through thin film to reactive site. Using the Cottrell equation (Yap and Doane, 1982; Zhou and Vander Poorten, 1995):

$$i(t) = nFAC^* \sqrt{\left(\frac{D}{\pi t}\right)} \quad (4.7)$$

where i is the limited current (A), n the number of electrons, F the Columbic charge (96,485 C mol^{-1}), A the surface area of the electrode (cm^2), D the diffusion coefficient (cm^2 s^{-1}), t the time (s) and C^* is the concentration of reactant (M), oxygen diffusion coefficients of for different samples can be calculated. The diffusion process is slow and dependent on the thickness of GDL; therefore, using ultra-thin iCVD GDLs should improve oxygen mass transport (Zhou and Vander Poorten, 1995). Oxygen diffusion

coefficients listed in Table 4.7 were calculated using EIS (Eq. (4.6)) and chronoamperometry (Eq. (4.7)) data for comparison. Although there are small differences in calculated diffusion coefficients between two methods, the results agree well with oxygen permeability measurements. The oxygen diffusion coefficient of poly(PFHEA) homopolymer GDLs is comparable to oxygen diffusion coefficient of commercial GDE. The oxygen diffusion coefficient for GDE with HCO-5 GDL in 6 M KOH solution is 20 times higher than that for commercial GDE and is almost four times higher than GDE with ECO-5 GDL making it a better candidate as gas diffusion layer for use in a GDE for a metal-air battery. Poly(V4D4-co-PFHEA) copolymer GDLs improve the oxygen transport due to a cross-linked network structure with the highly oxygen permeable siloxane and smaller fluorinated groups compared to poly(V4D4-co-PFEMA).

Table 4.7. Calculated oxygen diffusion coefficients for GDEs

GDEs	**Diffusion coefficient x 10^8, cm^2 s^{-1} (using EIS data)**	**Diffusion coefficient x 10^8, cm^2 s^{-1} (using Chronoamperometry data)**
commercial GDE	1.69	1.84
GDE w/poly(V4D4) GDL	26.8	22.5
GDE w/poly(PFHEA) GDL	2.32	3.94
GDE w/poly(PFEMA) GDL	0.23	0.28
GDE w/HCO 5 GDL	32.5	39.51
GDE w/ECO 5 GDL	8.64	6.76

4.4. Conclusions

Poly(V4D4), poly(PFHEA), poly(PFEMA) homopolymer, poly(V4D4-co-PFHEA), and poly(V4D4-co-PFEMA) copolymer coatings with different compositions were deposited via iCVD to be used as GDLs on gas diffusion electrodes for metal-air batteries. Oxygen and water vapor permeability of GDLs (350 ± 50 nm in thickness) were measured using 9.5 μm thick Psf support membranes. It was found that thin iCVD GDLs showed six to seven orders of magnitude lower water permeability (ranging from 0.261 x 10^{-15} to 0.581 x 10^{-15} mol m $m^{-2}s^{-1}Pa^{-1}$) than Psf membranes as previously reported (3.38 x 10^{-9} mol m $m^{-2}s^{-1}Pa^{-1}$) (Choi et al., 2019). In the literature, the water transmission rates of layer as GDL for GDE were reported as 11.16-811.99 g $m^{-2}day^{-1}$ (Amici et al., 2016a; Amici et al., 2016b; Xie et al., 2019). It was found that thin iCVD GDLs exhibited water

vapor transmission rates varying from 5.48 g m^{-2} day^{-1} to 11.32 g m^{-2} day^{-1}; between 2 and 150 times lower than commercial GDLs (Choi et al., 2019).

In addition, polymeric materials used as GDLs such as polyimide Kapton (Nicodemo et al., 1992), PVDF-HFP poly(vinylidene fluoride co-hexafluoropropylene) (Amici et al., 2016a), HDPE (high density polyethylene) (Xie et al., 2019), PTFE (polytetrafloroethylene) (Gilbert et al., 2004), etc. were reported have oxygen permeabilities between 0.01 and 4.21 Barrer. iCVD deposited GDLs exhibited higher oxygen permeability varying between 0.61 and 5.66 Barrer (0.204 x 10^{-15} and 1.895 x 10^{-15} mol m $m^{-2}s^{-1}Pa^{-1}$). iCVD deposited poly(V4D4-co-PFHEA) copolymer with a 1:1 ratio of V4D4:PFHEA showed an exceptional 10.5 Barrer (3.53 x 10^{-15} mol m $m^{-2}s^{-1}Pa^{-1}$), the highest oxygen permeability for similar GDLs reported in the literature. Electrochemical performance of GDEs with iCVD GDLs was investigated by polarization measurements, CV, and EIS analysis. CV analysis showed that poly(V4D4-co-PFHEA) GDLs are responsible for higher electrocatalytic activity for oxygen reduction compared to homopolymer and poly(V4D4-co-PFEMA) copolymer GDLs. Fabricated GDE electrodes with poly(V4D4-co-PFHEA) and poly(V4D4-co-PFEMA) exhibited higher oxygen reduction current densities (228.2 mA cm^{-2} and 189.2 mA cm^{-2}, respectively) compared to commercial GDE (132.7 mA cm^{-2}). The chronoamperometry measurements and EIS analysis also confirmed findings of oxygen permeability measurements. By combining siloxane and fluorinated matrix, poly(V4D4-co-PFHEA) copolymer GDLs provide enhanced oxygen transport and reduce moisture entrance significantly. Using the well-balanced properties of siloxane and fluorinated polymer chemistries, iCVD process is an excellent low-cost method for the fabrication of an oxygen-permeable hydrophobic gas diffusion layers for battery application.

CHAPTER 5

ROBUST FLUORINATED SILOXANE COPOLYMERS VIA INITIATED CHEMICAL VAPOR DEPOSITION FOR CORROSION PROTECTION

5.1. Introduction

A great deal of interest has arisen in polymer coatings for protection of metal surfaces against physical damage and corrosion in a wide range of applications. An ideal corrosion-resistant polymer coating should have excellent chemical stability, high mechanical strength, strong adhesion to the surface and outstanding passivation ability (Cao et al., 2018; Chen et al., 2019; Nautiyal et al., 2018; Rajitha, et al., 2020). One of the advantages of using polymeric coatings is the ability to tune the morphology, chemical composition, adhesion, and thickness of the coating to reduce the corrosion rate or minimize contact of liquid media with coated surface (Ikhe et al., 2016). Although polymer coatings are physical barrier layers between the substrate and corrosive media, complete corrosion prevention is still a challenge since water, ions, and oxygen from the external environment can gradually diffuse into polymer coatings. The use of superhydrophobic polymers is among the most effective methods to inhibit direct contact of the substrate with water (Ikhe et al., 2016; Cao et al., 2018; Caldona et al., 2020; Semiletov et al.; 2020). Fluorinated polymers are especially attractive as protective coatings due to their release and nonstick abilities, low abrasion and friction, low refractive index and surface energy, and antifouling properties (Chambers et al., 2006; Graham et al.; 2000; Munekata, 1988; Scheirs, 1997; Yang et al., 2008). The fluoropolymer matrix has a small carbon-fluorine bond polarization and provides extremely high bonding energy (Banks et al., 1994) making it a preferred candidate for applications requiring high-temperature and/or harsh-environment performance (He et al., 2015).

This chapter has been published as:
Cihanoğlu, G., Ebil, O. (2021) Robust fluorinated siloxanecopolymers via initiated chemical vapor deposition for corrosion protection, *Journal of Materials Science*, 56 (20), 11970-11987.

Commonly used methods to prepare fluoropolymer coatings for protection of metallic surfaces from the effects of corrosion degradation are etching (Emarati and Mozammel, 2020; Huang et al., 2015), lithography (Jeong et al., 2009; Martines et al., 2005), anodizing (Emarati aand Mozammel, 2020; Nishimoto et al., 2014), laser processing (Steele et al., 2013), coating of the surface using layer by layer deposition (Bravo et al., 2007; Chunder et al., 2009), electrodeposition (Liu et al., 2015), sol–gel deposition (Liang et al., 2014; Mahadik et al., 2016), and electrospinning (Han and Steckl, 2009; Li et al., 2009). Cao et al. reported a superhydrophobic film based on polydopamine functionalized with 1H,1H,2H,2H-perfluorodecanethiol (PFDT) on a brass surface deposited using hydrothermal method to improve long-term chemical and thermal stability of films (Cao et al., 2018). Vuoristo et al. demonstrated corrosion resistive polyvinylidene fluoride (PVDF), ethylene chlorotrifluoroethylene (ECTFE), perfluoroalkoxy alkane (PFA) and perfluoroethylenepropylene (FEP) coatings on low alloy steel Fe 37 (St 37) by thermal spray process (Leivo et al., 2004). Combining electroetching, anodizing, sealing and surface modification methods, Mozammel and Emarati prepared a superamphiphobic surface on Al alloy 2024 (AA 2024) and demonstrated strong barrier effect of fluoropolymer coatings (Emarati and Mozammel, 2020). Xu et al. applied chronoamperometric methods to produce perfluorinated lubricant/polypyrrole composite polymer coatings for protecting low alloy steel from the corrosion (Zhu et al., 2014). The increase in the coating thickness confines the electron and heat transfer, while achieving the chemical stability for metals in electronic devices, heat conductor, and heat exchangers (Liu et al., 2007; Ates et al., 2016; Zhao et al., 2019; Liang, 2001; Kaufman et al., 1980; Roldughin and Vysotskii, 2000). However, most of these methods still suffer from thickness nonuniformity, conformality problems due to poor surface wetting, pinhole and other defects due to fast solvent evaporation etc. limiting their corrosion protection performance. Chemical Vapor Deposition (CVD) offers the smoothest conformal, cross-linked polymer coatings with good thickness control due to vapor phase polymerization process (Chen et al., 2019; Chan and Gleason, 2005; Coclite et al., 2009). Recently, CVD process has been used for the fabrication of fluorinated films to improve corrosion resistance of metals in aggressive media. Ishizaki et al. used microwave Plasma Enhanced Chemical Vapor Deposition (PECVD) process to fabricate superhydrophobic coatings on magnesium alloy AZ31 to improve chemical stability and corrosion resistance of AZ31 alloy (Ishizaki et al., 2010).

However, the corrosion rates still remain high for effective protection and fluorinated homopolymer films do not achieve chemical/mechanical robustness required in harsh environments such as strong organic solvents, acids, bases, and oxidants (Chen et al., 2019; Zhu et al., 2020). An ideal protective polymer coating should provide corrosion protection in such environments for weeks and months without any measurable change in its chemical and mechanical properties. A facile approach employed for the fabrication of a chemically and mechanically robust polymer coatings involves crosslinking and/or establishing covalent bonding between the coating and the substrate (Grignard et al., 2011; Seok et al., 2018; Achyuta et al., 2009; Zhu et al., 2020) or using stacked polymer films (Yoo et al., 2013). Ye et al. demonstrated superhydrophobic bilayer polymer coatings consisting of highly cross-linked polyethylene glycol diacrylate (PEGDA) bottom layer and nanostructured poly(perfluorodecyl acrylate-co-ethylene glycol diacrylate) (poly(PFDA-co-EGDA)) top layer on copper, Si wafer and polystyrene via iCVD. It was demonstrated that highly crosslinked film provided an effective oxygen barrier and good corrosion resistance (Chen et al., 2019).

Employing mechanically flexible and hydrolytically stable polysiloxane films such as poly(V4D4) in copolymer structure leads to improved chemical and mechanical properties (Achyuta et al., 2009; Seok et al., 2018; Grignard et al., 2011; Goksel and Akdogan, 2019). Copolymer films of ionically conductive polysiloxane and hydrophobic fluoropolymers can enhance conduction and improve long-term stability while inhibiting the direct contact of the metal with medium, thus suppressing aggressive corrosion. Lee et al. fabricated a crosslinked organosilicon-acrylate copolymer thin film consisting of V4D4 and cyclohexyl methacrylate (CHMA) via iCVD process to provide a moisture barrier with improved mechanical stability (Seok et al., 2018). Murthy et al. used iCVD to synthesize a copolymer film with V3D3 monomer and hexavinyldisiloxane (HVDS) as a spacer for a potential application in neutral probe fabrication and reported enhanced chemical durability in both polar and nonpolar solvents such as tetrahyrofuran, acetone, isopropyl alcohol, and dimethyl sulfoxide due to its highly cross-linked nature (Achyuta et al., 2009). Kwak et al. fabricated a copolymer using poly(V4D4) and poly(PFDMA) (poly-perfluorodecyl methacrylate) via iCVD to improve the mechanical durability of the film fluoropolymer films (Lee et al., 2019). However, only a few studies related to iCVD poly(V4D4) films in literature have reported their physical properties such as passivation performance (Zhao et al., 2019). Gleason and co-workers evaluated chemical stability and corrosion resistance of iCVD fabricated homopolymer films of polydivinylbenzene

(poly(DVB)), poly(V3D3), poly(V4D4), and poly(1H,1H,2H,2H-perfluorodecyl acrylate) (poly(PFDA)). They reported that poly(V3D3) and poly(V4D4) films exhibited excellent stability and reduced surface corrosion due to crosslinked covalent organic network (Zhao et al.; 2019).

Here, we report highly crosslinked, hydrophobic copolymers of V4D4 and PFHEA/PFEMA synthesized via iCVD for corrosion protection of metals. Fabricated hydrophobic films showed excellent durability in various organic solvents and were found to be very effective for corrosion protection of metal and other substrates. The low process temperature and extreme flexibility of iCVD process enable fine tuning of physical and chemical properties of polymer films making it very attractive for the fabrication of self-cleaning, corrosion-resistant, transparent barrier layers on a large variety of substrates, including temperature sensitive materials.

5.2. Experimental

5.2.1. Materials

Analytical grade chemicals, 2,4,6,8-tetramethyl-2,4,6,8 tetravinylcyclotetra siloxane (V4D4, Sigma-Aldrich, 97%), 2-(perfluorohexylethyl)acrylate (PFHEA, Fluoryx Inc.) and 2-(perfluoroalkyl) ethylmethacrylate (PFEMA, Fluoryx Inc.) as monomers, and tert-Butyl peroxide (TBPO, Sigma-Aldrich, 98%) as initiator were used in fabrication of polymer thin films. Organic solvents such as tetrahydrofuran (THF, Panreac, 99.9%), dichloromethane (DCM, Sigma-Aldrich), N,N-dimethylformamide (DMF, Sigma-Aldrich), chloroform (Sigma-Aldrich), diethyl ether (Sigma Aldrich), 2-propanol (Sigma-Aldrich, ≥99.5%), acetone (Sigma-Aldrich, ≥99.5%), ethanol (Sigma-Aldrich, ≥99.8%), toluene (Sigma-Aldrich, ≥99.5%) and hydrogen peroxide (H_2O_2, Sigma-Aldrich) were used in durability tests. Commercially available copper and zinc plates (0.8 cm x 1.5 cm) were used for corrosion tests. Metal plates were polished with emery paper and then cleaned using 2-propanol (Sigma-Aldrich, ≥99.5%) before coating process.

5.2.2. Fabrication of Polymer Coatings

For the fabrication of polymer coatings, a custom-built iCVD system was used. The deposition chamber was prismatic in shape with a width of 30 cm and a height of 4 cm. The top of the reactor was covered with a 2.5 cm thick quartz plate. The reactor was equipped with a filament array which was suspended 2.5 cm over the substrate to supply thermal energy for the decomposition of initiator. Nichrome filaments were resistively heated via AC power supply. The substrate temperature was controlled by an external circulator (WiseCircu - refrigerated bath circulator). The reactor pressure was controlled using a throttling butterfly valve (MKS Model 253). The vacuum was provided via a rotary vane pump (BSV10, Baosi) equipped with a cold trap. Thin-films of poly(V4D4), poly(PFHEA) and poly(PFEMA) homopolymers, and poly(V4D4-co-PFHEA) and poly(V4D4-co-PFEMA) copolymers were fabricated on metal and crystalline silicon (c-Si) substrates. In order to obtain sufficient vapor pressure, PFHEA and PFEMA monomers were heated to 65 ^{o}C and 95 ^{o}C, respectively. Monomer vapors were metered into the chamber through mass-flow controllers (MKS 1479A). For poly(V4D4) deposition, V4D4 monomer was heated to 90 ^{o}C and fed into the chamber through a special mass-flow controller (MKS 1150C). TBPO was introduced into the reactor at room temperature through a mass-flow controller (MKS 1479A). Reactor pressure was maintained at 250 mTorr throughout this study. The substrate and filament temperature were adjusted for optimum deposition rate for homopolymers and copolymers. The filament temperature was set to 250 ^{o}C for PFEMA homopolymer, and fixed at 300 ^{o}C for all other homopolymer and copolymer film depositions. Thicknesses of homopolymer films on c-Si varied from 1 to 1.8 μm. The average thickness of iCVD deposited polymer films on metal substrates was 250 nm to evaluate the corrosion resistance. The deposition conditions for homopolymers and copolymers are summarized in Table 5.1.

Table 5.1. Process conditions for iCVD deposited homopolymers and copolymers

Sample name	**F_{V4D4} sccm**	**F_{PFHEA} sccm**	**F_{PFEMA} sccm**	**F_{TBPO} sccm**	**P_{total} mTorr**	**$T_{substrate}$ ^{o}C**
poly(V4D4)	0.32	-	-	0.16		45
poly(PFHEA)	-	0.39	-	0.13		25
poly(PFEMA)	-	-	0.20	0.025	250	35
poly(V4D4-co-PFHEA)	0.22	0.22	-	0.66		45
poly(V4D4-co-PFEMA)	0.22	-	0.22	0.66		45

5.2.3. Film Characterization

The thicknesses of fabricated films were measured using an Mprobe-Vis20 system with a spectral range of 400-1100 nm, 2 mm spot size and 2 nm measurement accuracy. Fourier Transform Infrared spectroscopy (FTIR) analysis was performed using a Perkin Elmer Inc.-Spectrum BX FTIR Spectrometer for the evaluation of the quality and chemical composition of monomers and fabricated polymer films. The spectra were measured from 4000 to 650 cm^{-1} with a resolution of 4 cm^{-1} and accumulating over 20 scans. All spectra were baseline corrected and thickness normalized. Surface morphologies of fabricated iCVD films were investigated using Scanning Electron Microscopy (SEM) (FEI Quanta250 system). Water Contact Angle (WCA) measurements were conducted to investigate the hydrophilicity of the surface for fabricated iCVD films with a Theta Optical Tensiometer.

5.2.4. Chemical Stability and Durability Tests

The durability of poly(V4D4), poly(PFHEA), poly(PFEMA) homopolymers and poly(V4D4-co-PFHEA) and poly(V4D4-co-PFEMA) copolymer films in various organic solvents was investigated following procedures described in literature (Seok et al., 2018). Solubility tests were performed by immersing iCVD coated substrates in various organic solvents including tetrahydrofuran (THF), 2-propanol (IPA), acetone, hydrogen peroxide (H_2O_2), toluene, dichloromethane (DCM), N,N-dimethylformamide (DMF), chloroform and diethyl ether for 30 min and then drying at 70 ^oC for 1 h under vacuum. Adhesion to silicon wafer and optical glass was tested as described previously in literature (Ozpirin and Ebil, 2018). A cellophane adhesive tape was applied on the film surface and then rapidly removed from the surface at the angle that was normal to the coated surface. The percentage of delamination was calculated by dividing the test surface into equally spaced grids. The coating adhesion test was evaluated by visual inspections using a reflectometer and optical microscope. The thickness of each film before/after the adhesion test was measured.

5.2.5. Electrochemical Tests

Anti-corrosion performance of iCVD coatings was evaluated using a Potentiostat/Galvanostat/ZRA (Gamry Model 22162) with a tripolar electrode measurement apparatus consisting of a Pt wire as counter electrode, a saturated Ag//AgCl reference electrode and polymer film coated Cu or Zn metal plate as working electrode with an exposed area of 1.2 cm^2. Polarization curves and electrochemical impedance spectra were obtained in 5 wt.% NaCl solutions at room temperature under open-circuit conditions. iCVD coated Cu and Zn plates were immersed in 5 wt.% NaCl solution for 30 min for stabilization before the polarization measurements. Potentiodynamic polarization was performed within a potential range of Open-Circuit Potential (OCP) ± 250 mV at a scan rate of 1 mV s^{-1}. Corrosion parameters such as corrosion potential (E_{corr}), corrosion current density (I_{corr}), polarization resistance (R_p), and anodic/cathodic Tafel slopes (β_a/β_c) were calculated by using the potentiodynamic curves. For EIS analysis, AC impedance (OPC ± 5 mV) was applied at a frequency range of 100 mHz to 10 kHz with a sinusoidal signal perturbation of 10 mV and 5 points per decade. Similar to potentiodynamic polarization, all iCVD coated samples were immersed into NaCl solution for 30 min before the impedance measurements.

5.3. Results and Discussion

5.3.1. FTIR Analysis of Perfluorinated Polymer Coatings

Chemical compositions of PFHEA and PFEMA monomers and homopolymers were investigated by FTIR analysis, as shown in Figure 5.1. The characteristic peaks of C=O at 1745 cm^{-1} are clearly shown in PFHEA and PFEMA spectra. The three peaks in 1140-1240 cm^{-1} region indicate stretching of $-CF_2$ and $-CF_3$ end groups. The intensity of characteristic peaks representing strong bending and stretching of C=C at 985 cm^{-1}, 995 $cm^{-1}$and 1640 cm^{-1} disappear due to complete free-radical polymerization (Wang et al., 2010; Zhang et al., 2014a). Table 5.2 lists FTIR absorption frequencies and peak intensities of both PFHEA and PFEMA homopolymers (Wang et al., 2010; Yin et al., 2017).

Table 5.2. FTIR absorption band assignments for PFHEA and PFEMA

Group	iCVD film (cm^{-1})	literature (cm^{-1})	intensity	Ref.
$-CF_3$ vibration wag	700	700	medium	Yin et al., 2017
$=CH_2$ wag	735	720-740	medium	Trujillo et al., 2009
$-CF_3$ stretch	1143	1142	medium	Yin et al., 2017
$-CF_2$ absorption vibration stretch	1232	1200-1240	medium	Yin et al., 2017
$-CH_2$ and CH_3 deformation	1415	1200-1500	medium	Gedde, 1999
C=C stretch acrylic double bond	1640	1630-1640	medium	Wang et al., 2010
C=O stretch in ester group	1741	1735-1750	strong	Wang et al., 2010
CH stretch of vinyl bond	3000	2995-3020	medium	O'Shaughnessy et al., 2006

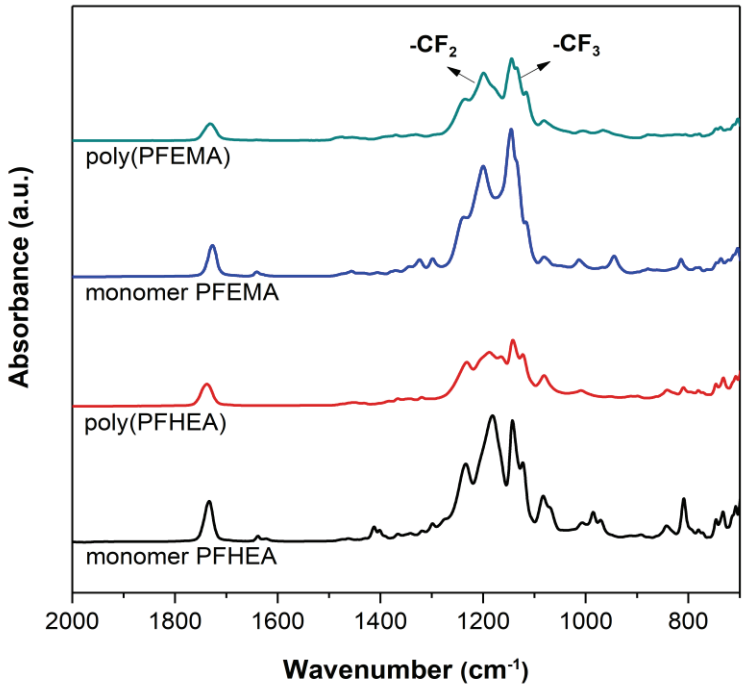

Figure 5.1. FTIR spectra of (a) PFHEA monomer and (b) poly(PFHEA) film synthesized in iCVD system.

5.3.2. Chemical Stability of Perfluorinated Polymer Coatings

Determination of the chemical stability of iCVD films in various solvents is essential to evaluate their corrosion protection performance. The hydrolysis of the ester group is extremely slow due to the hydrophobic character of fluorinated polymers making them attractive candidates for protective materials (Grignard et al. 2011). Most of previous studies in literature related to hydrophobic films as protective layers have solely used WCA measurements to claim good chemical stability. Chemical stability of iCVD

homopolymer films deposited on c-Si wafer was measured by the change in film thickness after immersion in various organic solvents including THF, DCM, acetone (polar aprotic solvents), IPA, ethanol, H_2O_2 (polar protic solvents), toluene, chloroform and diethyl ether (nonpolar solvents) for 30 min. Figure 5.2 shows relative thickness change and WCA values of iCVD poly(PFHEA) and poly(PFEMA) homopolymers after immersion in solvents. Even without any crosslinking or surface grafting, both iCVD films showed good durability in organic solvents. The relative thickness change of poly(PFHEA) homopolymer films was less than 5% with the exception of diethyl ether in which a 10% thickness change was measured after immersion. On the other hand, poly(PFEMA) films showed greater durability with less than 1.5% thickness loss except THF and diethyl ether in which 13% and 15% changes were measured, respectively. The change in WCA for homopolymer films after immersion in solvent are also shown in Figure 5.2. The lowest WCA for poly(PFHEA) homopolymer was measured after immersion in diethyl ether in which the highest thickness reductions was also observed. Overall, WCA values did not change significantly and varied between 87^o and 99^o. Compared to poly(PFHEA), iCVD deposited poly(PFEMA) films are more hydrophobic with a WCA of 146^o vs 102^o for poly(PFHEA). Immersion in solvents resulted in slight reduction in WCA of poly(PFEMA) except THF and diethyl ether in which WCA changed significantly. This observation is also in line with thickness measurements shown in Figure 5.2(b). However, poly(PFEMA) homopolymers still showed hydrophobicity after immersion test. The results indicate that iCVD fluorinated homopolymer films exhibit good resistivity against organic solvents.

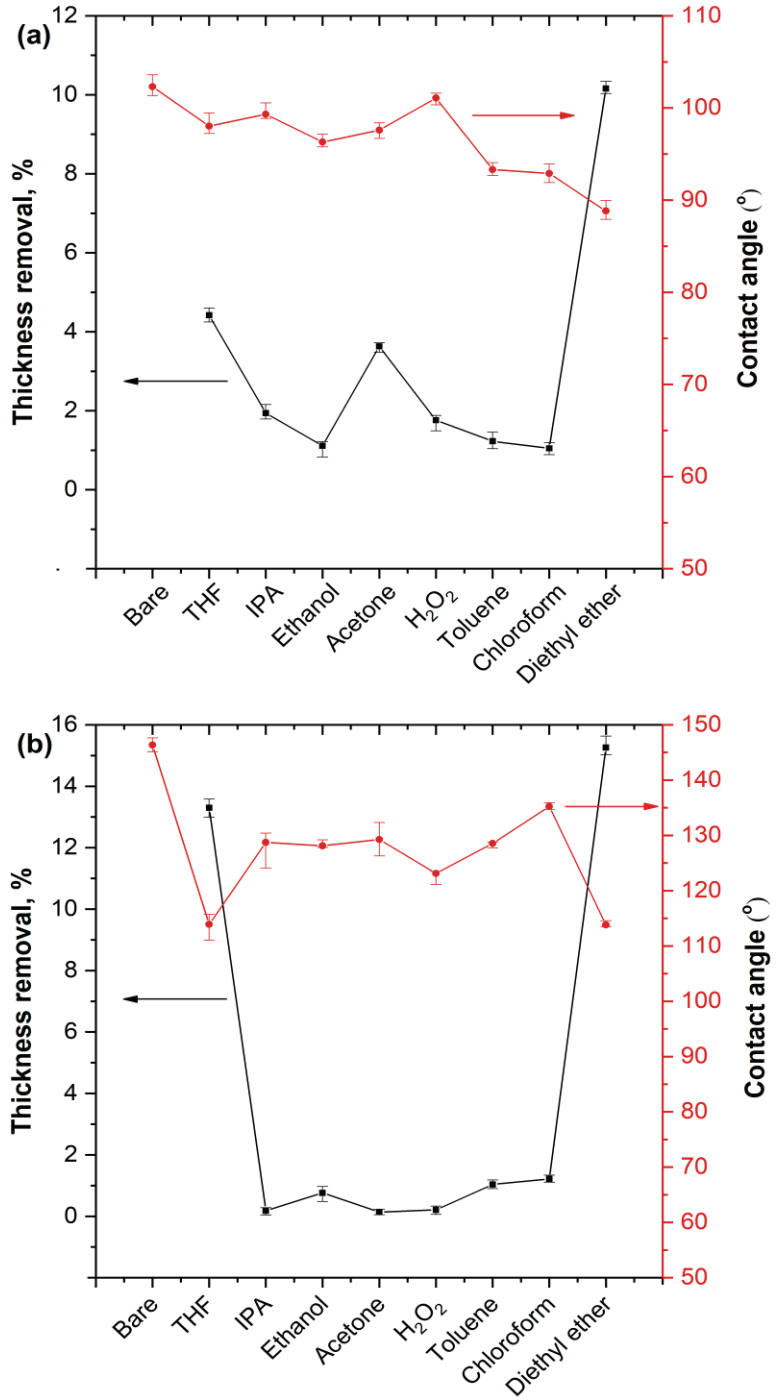

Figure 5.2. Relative thickness change and absolute WCA values for (a) poly(PFHEA) and (b) poly(PFEMA) homopolymer films after immersion in various solvents.

The solubility resistance of fluorinated homopolymer coatings (both poly(PFHEA) and poly(PFEMA)) was estimated by measuring the loss of thickness after immersion in solvents. There were no significant changes in measured thicknesses indicating no swelling and or dissolving of the films. Both poly(PFHEA) and poly(PFEMA) films passed all solubility tests. More details about thickness

measurements are given in online resource Table 5.3. FTIR spectroscopy was also used to investigate durability of poly(PFHEA) and poly(PFEMA) homopolymers films after immersion tests, shown in Figure 5.3. Although peak intensities were slightly decreased, all characteristic peaks were still visible after the immersion in diethyl ether confirming durability of homopolymers in most organic solvents.

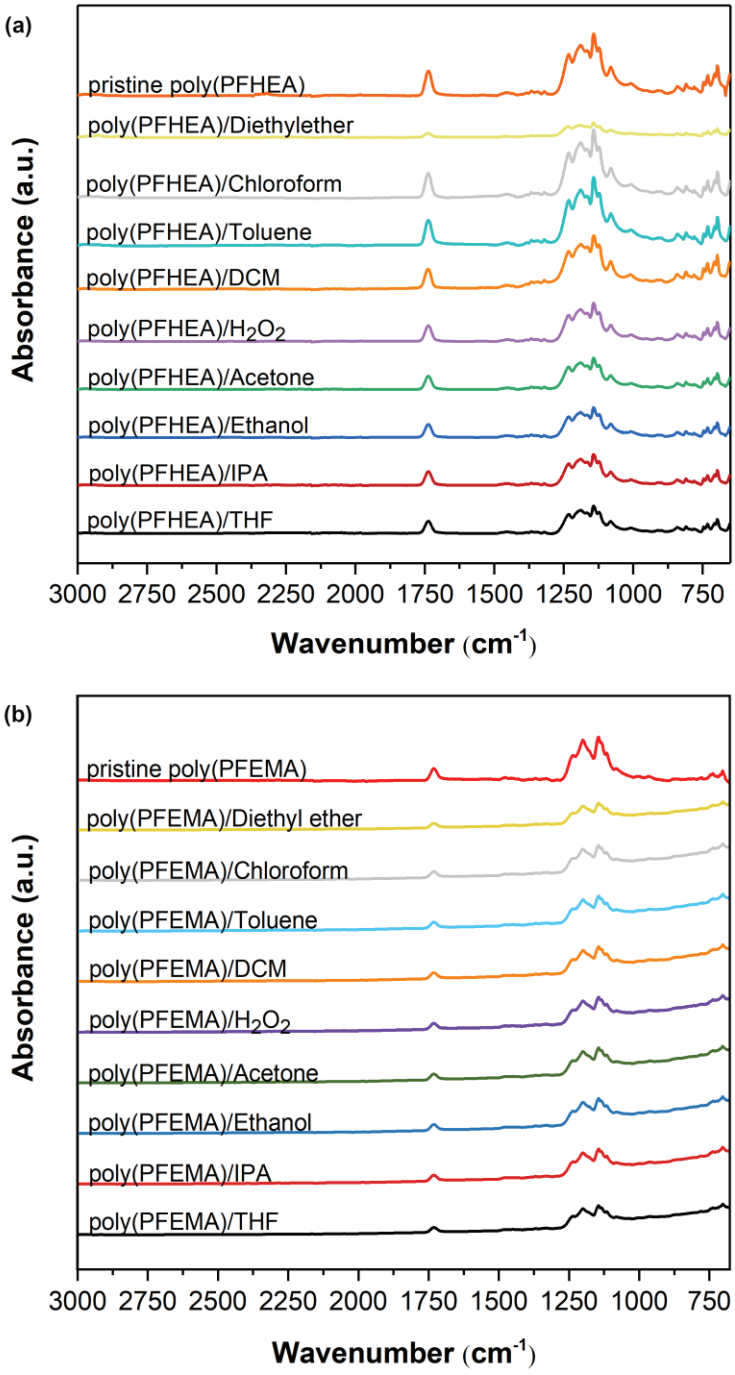

Figure 5.3. Changes in the FTIR spectra before and after solubility tests (a) poly (PFHEA) (b) poly(PFEMA) films.

Table 5.3. Film thickness measurements after immersion in various solvents

Solvent	poly(PFHEA) film			poly(PFEMA) film		
	Initial thickness (µm)	**Final thickness (µm)**	**Removal (%)**	**Initial thickness (µm)**	**Final thickness (µm)**	**Removal (%)**
THF	1.7547	1.6770	4.42	0.9891	0.8572	13.3
IPA	1.7612	1.7271	1.94	1.0305	1.0286	0.18
EtOH	1.8330	1.8128	1.11	1.0292	1.0213	0.76
Acetone	1.9166	1.8471	3.63	0.9876	0.9862	0.14
H_2O_2	1.9612	1.9266	1.76	1.0146	1.0125	0.21
Toluene	1.7988	1.7767	1.23	1.0159	1.0053	1.04
Chloroform	1.6447	1.6275	1.05	1.0450	1.0087	1.22
Diethyl ether	1.6291	1.4636	10.16	1.0212	0.8855	15.26

In addition to simple immersion tests in various organic solvents, we also evaluated the durability and chemical stability of these homopolymer films after thermal and ultrasonic treatment with mechanical mixing in dichloromethane (DCM) which is a very strong solvent. Poly(PFHEA) and poly(PFEMA) films were heat treated at 70 ^{o}C for 1 hour under vacuum. Sonication was carried out in DCM for 30 min. The change in film thickness and WCA measurement after the test are shown in Figure 5.4. Both homopolymer films were completely removed or dissolved in DCM after 30 min ultrasonic treatment. Polymer films were found out to be durable in simple DCM immersion. Mechanical mixing during immersion in DCM seems to reduce durability of the films slightly while thermal annealing before test did not improve durability in DCM. Poly(PFEMA) homopolymer films showed slightly reduced WCA values after immersion in DCM with and without mechanical mixing while WCA sharply decreased with mechanical mixing for poly(PFHEA) homopolymer.

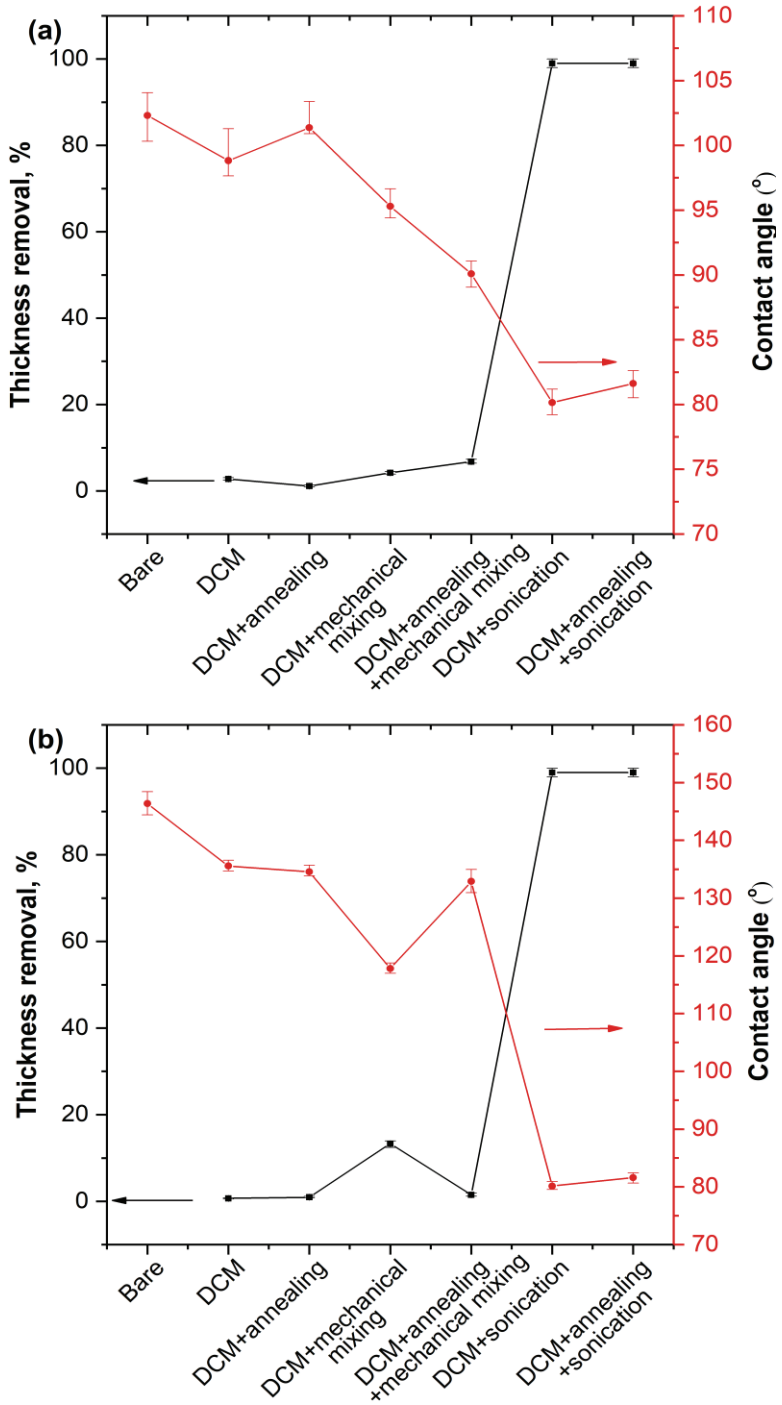

Figure 5.4. Relative thickness change and absolute WCA values for (a) poly(PFHEA) and (b) poly(PFEMA) homopolymer films after immersion in DCM.

FTIR analysis of homopolymer films showed all characteristic peaks after immersion in DCM with or without mechanical mixing and also confirmed complete removal of the film from the substrate surface with ultrasonic treatment, as shown in Table 5.4 and Figure 5.5. It seems ultrasonic treatment is a very effective method to remove these homopolymer films from the surface.

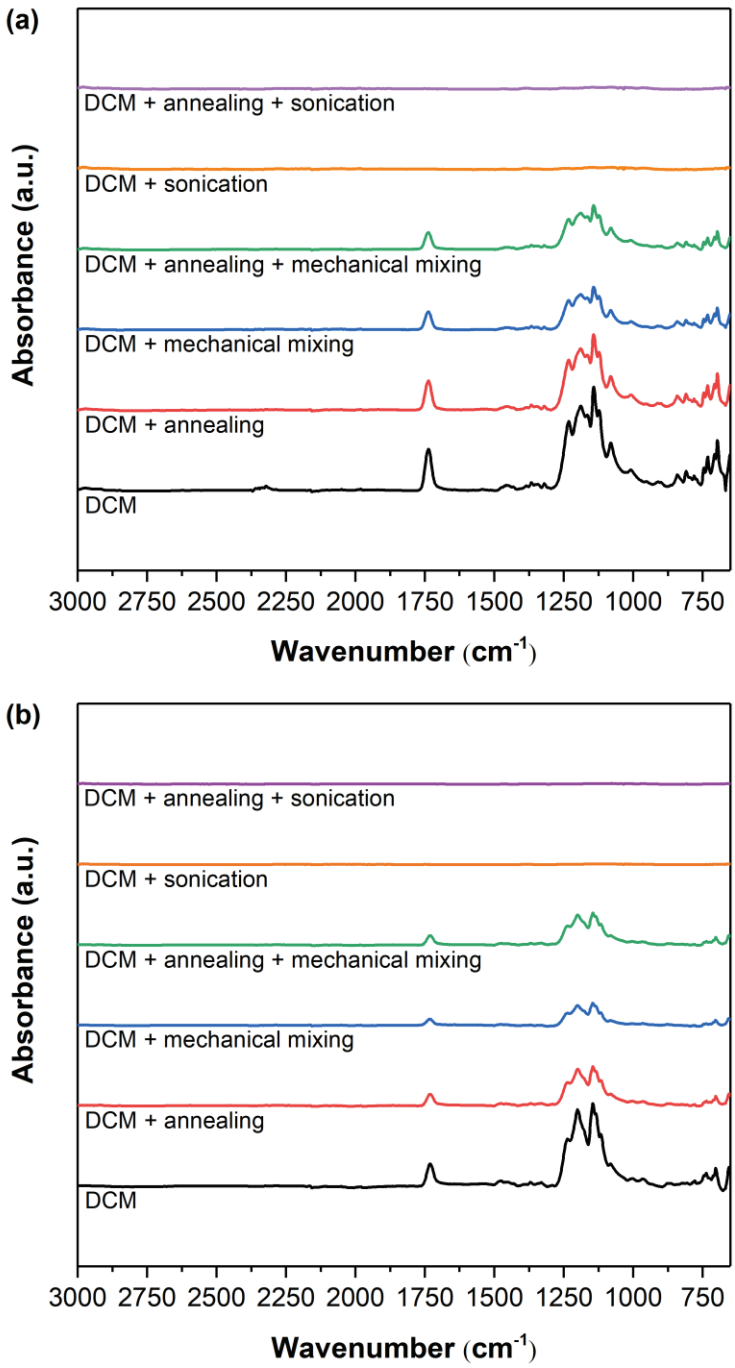

Figure 5.5. Change in FTIR spectra of (a) poly(PFHEA) and (b) poly(PFEMA) films after annealing, mechanical mixing and sonication.

Table 5.4. Film thickness measurements before and after immersion in dichloromethane (DCM)

Solvent	poly(PFHEA) film			poly(PFEMA) film		
	Initial thickness (µm)	Final thickness (µm)	Removal (%)	Initial thickness (µm)	Final thickness (µm)	Removal (%)
DCM	1.7612	1.7129	2.74	0.9968	0.9898	0.67
DCM+annealing	1.9857	1.9634	1.12	1.0101	1.0005	0.95
DCM+mechanical mixing	1.8602	1.7825	4.18	1.0276	0.8905	13.31
DCM+mechanical mixing+annealing	1.8673	1.7409	6.77	1.0282	1.0128	1.49
DCM+sonication	1.8398	no measured	~100	1.0043	no measured	~100
DCM+sonication+ annealing	1.8603	no measured	~100	0.9985	no measured	~100

5.3.3. FTIR Analysis of Crosslinked Copolymer Coatings

In addition to poly(PFHEA) and poly(PFEMA) homopolymers, two different series of crosslinked copolymer thin films were synthesized via iCVD process by copolymerization of V4D4 with acrylic (PFHEA) and methacrylic (PFEMA) monomers. Chemical structures and FTIR spectra of monomers and copolymers in iCVD process are shown Figure 5.6 and Figure 5.7, respectively. For poly(V4D4) homopolymer, the peaks between 1064 cm^{-1} and 1073 cm^{-1} in FTIR spectrum represent asymmetric Si-O-Si stretching related to eight-member siloxane ring in network configuration and the peak at 1260 cm^{-1} shows the strong Si-CH_3 symmetric bending (Achyuta et al., 2009; O'Shaughnessy et al., 2006; Trujilo et al., 2009). In poly(V4D4-co-PFHEA) and poly(V4D4-co-PFEMA) of FTIR spectra, the shoulders at 1140 cm^{-1} and 1240 cm^{-1} are representative of C-F chains and provide evidence of a copolymer with crosslinked network structure. Also, the peak at 1740 cm^{-1} corresponds to stretching C=O in the acrylic group or methacrylic group (Wang et al., 2010; Yin et al., 2017). By adjusting the flow rate of the fluorinated monomer, the composition of copolymers can be controlled. However, there may be a difference between feed composition and copolymer composition due to the monomer adsorption rate on the surface (Gleason, 2015).

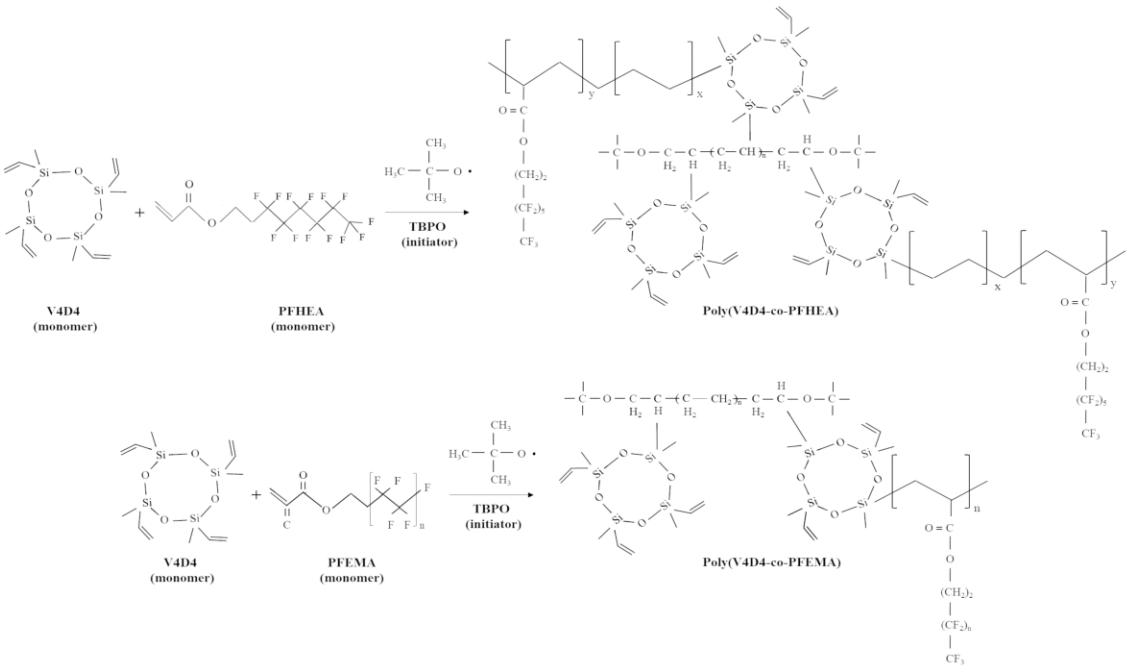

Figure 5.6. Chemical structures of monomers, initiator radical and copolymers in iCVD process.

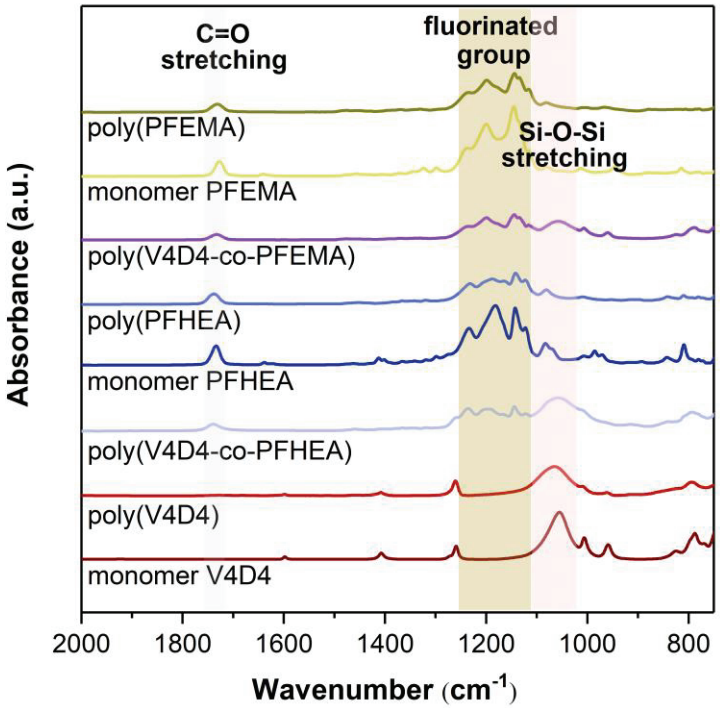

Figure 5.7. FTIR spectra of poly(V4D4), poly(PFHEA), poly(PFEMA) and their copolymers.

5.3.4. Chemical Stability of Crosslinked Copolymer Coatings

Similar to homopolymer films, the chemical stability of poly(V4D4-co-PFHEA) and poly(V4D4-co-PFEMA) copolymers deposited on c-Si substrates was evaluated by the change in film thickness after immersion in strong organic solvents as described in the literature (Seok et al., 2018). The relative changes in thicknesses of homopolymers and copolymer films before and after immersion in THF, DCM, DMF, chloroform and diethyl ether for 30 min are shown in Figure 5.8.

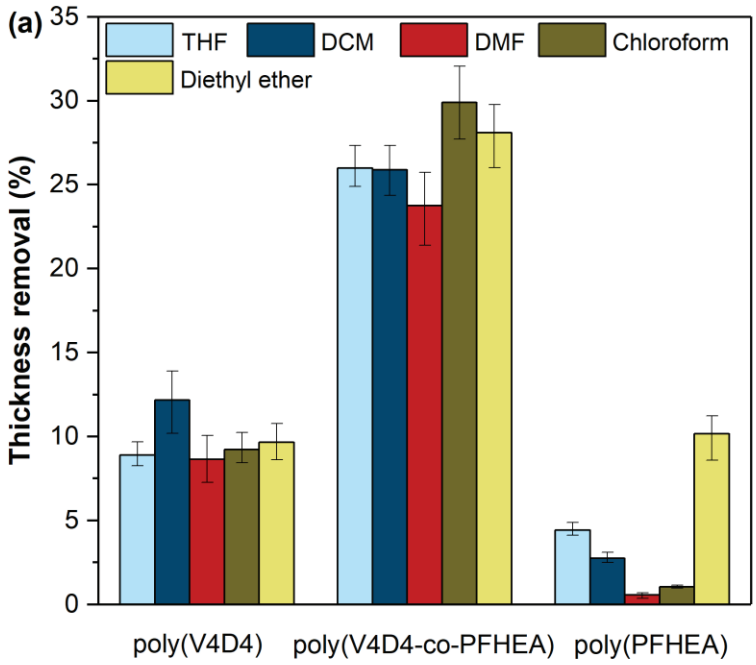

Figure 5.8. The relative change in film thickness for copolymers with varying (a) PFHEA and (b) PFEMA content in the film.

(Cont. on next page)

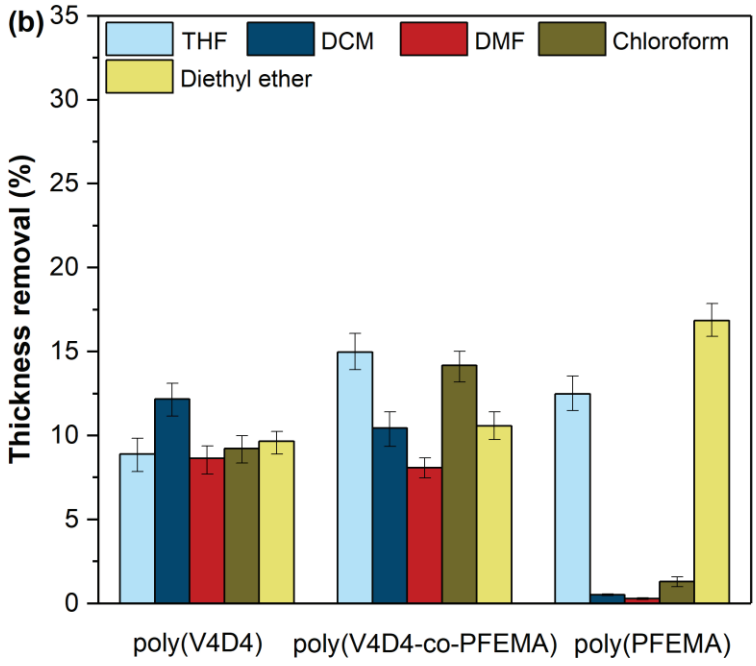

Figure 5.8. Cont.

The monomer flow rate ratios in copolymerization process are given in Table 5.1. Poly(V4D4-co-PFHEA) polymers showed up to 30% thickness loss, while the maximum thickness loss was around 15% for poly(V4D4-co-PFEMA). This might be related to the differences between the length of the pendent perfluorocarbon chains (n_{PFEMA} = 4–10; n_{PFHEA} = 6) (Tsibouklis et al., 2000; Wang et al., 2010). It is also possible that formation of small molecules or short side chains due to certain process conditions might lead to insufficient cross-linking of polymer making it sparingly soluble (Achyuta et al., 2009). In addition to chemical composition, the durability of copolymer films in a solvent is also affected by overall quality and uniformity of the film as well as the surface properties of the substrate on which the copolymer is deposited. The chemical stability of the films was also analyzed after the tests. FTIR analysis confirmed V4D4 and PFHEA/PFEMA moieties for both copolymer films after solubility test, indicating durability good resistance of iCVD copolymer films against strong solvents, as shown in Figure 5.9.

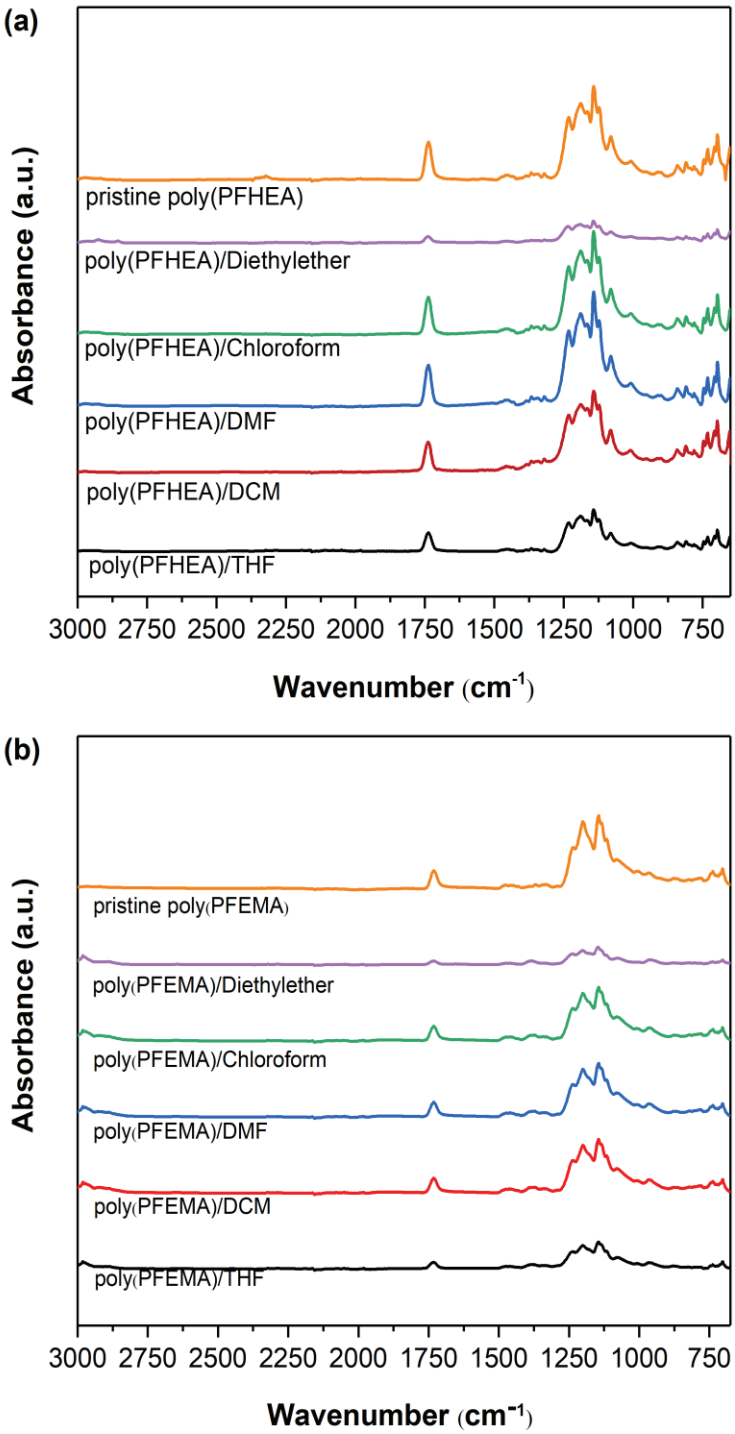

Figure 5.9. Changes in FTIR spectra of (a) poly(PFHEA), (b) poly(PFEMA), (c) poly(V4D4), (d) poly(V4D4-co-PFHEA) and (e) poly(V4D4-co-PFEMA) before and after dissolution test in various solvents.

(Cont. on next page)

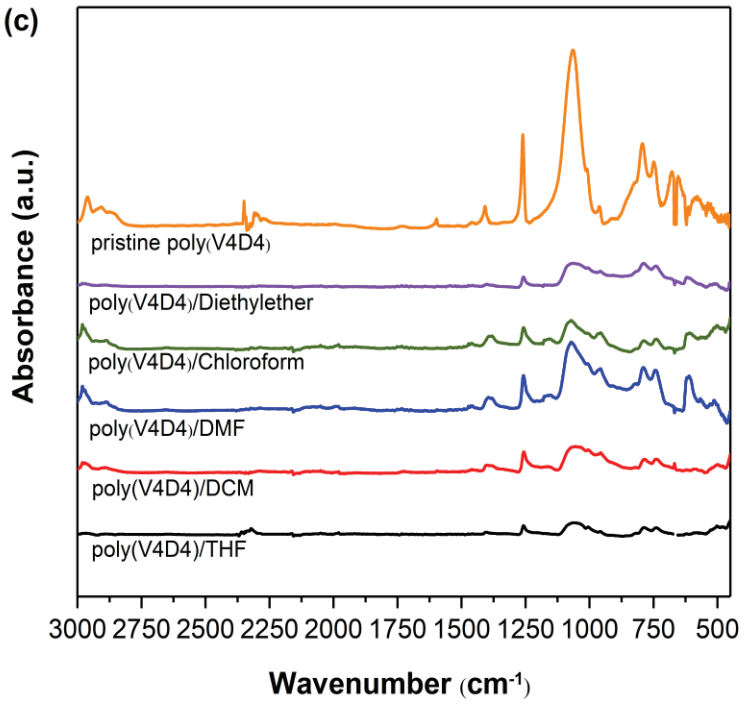

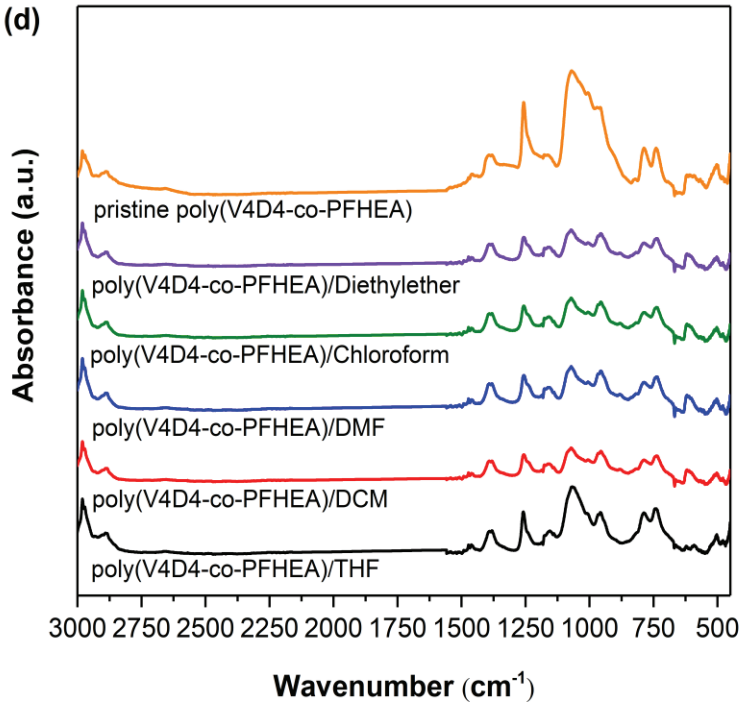

Figure 5.9. Cont.

(Cont. on next page)

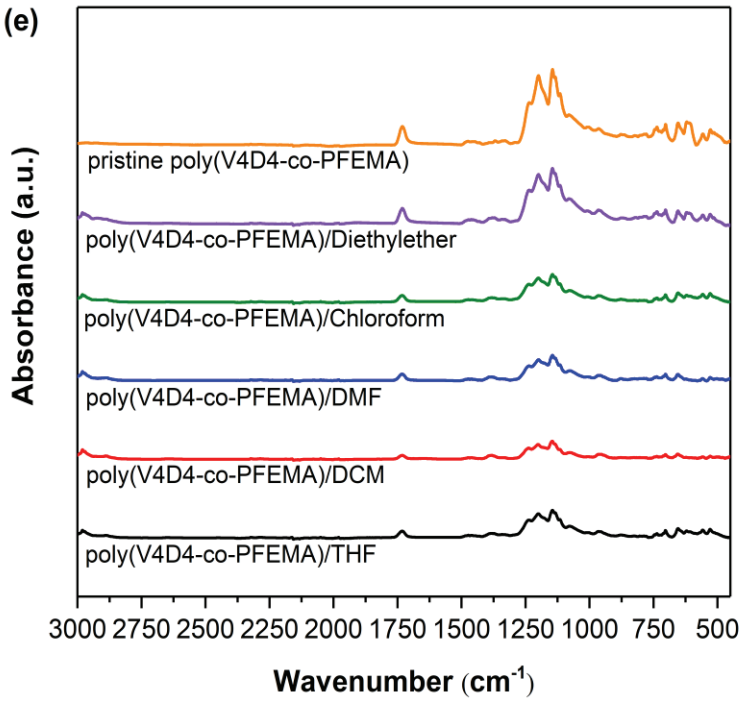

Figure 5.9. Cont.

In addition, SEM analysis before and after immersion in diethyl ether confirmed the durability of polymer coatings as there were no significant change in surface morphologies, as seen in Figure 5.10.

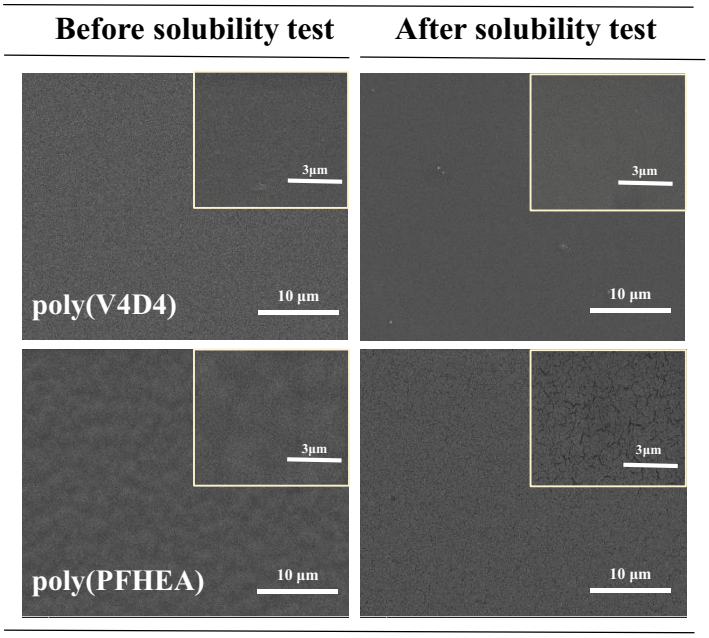

Figure 5.10. SEM images of iCVD polymers before and after solubility test.

(Cont. on next page)

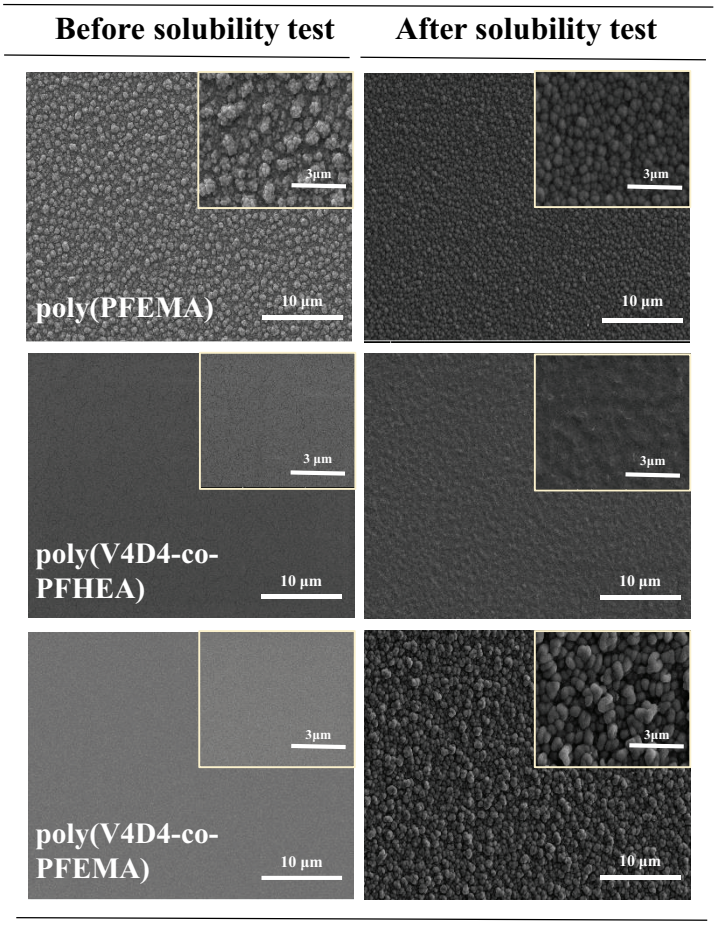

Figure 5.10. Cont.

5.3.5. Corrosion Tests

The corrosion protection performances of homo and copolymers on copper and zinc substrates were evaluated via Tafel polarization measurements as shown in Figure 5.11. The potentiodynamic polarization was measured after achieving constant OCP. Tafel curves were generated for poly(V4D4), poly(PFHEA), poly(PFEMA) homopolymers as well as poly(V4D4-co-PFHEA) and poly(V4D4-co-PFEMA) copolymers in 5 wt.% NaCl solution. The values of the anodic and cathodic Tafel slopes (β_A and β_C) provide valuable information on corrosion protection efficiency of the coatings; β_C is attributed to the hydrogen evolution in a cathodic branch, while β_A corresponds to the metal dissolution in an anodic branch (Ikhe et al., 2016).

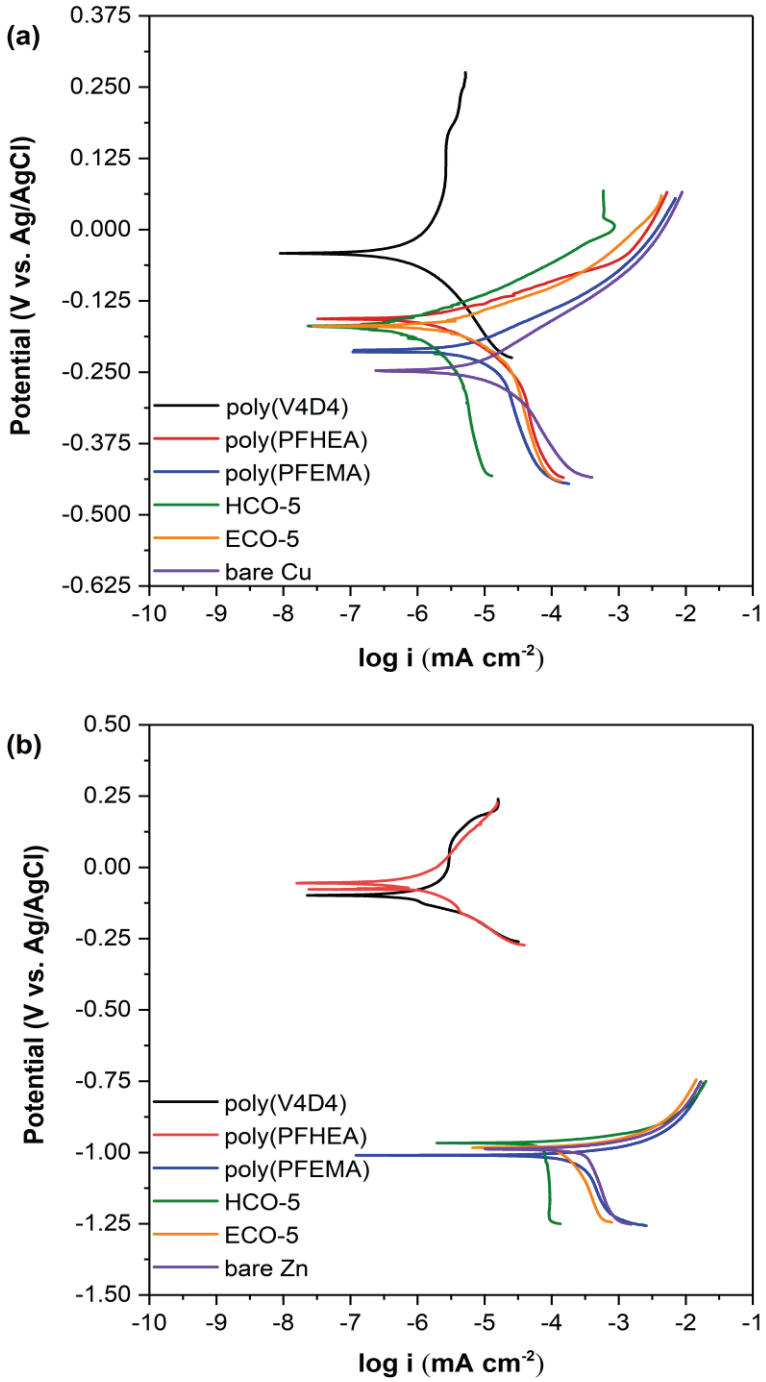

Figure 5.11. Potentiodynamic polarization measurements for iCVD coatings on (a) copper and (b) zinc substrates.

The effective anti-corrosion performance is attributed to minimizing the diffusion of the corrosive elements such as oxygen, water molecules and chloride ions towards the metal surface. The corrosion process is directly dependent on the wettability of the metal surface (Ishizaki et al., 2010; Zhu et al., 2014).

The important corrosion parameters, i.e. corrosion current density (I_{corr}), corrosion potential (E_{corr}), cathodic/anodic Tafel slopes (β_c/β_a) received from Tafel curves are listed

in Table 5.5. Experimental polarization resistance (R_p) was calculated by Stern-Geary equation (Emarati and Mozammel, 2020):

$$R_p = \frac{\beta_A \beta_C}{2.303 I_{corr}(\beta_A + \beta_C)} \tag{5.1}$$

where I_{corr} is the corrosion current in amps, β_A is the anodic beta Tafel coefficient for anodic portion in V dec^{-1}, β_C is the cathodic beta Tafel coefficient for anodic portion in V dec^{-1}.

Corrosion potential and corrosion current density are two indicative parameters for corrosion reaction. The lower corrosion current density and higher corrosion potential signify a lower corrosion rate which means better corrosion protection behavior (Chen et al., 2019; Rajitha and Mohana, 2020). Unlike wet processes like spin coating and dip coating, most iCVD deposited polymers exhibit very small or no porosity due to lack of solvent in polymerization environment. Since polymerization reactions occur on cooled substrate surface, and not in gas phase iCVD coatings can conform to the overall geometry making them highly suitable to use as anti-corrosion coatings. Still, the porosity of iCVD coatings on metal surfaces was calculated from potentiodynamic polarization measurements, using Equation 5.2 (Pawar et al., 2007):

$$Porosity = \frac{R_{p_{bare}}}{R_{p_{coated}}} \times 10^{-(\frac{|\Delta E_{corr}|}{\beta_a})} \tag{5.2}$$

where R_{pbare} is the polarization resistance of bare metal, $R_{pcoated}$ is the polarization resistance of coated metal, ΔE_{corr} is the difference between corrosion potentials, and β_a is the anodic Tafel slope for bare metal. The protection efficiency (η %) of the coatings were calculated from I_{corr} values of the samples, using the expression (Zhu et al., 2014):

$$\eta(\%) = \frac{I_{corr_{bare}} - I_{corr_{coated}}}{I_{corr_{bare}}} \times 100 \tag{5.3}$$

The results suggest that siloxane films significantly increase E_{corr} and provide better corrosion protection for metal surfaces. Copolymerization of V4D4 with fluorinated monomers results in lower E_{corr} compared to poly(V4D4) homopolymer;

however, chemical and mechanical stability in strong organic solvents is greatly improved. For copper substrates, poly(V4D4-co-PFHEA) coatings showed the highest protection efficiency (91%) and the lowest corrosion rate (0.018 mpy). All homopolymers exhibited lower corrosion rates and higher protection efficiencies than poly(V4D4-co-PFEMA) copolymer. On zinc substrates, poly(V4D4) and poly(PFHEA) homopolymers followed by poly(V4D4-co-PFHEA) copolymer showed lower corrosion rates and higher protection efficiencies.

Table 5.5. Kinetic parameters of iCVD polymers on copper and zinc substrates

	E_{corr}, mV	I_{corr}, μA	β_A, mV/dec	β_C, mV/dec	Corrosion rate, mpy	$R_p x10^{-3}$, kΩ/cm^2	Porosity, %	η, %
Copper								
Bare	-247	18.9	106	159	0.182	1.46		
poly(V4D4)	-42	4.2	1922	213	0.046	19.82	6.33	77.78
poly(PFHEA)	-156	7.8	68	201	0.086	2.83	3.73	58.73
poly(PFEMA)	-213	14.4	87	248	0.158	1.94	1.57	23.81
poly(V4D4-co-PFHEA)	-169	1.7	59	249	0.018	12.18	0.65	91.01
poly(V4D4-co-PFEMA)	-169	12	77	245	0.132	0.25	3.75	36.51
Zinc								
Bare	-988	939	152	10^{15}	9	8.79		
poly(V4D4)	-98	2	531	137	0.024	20.54	1.81	99.79
poly(PFHEA)	-60	0.1	136	92	0.002	100.08	0.85	99.99
poly(PFEMA)	-910	874	156	10^{15}	8.05	9.05	$4.46x10^{-6}$	6.92
poly(V4D4-co-PFHEA)	-967	140	87	10^{15}	1	5.69	$2.92x10^{-8}$	85.09
poly(V4D4-co-PFEMA)	-983	550	139	10^{15}	6	1.45	$1.62x10^{-7}$	41.43

dec: decade
mpy: mils per years

EIS analysis is a powerful tool that provides valuable information about corrosion protection performance, robustness of coatings, and electrochemical activity at coating/metal interface. EIS analysis was performed for bare metals and polymer-coated metals from 100 mHz to 10 kHz in 5 wt.% NaCl solution. Measurements were performed after 30 min of immersion for stabilization. Nyquist plots of bare metals and polymer-coated metals (copper and zinc) are presented in Figure 5.12 with insets showing enlarged Nyquist plots. The impedance plots of the copolymer coatings showed that there are two different capacitive loops as shown in Figure 5.12. The first loop refers to the polymer coating itself, while the second one is attributed to the dissolution process taking place at the coating-metal interface (Sadagopan et al., 2005). The Nyquist semi-circles with wider diameters indicate better corrosion resistance (Rajitha and Mohana, 2020). As shown in Figure 5.12, homopolymers of poly(V4D4) and poly(PFHEA) and their copolymer poly(V4D4-co-PFHEA) coating exhibit better anti-corrosion and barrier performance than poly(PFEMA) homopolymer and poly(V4D4-co-PFEMA) copolymer coatings with

lower corrosion impedance. The variations between poly(V4D4-co-PFHEA) and poly(V4D4-co-PFEMA) copolymer performance might be due to differences in crosslinked network due to acrylate and methacrylate groups linked to V4D4 (Sakai et al., 2012).

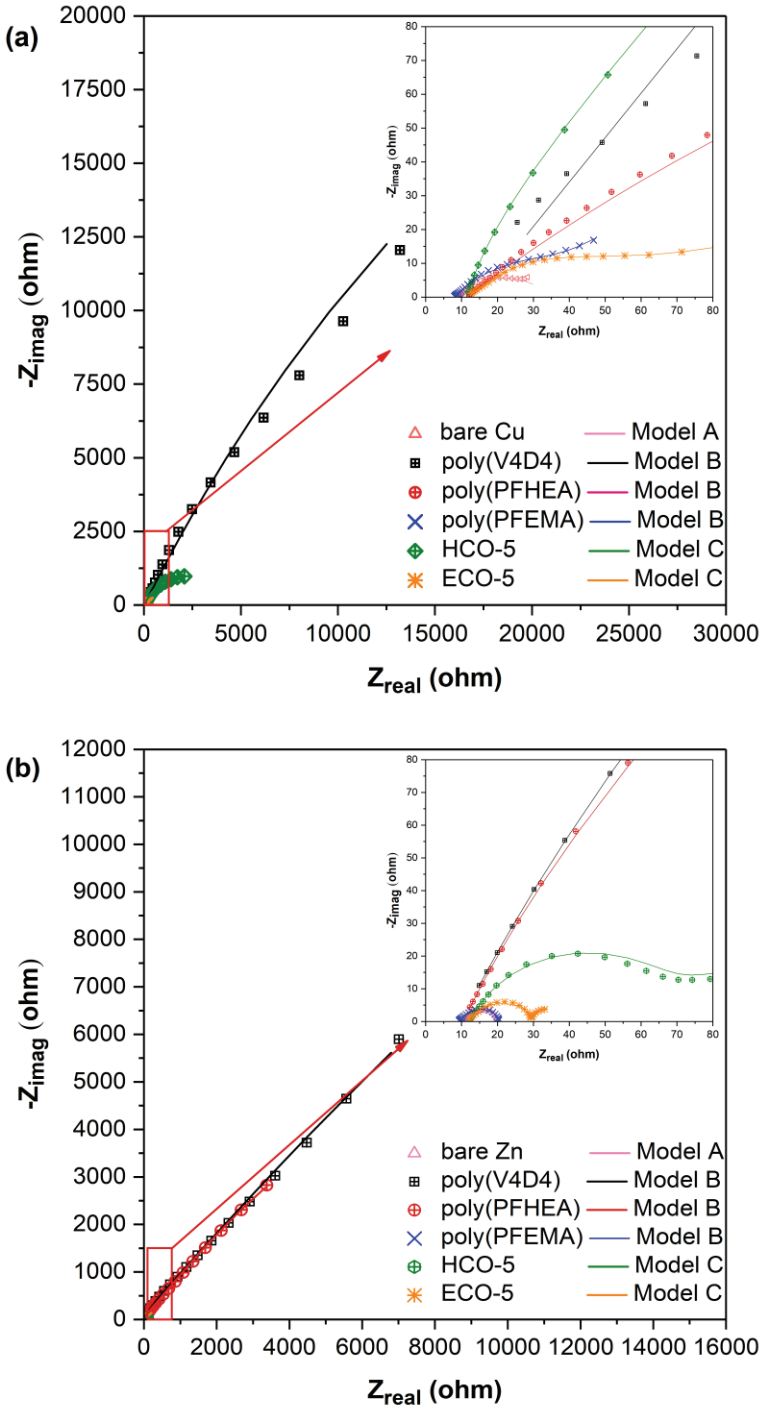

Figure 5.12. Nyquist plots of iCVD polymers on (a) copper and (b) zinc substrates.

Bode plots of samples from the same experiment are shown in Figure 5.13. Bode plots reveal the circuit behavior in terms of circuit elements either as resistor (Θ = 0 degrees) or capacitor (Θ = -90 degrees), and provide valuable information about electrochemical activity at the coating–metal interface and the extent of water diffusion or penetration (Caldona et al., 2020; Kunst et al., 2014). The shift in time constant through high frequency to medium/low frequency indicates the presence of a passivation layer on the top of metal surface (Hsu and Mansfeld, 2001). The medium to low frequency phenomenon is associated with the acceleration of interaction between coating and metal surface (Jüttner, 1990). Figure 5.13 shows circuit behavior representative of a capacitor at frequencies above 100 Hz and of a resistor at frequencies below 1 Hz with the exception of poly(V4D4) and poly(PFHEA) homopolymer. From Figures 5.13 (a) and (c), bare metal and homopolymer coated samples have only one peak at low frequency region while poly(V4D4-co-PFHEA) and poly(V4D4-co-PFEMA) coated samples showed two-time constants. The phase angle of poly(V4D4-co-PFHEA) coating on copper surface shows well-defined time constants in high frequency range indicating a better corrosion barrier. However, on zinc surface the lack of high frequency time constants imply poor or defective copolymer coatings. This observation is also in agreement with calculated protection efficiencies listed in Table 5.5 where poly(V4D4) and poly(PFHEA) homopolymers exhibited better protection efficiency compared to copolymer coatings, especially on zinc. Figure 5.13 (b) and (d) show parallel resistor-capacitor behavior of polymer coatings by illustrating the effect of measurement frequency on current flow. The current passes through the circuit capacitors at high frequencies and passes through the circuit resistors as lower frequencies (Loveday et al., 2004a; Loveday et al., 2004b; Loveday et al., 2005). The lower breakpoint frequency can correspond to reduction of corrosion delamination (Caldona et al., 2020). The shift in the breakpoint frequency through high frequencies might indicate electrolyte diffusion through the coating. As the frequency decreases, the trend lines diverge, and the dissimilar resistance values of polymer coatings become apparent. A coating experiencing corrosion at the substrate requires a second parallel resistor-capacitor in series with the coating resistor as observed for both copolymer coating on zinc, as seen in Figure 5.13 (d) (Loveday et al., 2004a; Loveday et al., 2004b; Loveday et al., 2005).

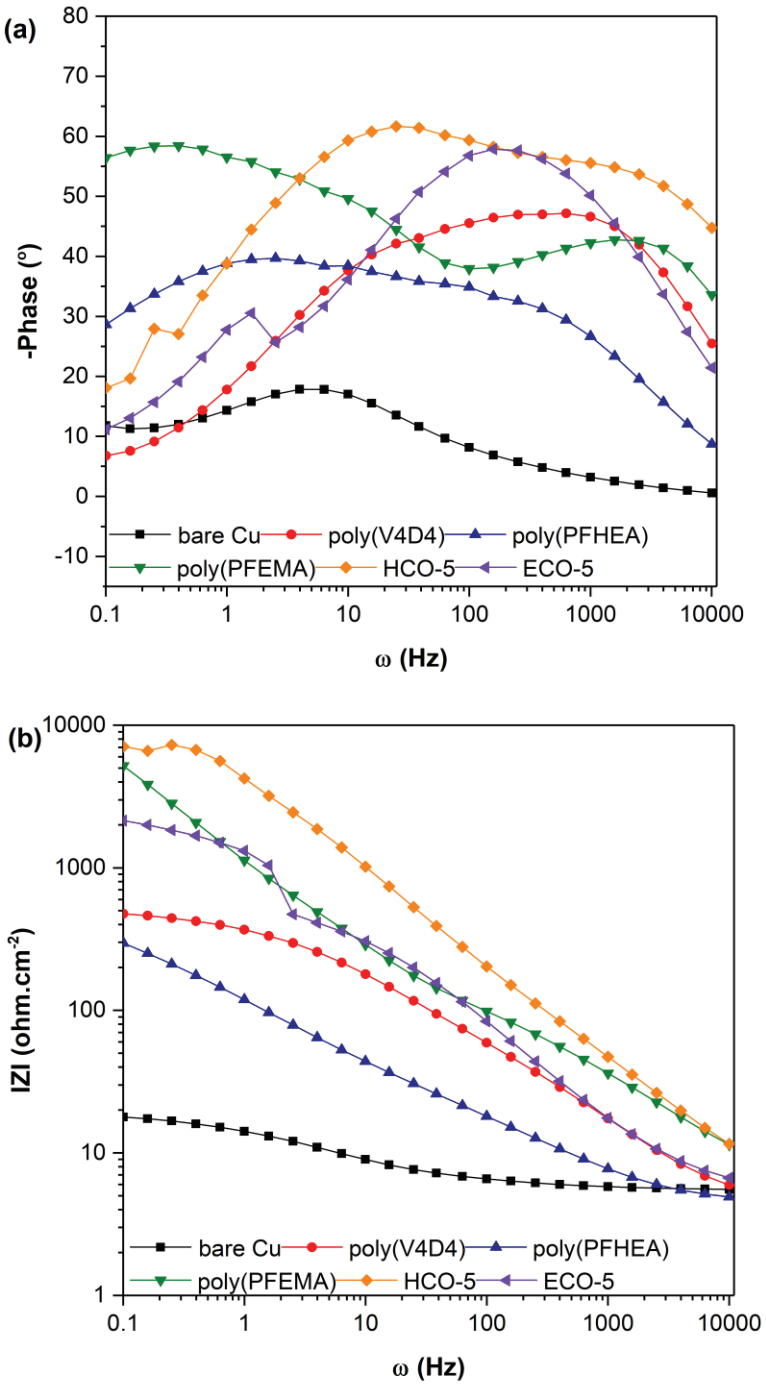

Figure 5.13. Bode plots of iCVD polymers on (a), (b) copper and (c), (d) zinc substrates

(Cont. on next page)

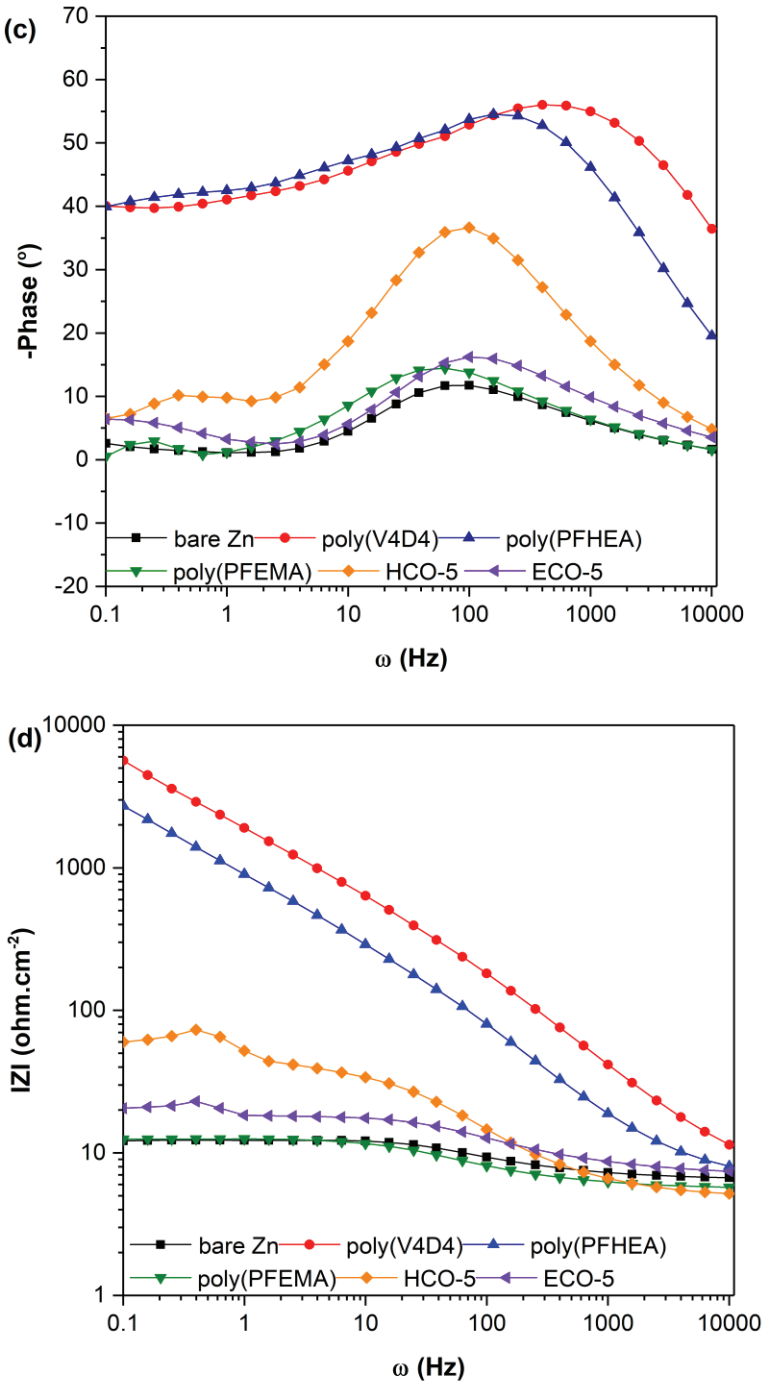

Figure 5.13. Cont.

Figure 5.14 shows three proposed EEC models based on Bode plot analysis to fit impedance parameters including solution resistance (R_s), resistance of the coating (R_c) which is the function of pore dimensions, constant phase element of the coating (CPE_c) characterized by the coating thickness and dielectric constant, charge transfer resistance at polymer/metal interface (R_{ct}) and constant phase element of electrical double layer (CPE_{dl}). The constant phase element (CPE) is commonly used in electric equivalent

circuit to decrease the systematical error and represents deviation from true capacitance behavior which depends on a few parameters such as coating thickness and defect structure (Ishizaki et al., 2010). The impedance of CPE is expressed as $Z_{CPE} = Y_o^{-1}(j\omega)^{-n}$, where Y_o represents the pseudo-capacitance (j^2=-1), ω is the angular frequency (ω=2πf) and n indicates the exponential coefficient ranging from 0 to 1 (Caldona et al., 2020). The impedance parameters of bare metals and polymer-coated metals were modeled by the electric equivalent circuit using Gamry Echem Analyst™ software. Table 5.6 lists model parameters of the best fit to the experimental data using EEC models shown in Figure 5.14. Randles model (Model A) is one of the simplest and commonly used models describing electrochemical processes at bare metal/medium interface using solution resistance in connection with charge transfer resistance and constant phase element of electrical double layer. Model B describes corrosion process of metal surface with a polymer coating exposed to corrosive medium using solution resistance, resistance of polymer coating and constant phase element of the coating. The fit parameters, CPE_c and R_c, of Model B are used as invariable constants for the non-perfect coatings which are considered as typical for undamaged coating. Model C expands Model B with addition of charge transfer resistance at polymer/metal interface and constant phase element of electrical double layer. The higher values of R_c and R_{ct} and the lower values of CPE_c and CPE_{dl} indicate the better corrosion performance of the coating (Pawar et al., 2007).

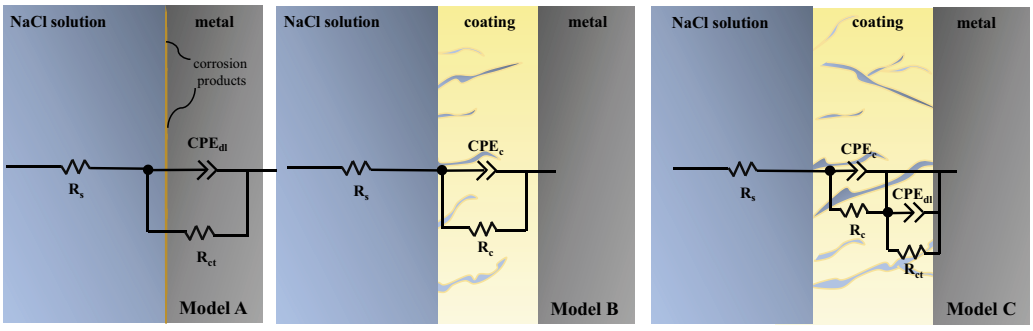

Figue 5.14. Equivalent electric circuits (EEC) used for fitting EIS data of bare and iCVD coated metals

The values of electrochemical parameters from EEC fitting are in accordance with low Chi-Square (χ^2) values which are similar to reported values in literature (Jüttner, 1990; Sakai et al., 2012). Chi-Square value (χ^2) calculated between measured and model impedances should be greater than or equal to zero (Pan et al., 1996; Feliu, 2020);

therefore, only the best fitting models are shown in Table 5.6 and Table 5.7. As shown in Table 5.6, poly(V4D4) homopolymer coating shows at least two orders of magnitude higher coating resistance than fluorinated homopolymers on copper. On zinc metal poly(V4D4) and poly(PFHEA) homopolymers exhibited three orders of magnitude higher coating resistance than poly(PFEMA). In addition, poly(V4D4) and poly(PFHEA) homopolymers exhibited lower CPE_c than poly(PFEMA). The experimental data are also in good agreement with the lower values of corrosion current density (I_{corr}) or higher values of corrosion potential (E_{corr}) as shown in Table 5.6 (Cao et al., 2018). For uncoated copper and zinc, R_s values describing the diffusion of ions into the solution from the oxidation of metals were determined to be 8.9 Ω and 10.9 Ω, respectively (Caldona et al., 2020; Liu et al., 2007). For all iCVD coatings with the exception of poly(PFEMA) homopolymer, higher R_s values were obtained. R_{ct} and CPE_{dl} parameters in Model C represents electrochemical reactions at the coating and metal interface. R_{ct} values of poly(V4D4-co-PFHEA) coatings ($3.6x10^3$ Ω and 33.9 Ω for copper and zinc, respectively) suggest that these coatings effectively decrease electron-transfer activity at the coating-metal interface. A lower CPE_{dl} indicates that electrical charge distribution is minimal and the presence of corrosion products are reduced significantly (Caldona et al., 2020). Additionally, R_c values of poly(V4D4-co-PFHEA) coatings are higher than poly(V4D4-co-PFEMA) on both copper and zinc metals.

Table 5.6. Electrochemical parameters extracted from the fit to the equivalent circuit models for EIS data in 5 wt.% NaCl solution

	Uncoated	poly(V4D4)	poly(PFHEA)	poly(PFEMA)	poly(V4D4-co-PFHEA)	poly(V4D4-co-PFEMA)
Copper						
Model	**Model A**	**Model B**	**Model B**	**Model B**	**Model C**	**Model C**
R_s (Ω)	8.9	14.1	11.1	7.6	11.9	11.6
CPE_c (F m^{-1})		0.32	0.55	15.8	0.03	$4.5x10^{-7}$
n_1		0.58	0.42	0.47	0.84	0.46
R_c (Ω)		$95.9x10^3$	665.5	70.9	110.3	70.5
CPE_{dl} (F m^{-1})	7.99				0.38	13.46
n_2	0.52				0.56	1
R_{ct} (Ω)	26.13				$3.6x10^3$	36.7
χ^2	0.0066	0.0065	0.0015	0.0089	0.0024	0.0069
Zinc						
Model	**Model A**	**Model B**	**Model B**	**Model B**	**Model C**	**Model C**
R_s (Ω)	10.9	12.9	12.3	9.3	12.3	11.9
CPE_c (F m^{-1})		0.17	0.37	0.42	$1.1x10^{-4}$	0.14
n_1		0.58	0.59	0.71	0.73	0.69
R_c (Ω)		$17.4x10^3$	$8.8x10^3$	11.4	63.4	18.5
CPE_{dl} (F m^{-1})	0.29				19.9	297.54
n_2	0.73				0.77	0.95
R_{ct} (Ω)	9.3				33.9	8.1
χ^2	0.0041	0.0014	0.0011	0.0029	0.0048	0.0029

Table 5.7. Electrochemical parameters extracted from the fit to the equivalent circuit models for the EIS data in 5 wt.% NaCl solution

	Uncoated			poly(V4D4)			poly(PFHEA)		
Copper									
Model	**Model A**	**Model B**	**Model C**	**Model A**	**Model B**	**Model C**	**Model A**	**Model B**	**Model C**
R_s, Ω	8.9	8.8	8.9	14.2	14.1	11.8	10.8	11.1	11.5
CPE_c, F		8.041	319.89		0.32	0.0013		0.55	0.13
n_1		0.52	0.56		0.587	0.74		0.43	0.47
R_c, Ω		26.13	23.72		95.9×10^3	138.3		665.5	254.2
CPE_{dl}, F			478	0.32		0.103	0.51		15.44
n_2	0.52		1	0.59		0.613	0.42		1
R_{ct}, Ω	26.13		3.74×10^3	9.7×10^4		4.85×10^4	663.2		3.91×10^3
χ^2	0.0066	0.0069	0.0071	0.0068	0.0065	0.0066	0.0017	0.0015	0.0016
Zinc									
Model	**Model A**	**Model B**	**Model C**	**Model A**	**Model B**	**Model C**	**Model A**	**Model B**	**Model C**
R_s, Ω	10.9	10.8	10.9	2.3	2.9	9.8	6.7	6.8	10.5
CPE_c, F		0.28	0.28		0.17	8.1×10^{-3}		0.37	0.024
n_1		0.74	0.74		0.58	0.73		0.59	0.74
R_c, Ω		9.31	9.28		17.4×10^3	767.2		8.8×10^3	496.8
CPE_{dl}, F	0.29		2268	0.17		6.46	0.37		1.5×10^{-3}
n_2	0.74		1	0.58		0.441	0.58		0.48
R_{ct}, Ω	9.3		309.2	1.75×10^4		1.5×10^5	8.73×10^3		31.51
χ^2	0.0041	0.0042	0.0046	0.0015	0.0014	0.0015	0.0013	0.0011	0.0012

(Cont. on next page)

Table 5.7. Cont.

	poly(PFEMA)			poly(V4D4-co-PFHEA)			poly(V4D4-co-PFEMA)		
Copper									
Model	**Model A**	**Model B**	**Model C**	**Model A**	**Model B**	**Model C**	**Model A**	**Model B**	**Model C**
R_s, Ω	7.6	7.6	7.9	6.4	6.11	11.9	10.7	10.8	11.6
CPE_c, F		15.8	6.09		0.31	0.03		6.75	4.5×10^{-7}
n_1		0.47	0.53		0.65	0.84		0.37	0.46
R_c, Ω		70.9	47.48		3.14×10^3	110.3		$1.32E \times 10^2$	70.5
CPE_{dl}, F	15.92		201.56	0.31		0.38	7.08		13.46
n_2	0.47		0.73	0.66		0.56	0.39		1
R_{ct}, Ω	71.2		89.44	2.97×10^3		3.6×10^3	1.33×10^2		36.7
χ^2	00097	0.0089	0.0121	0.0055	0.0046	0.0024	0.0076	0.0076	0.0069
Zinc									
Model	**Model A**	**Model B**	**Model C**	**Model A**	**Model B**	**Model C**	**Model A**	**Model B**	**Model C**
R_s, Ω	9.3	9.3	9.2	7.7	7.6	8.2	8.6	8.4	11.9
CPE_c, F	0.42	0.42	0.15	1.6×10^{-4}		1.1×10^{-4}		0.56	0.14
n_1	0.71	0.71	0.79	0.64	0.64	0.73		0.62	0.69
R_c, Ω	11.3	11.4	3.87	80.4	80.7	63.4		341.3	18.5
CPE_{dl}, F			0.49			19.9	0.56		297.54
n_2			0.82			0.77	0.61		0.95
R_{ct}, Ω			7.41			33.9	340.3		8.1
χ^2	0.0031	0.0029	0.003	0.0051	0.005	0.0048	0.0036	0.0035	0.0029

As shown in Figure 5.15 pictures of the samples taken before and after the test also support potentiodynamic polarization measurement and EIS analysis findings as poly(V4D4), poly(PFHEA) and their copolymers (HCO-5) films seems to perform better than poly(PFEMA). The hydrophobic polymer layer inhibits the adsorption of chloride ions on the metal surface which leads to the transformation of $M(OH)_2$ (M: metal) to soluble MCl_2 destroying metal surface (Ikhe et al., 2016). The results suggest that HCO-5 coatings can act as effective barriers to Cl^- ions reaching surface.

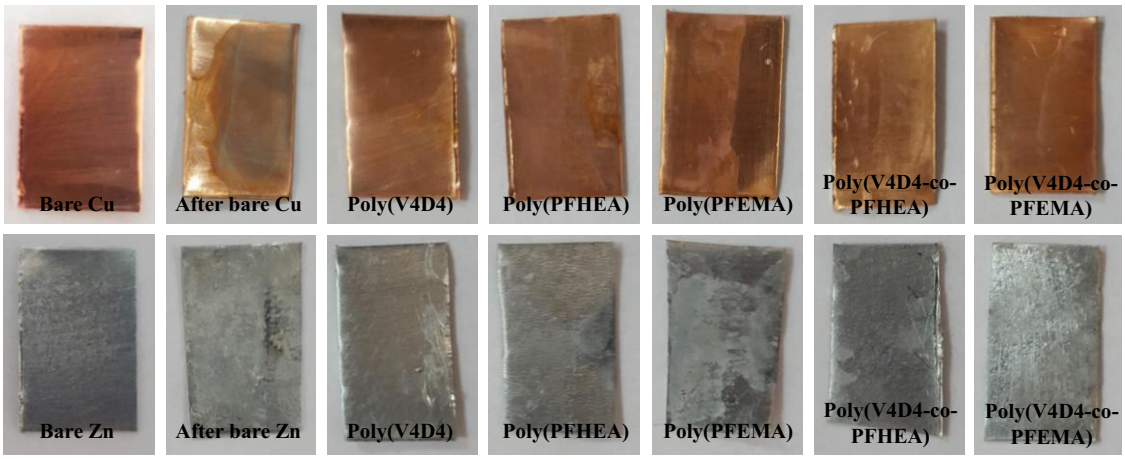

Figure 5.15. Pictures of bare and iCVD coated (a) copper and (b) zinc samples after corrosion test.

Long term durability and corrosion tests of copolymer coatings were performed by immersing poly(V4D4-co-PFHEA) coated Cu and Zn plates in 5 wt.% NaCl solution at room temperature for 30 days. Samples were cleaned by following the procedure described in ISO 8407 standard to remove the corrosion products (ISO 8404:2009, 2009). Figure 5.16 shows the surface of uncoated and poly(V4D4-co-PFHEA) coated copper and zinc metals immersed in 5 wt.% NaCl solution for 15 and 30 days. The corrosion products increased with increasing immersion time and continuously precipitated on the surface. Uncoated copper and zinc show severe corrosion after 30 days. Although copolymer films deposited on samples were very thin (~250 nm), the difference between coated and uncoated samples were clear on macroscopic scale.

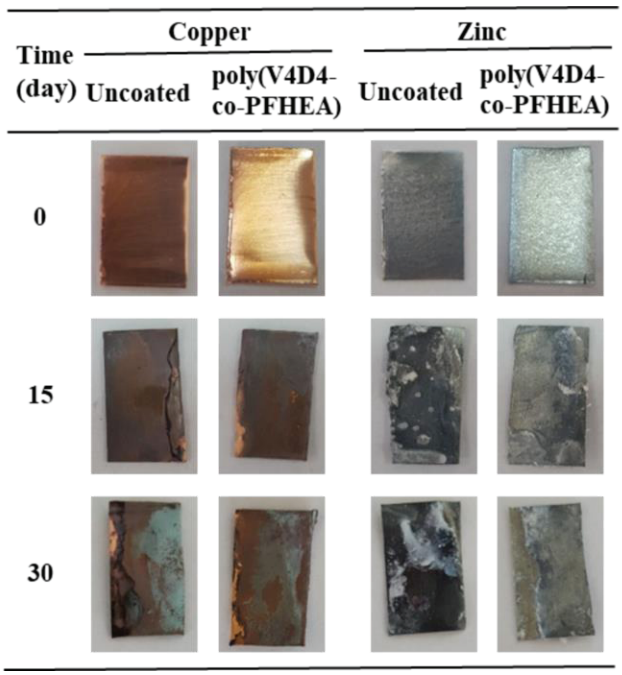

Figure 5.16. Coated and uncoated Cu and Zn metals after immersion in 5 wt.% NaCl solution.

In addition to visual inspection of the metal surfaces, detailed SEM analysis was also carried out to evaluate performance of iCVD coatings against corrosion. Figure 5.17 shows the surface morphology evolution of bare and coated metal samples exposed to 5 wt.% NaCl solution after 15 and 30 days with insets showing higher magnification. The scratches on the surface of uncoated metals are due to initial rough surface cleaning using emery papers. Also, there are a few fissures and pits visible at high magnification. There is almost no difference in the surface morphology of poly(V4D4-co-PFHEA) coated metals compared with bare metals before the corrosion test. The pitting and small pores that are uniformly distributed on the entire surface were observed after 15 days and became more pronounced after 30 days on uncoated copper. First indication of corrosion was observed on poly(V4D4-co-PFHEA) coated copper with a small number of localized pits after 15 days. Corrosion seemed to be progressing at a much slower rate compared to uncoated sample after 30 days. During corrosion process the electrolyte is adsorbed by the coating on copper surface (Ikhe et al., 2016). The electrolyte carries water with dissolved O_2 and Cl^- and brings them in contact with bare copper surface resulting in loss of corrosion protection (Pawar et al., 2007; Cakmakcı et al., 2013). The coating on copper surface could not provide complete corrosion protection after 30 days due to formation of copper oxides and/or chloride. The platelet-shaped microcrystals appeared on bare Zn surface after 15 days of immersion and covered the entire surface in 30 days. However,

poly(V4D4-co-PFHEA) coated Zn showed very few of these features in 30 days. After that submicron scale corrosion products started to appear and cover the surface. The extending exposure time to solution can result in inhibition of oxygen reduction and reduce the dissolution of zinc due to formation of passive layer as a corrosion product as reported in literature (Cakmakcı et al., 2013; Redondo et al., 2009; Meng et al., 2019; Pawar et al., 2007).

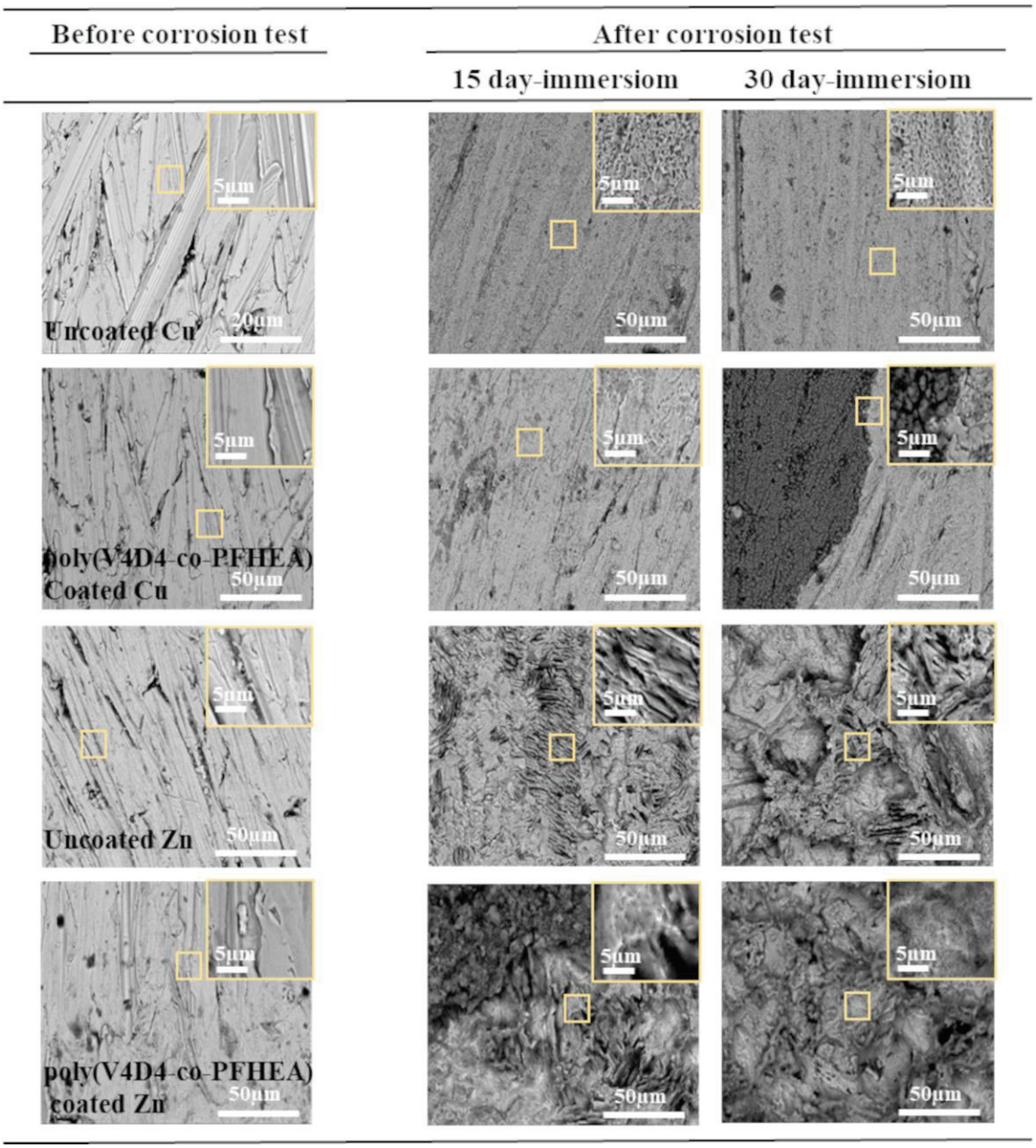

Figure 5.17. SEM images of uncoated and HCO-5 coated metals immersed in 5 wt.% NaCl solution for 15 days and 30 days.

As listed in Table 5.8, measured weight losses of samples after 15 and 30 days were consistent with the potentiodynamic polarization, impedance analysis results and SEM analysis. The measured weight loss is in accordance with the release rate of M^{+2} (M: metal) on the surface of metal which leads to surface damage (Ikhe et al., 2016). Poly(V4D4-co-PFHEA) coating provided a certain degree of corrosion protection as evidenced by approximately 50% less weight loss compared to uncoated samples. Surface hydrophobicity due to the presence of $–CF_3$ groups and a crosslinked structure of polymer coating seems to have decreased the formation of the corrosion products.

Table 5.8. Weight losses of uncoated and coated samples after 15-day and 30-day immersion in 5 wt.% NaCl

Time Day	**Weight loss, mg cm^{-2}**			
	Cu		**Zn**	
	Uncoated	**poly(V4D4-co-PFHEA)**	**uncoated**	**poly(V4D4-co-PFHEA)**
15	31.86	13.19	14.15	9.32
30	43.23	18.52	20.59	11.39

5.3.6. Mechanical Stability of Polymer Coatings

In addition to metals or other opaque substrates, protective coatings are also applied to optically transparent materials such as electronic and photonic devices and their components where optical transparency of the protective coating is important. It has been shown that epoxy based iCVD copolymers exhibit excellent optical transparency in visible spectrum, good adhesion to optical glass and good mechanical strength (Ozpirin and Ebil, 2018). Adhesion tests were performed for poly(V4D4), poly(PFHEA), poly(PFEMA) homopolymers and their copolymers on c-Si and metal substrates to evaluate how well iCVD polymers adhere to substrates. The optical microscope images of coatings before and after adhesion test are shown in Figure 5.18. Hydrophobic materials are known to have a poor adhesion to most substrates, but they can exhibit good corrosion resistance (Grignard et al., 2011; Zhu et al., 2020). Very small pieces of fluorinated homopolymer coating (poly(PFHEA) and poly(PFEMA)) were removed by cellophane tape from the surface after the adhesion test. No other defects or delamination was observed under with optical microscope analysis of the surface after the test. The area removed during the test was less than 0.5% which still within acceptable range. Poly(V4D4) homopolymer showed excellent adhesion to the surface; no defect or

delamination was observed. Similarly, poly(V4D4-co-PFHEA) and poly(V4D4-co-PFEMA) copolymers also showed excellent adhesion to substrates with no visible defects or delamination.

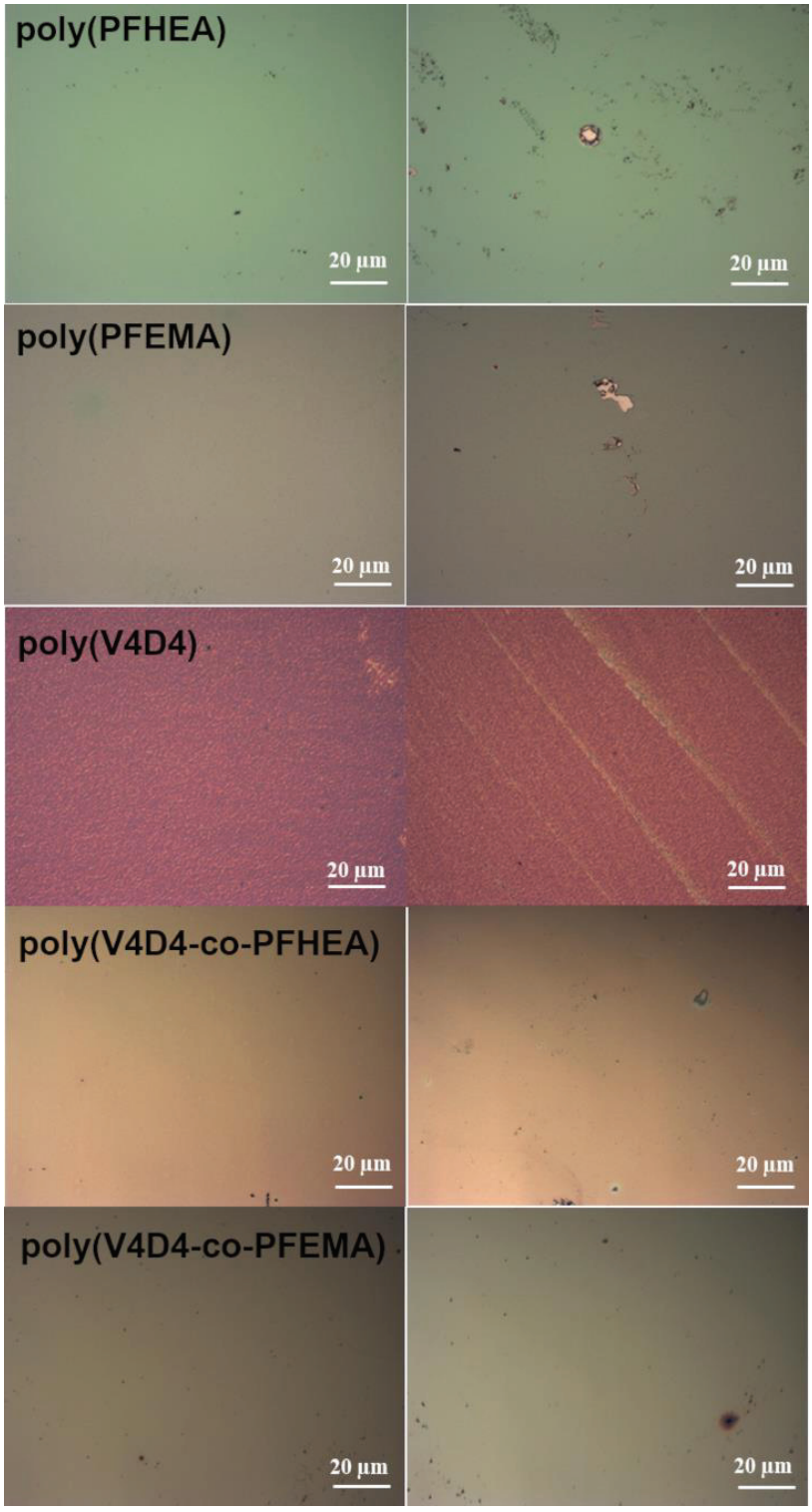

Figure 5.18. Optical microscopy images of polymer films before and after adhesion test.

5.4. Conclusion

Poly(V4D4), poly(PFHEA), poly(PFEMA) homopolymer, poly(V4D4-co-PFHEA) and poly(V4D4-co-PFEMA) copolymer coatings were synthesized on a variety of substrates via iCVD process. The chemical stability and durability of these polymer coatings were evaluated by adhesion to substrate tests and immersion in strong organic solvents. In addition, the corrosion protection aspects of coatings on copper and zinc substrates in 5 wt.% NaCl solution were investigated by potentiodynamic polarization measurements and EIS analysis.

It was found that hydrophobic poly(PFHEA) and poly(PFEMA) homopolymers can withstand strong organic solvents well with the exception of THF and diethyl ether; however, ultrasonic treatment can remove these homopolymers from substrate surface completely. Copolymerization of PFHEA and PFEMA monomers with V4D4 was found to increase both chemical durability and improve mechanical strength of coatings since vinyl groups of V4D4 were able to bind covalently with PFHEA or PFEMA. Copolymerization also increased surface adhesion of the films. In literature, corrosion rates for polymer coatings on copper and zinc substrates in 3.5 wt.% NaCl solution were reported as 0.035-0.098 mpy and 0.063 mpy, respectively (Cao et al., 2018; Pawar et al., 2007; Meng et al., 2019). iCVD synthesised polymer coatings exhibited much lower corrosion rates, as low as 0.002 mpy, in 5 wt.% NaCl. Although, the increase in the concentration of NaCl accelerates pitting corrosion, iCVD copolymer coatings in a higher concentration of NaCl solution still exhibit higher anti-corrosion resistance than those reported in the literature (Meng et al., 2019; Han et al., 2016). Between fluorinated homopolymers, poly(PFHEA) performed better than poly(PFEMA). EIS analysis also confirmed that poly(V4D4), poly(PFHEA) and poly(V4D4-co-PFHEA) copolymer films exhibit better resistance to corrosion in 5 wt.% NaCl solution. The potentiodynamic polarization measurements reveal that copolymerization of fluorinated monomers with V4D4 resulted in coatings with higher protection efficiency; 91% for poly(V4D4-co-PFHEA) and 36% for poly(V4D4-co-PFEMA), compared to homopolymer coatings; 59% for poly(PFHEA) and 24% for poly(PFEMA). Poly(V4D4-co-PFHEA) copolymer coatings showed the best anti-corrosion performance with weight loss reduction by 57% and 45% for copper and zinc, respectively, and the corrosion rates by nearly a factor of 10.

The results of potentiodynamic polarization measurements and EIS analysis, together with corrosion and durability indicate that poly(V4D4-co-PFHEA) copolymer coating (with 1:1 ratio of V4D4: PFHEA ratio) shows low porosity, highly hydrophobic surface, excellent adhesion, good solvent resistance and offers an effective physical and chemical protection without the need for surface pretreatment. Combining well-balanced properties of siloxane and fluorinated polymer chemistries, iCVD process is an excellent low-cost method for fabrication of conformal protective coatings on opaque and transparent materials with different geometries.

CHAPTER 6

CONCLUSION

This thesis is aimed to evaluate the feasibility of highly cross-linked, hydrophobic, and excellent oxygen selective thin homopolymers of 2,4,6,8-tetramethyl-2,4,6,8-tetra vinylcyclotetrasiloxane (V4D4), 2-(perfluorohexyl-ethyl acrylate) (PFHEA) and 2-(perfluoroalkyl-ethyl methacrylate) (PFEMA) and their copolymers films as potential candidates for GDLs materials in GDEs and as barrier layers fır corrosion protection of metals via the iCVD process. The electrochemical performance, physical and chemical properties of the fabricated homopolymers and copolymers on a variety of substrates are summarized as follows:

As reported in Chapter 4, hydrophobic and highly oxygen permeable polymer thin films were fabricated as GDLs in GDEs for aqueous metal-air batteries. Thin-film GDLs exhibited an average water vapor transmission rate of 7.5 g m^{-2} day^{-1} and enhanced oxygen diffusion with oxygen permeabilities as high as 3.53 x 10^{-15} mol m m^{-2} s^{-1} Pa^{-1} (10.5 Barrer). Water tranmission rate values for poly(V4D4-co-PFHEA) and poly(V4D4-co-PFEMA) copolymers varied between 5.48 g m^{-2} day^{-1} and 11.32 g m^{-2} day^{-1}; between 2 and 150 times lower than commercial GDLs (Crowther and Salomon, 2012). Fabricated GDEs exhibited higher oxygen reduction current densities (228.2 mA cm^{-2}) compared to commercial ones (132.7 mA cm^{-2}). Copolymer GLDs exhibited an order of magnitude higher oxygen diffusion (39.5 x 10^{-8} cm^2 s^{-1}) in GDEs compared to commercial counterparts (1.84 x 10^{-8} cm^2 s^{-1}). Due to the high oxygen solubility of V4D4 and excellent hydrophobic behavior of PFHEA and PFEMA, their copolymers can effectively promote the diffusion of oxygen and restrict moisture intake making them ideal materials for GDLs.

In Chapter 5, the corrosion resistance of the same iCVD polymers, chemical durability in various organic solvents and adhesion to the substrate were investigated. It was shown that iCVD polymers exhibited excellent adhesion to substrates. The corrosion rates as low as 0.002 mpy on zinc substrates was reached with 250-nm-thick iCVD-synthesized polymers which is lower than previously reported polymer coatings and more

than three orders of magnitude lower than bare zinc. Poly(V4D4) and poly(PFHEA) homopolymers show extremely high protection efficiencies (~ 99%) on zinc, while poly(V4D4-co-PFHEA) copolymer with slightly lower corrosion efficiency (85–91%) provides a better anticorrosion barrier with weight loss reduction by 57 and 45% for copper and zinc, respectively, and with improved chemical and mechanical properties.

In conclusion, all thin-films of 2,4,6,8-tetramethyl-2,4,6,8-tetravinyl cyclotetrasiloxane (V4D4), 2-(perfluorohexylethylacrylate) (PFHEA) and 2-(perfluoro alkylethylmethacrylate) (PFEMA) deposited via iCVD in this thesis can be adapted for a GDL in GDEs and corrosive protective materials on metal surface. Combining well-balanced properties of siloxane and fluorinated polymer chemistries, iCVD process is an excellent low-cost method for the fabrication of GDLs for metal-air battery applications. In addition, iCVD process enables fabrication of finely tuned fluorinated siloxane copolymer conformal coatings for corrosion protection on a variety of substrates.

REFERENCES

Aaron, D., Tang, Z., Papandrew, A.B., Zawodzinski, T.A. (2011). Polarization curve analysis of all-vanadium redox flow batteries. *Journal of Applied Electrochemistry*, 41, 1175-1182.

Achyuta, A.K.H., White, A.J., Lewis, H.G.P., Murthy, S.K. (2009). Incorporation of linear spacer molecules in vapor-deposited silicone polymer thin films. *Macromolecules, 42*, 1970-1978.

Adler, T.C., McLarnon, F.R., Cairns, E.J. (1993). Low-zinc-solubility electrolytes for use in zinc/nickel oxide cells, *Journal of Electrochemical Society*, 140, 289-294.

Allcock, H.R., Lampe, F.W., Mark, J.E. (2003). *Contemporary Polymer Chemistry*, Prentice Hall.

Amici, J., Francia, C., Zeng, J., Bodoardo, S., Penazzi, N. (2016a). Protective PVDF-HFP-based membranes for air de-hydration at the cathode of the rechargeable Li-air cell. *Journal of Applied Electrochemistry*, 46, 617- 626.

Amici, J., Alidoost, M., Francia, C., Bodoardo, S., Martines Crespiera, S., Amantia, D., Biasizzo, D., Caldera, F., Trotta, F. (2016b). O_2 selective membranes based on a dextrin-nanosponge (NS) in a PVDF-HFP polymer matrix for Li-air cells. *Chemical Communications,* 52, 13683-13686.

Amin, H.M.A., Baltruschat, H., Wittmaier, D., Friedrich, K.A. (2015). A highly efficient bifunctional catalyst for alkaline air-electrodes based on Ag and Co_3O_4 hybrid: RRDE and online DEMS insights. *Electrochimica Acta*, 51, 332-339.

Antolini, E., Giorgi, L., Pozio, A., Passalacqua, E. (1999). Influence of Nafion loading in the catalyst layer of gas-diffusion electrodes for PEFC. *Journal of Power Sources*, 77, 136-142.

Araújo, M.P., Nunes, M., Rocha, I.M., Pereira, M.F.R., Freir, C. (2019). Electrocatalytic activity of new Mn_3O_4@oxidized graphene flakes nanocomposites toward oxygen reduction reaction. *Journal of Materials Science*, 54, 8919-8940.

Arise, T.H.I., Mclarnon, F.R., Fukunaka, Y. (2011). Zinc surface morphological variations and ionic mass transfer rates in alkaline solution, *ECS Trans*sactions, 35, 3–9.

Ates, M. (2016). A review on conducting polymer coatings for corrosion protection. *Journal of Adhesion Science and Technology, 30*, 1510-1536.

Aurbach, D., McCloskey, B.D., Nazar, L.F., Bruce, P.G. (2016). Advances in understanding mechanisms underpinning lithium–air batteries. *Nature Energy*, 1, 1-11.

Baldo, L.G.M., Lenzi, M.K., Eiras, D. (2020). Water vapor permeation and morphology of polysulfone membranes prepared by phase inversion. *Polímeros*, 30, 1-8.

Banks, R.E., Smart, B.E., Tatlow, J. (1994). *Organofluorine Chemistry: Principles and Commercial Applications*, 1st ed. Springer, US.

Bayram, F., Mercan, E.S., Karaman, M. (2021). One-step fabrication of superhydrophobic-superoleophilic membrane by initiated chemical vapor deposition method for oil-water separation. *Colloid and Polymer Science*, 299, 1469-1477.

Braam, K.T., Volkman, S.K., Subramanian, V. (2012). Characterization and optimization of a printed, primary silver–zinc battery, *Journal of Power Sources*, 199, 367-372.

Bravo, J., Zhai, L., Wu, Z.Z., Cohen, R.E., Rubner, M.F. (2007). Transparent superhydrophobic films based on silica nanoparticles. *Langmuir*, 23:7293-7298.

Bursell, M., Björnbom, P. (1990). A method for studying microelectrodes by means of micromanipulators as applied to carbon agglomerates from oxygen reduction electrode catalyst. *Journal of the Electrochemical Society*, 137, 363.

Cakmakcı, I., Duran, B., Duran, M., Bereket, G. (2013). Experimental and theoretical studies on protective properties of poly(pyrrole-co-N-methyl pyrrole) coatings on copper in chloride media. *Corrosion Science, 69*, 252-261.

Caldona, E.B., Smith, D.W., Wipf, D.O. (2020). Protective action of semi-fluorinated perfluorocyclobutyl polymer coatings against corrosion of mild steel. *Journal of Materials Secience, 55*, 1796-1812.

Cao, L., Lv, F., Liu, Y., Wang, W., Huo, Y., Fu, X., Sun, R., Lu, Z. (2015). A high performance O_2 selective membrane based on CAU-1-NH_2@polydopamine and the PMMA polymer for Li-air batteries. *Chemical Communications, 51*, 4364-4367.

Cao, N., Miao, Y.Y., Zhang, D.L., Boukherroub, R., Lin, X.G., Ju, H., Li, H.P. (2018). Preparation of mussel-inspired perfluorinated polydopamine film on brass substrates: Superhydrophobic and anti-corrosion application. *Progress in Organic Coatings*, *125*(12), 109-118.

Chambers, L.D., Stokes, K.R., Walsh, F.C., Wood, R.J.K. (2006). Modern approaches to marine antifouling coatings. *Surface and Coatingd Technology, 201*(6), 3642-3652.

Chan, K., Gleason, K.K. (2005). Initiated chemical vapor deposition of linear and cross-linked poly(2-hydroxyethyl methacrylate) for use as thin-film hydrogels. *Langmuir, 21*, 8930-8939.

Chang, Y.Q., Dong, S.M., Ju, Y.H., Xiao, D.D., Zhou, X.H., Zhang, L.X., Chen, X., Shang, C.Q., Gu, L., Peng, Z.Q., Cui, G.L. (2015). A carbon- and binder-free nanostructured cathode for high-performance nonaqueous Li-O_2 battery. *Advanced Science*, 2, 1500092.

Chatman, H. (1996). Oxygen diffusion barrier properties of transparent oxide coatings on polymeric substrates, *Surface & Coatings Technology*, 78, 1-9.

Chen, L.D., Nørskov, J.K., Luntz, A.C. (2015). Theoretical limits to the anode potential in aqueous Mg-Air batteries, *Journal of Physical Chemistry C*, 119, 34, 19660-19667.

Chen, Y., Ye, Y.M., Chen, Z.R. (2019). Vapor-based synthesis of bilayer anti-corrosion polymer coatings with excellent barrier property and superhydrophobicity. *Journal of Materials Science*, 54(5), 5907-5917.

Cherian, C.T., Sundaramurth, J., Reddy, M.V., Kumar, P.S., Mani, K., Pliszka, D., Sow, C.H., Chowdari, B.V.R. (2013). Morphologically robust $NiFe_2O_4$ nanofibers as high capacity li-ıon battery anode material. *ACS Applied Materials & Interfaces*, 5(20), 9957–9963.

Choi, H.G., Shah, A.A., Nam, S.E., Park, Y.I., Park, H. (2019). Thin-film composite membranes comprising ultrathin hydrophilic polydopamine interlayer with graphene oxide for forward osmosis. *Desalination*, 449, 41-49.

Choi, W., Shin, H.C., Kim, J.M., Choi, J.Y., Yoon, W.S. (2020). Modeling and applications of electrochemical impedance spectroscopy (EIS) for lithium-ion batteries. *Journal of Electrochemical Science and Technology*, 11, 1-13.

Chunder, A., Etcheverry, K., Londe, G., Cho, H.J., Zhai, L. (2009). Conformal switchable superhydrophobic/hydrophilic surfaces for microscale flow control. *Colloid Surfaces A: Physicochemical Engineering Aspects,* 333(1-3), 187-193.

Cihanoğlu, G., Ebil, O. (2021) Robust fluorinated siloxanecopolymers via initiated chemical vapor deposition for corrosion protection, *Journal of Materials Science*, 56 (20), 11970-11987.

Clark, S., Latz, A., Horstmann, B. (2018). A review of model-based design tools for metal-air batteries, *Batteries,* 4, 1-26.

Clark, S., Mainar, A.R., Iruin, E., Colmenares, L.C., Blázquez, J. A., Tolchard, J. R., Latz, A., Horstmann, B. (2019). Towards rechargeable zinc-air batteries with aqueous chloride electrolytes, *Journal of Materials Chemisrty A*, 7, 11387-11399.

Clark, S., Mainar, A.R., Iruin, E., Colmenares, L.C., Blázquez, J.A., Tolchard, J.R., Jusys, Z., Horstmann, B. (2020). Designing aqueous organic electrolytes for zinc-air batteries: Method, simulation, and validation. *Advanced Energy Materials,* 1903470, 1-14.

Clark, S., Latz, A., Horstmann, B. (2017). Rational development of neutral aqueous electrolytes for zinc-air batteries, *ChemSusChem*, 10, 4735-4747.

Coclite, A.M., Ozaydin-Ince G., d'Agostino, R., Gleason, K.K. (2009). Flexible cross-linked organosilicon thin films by initiated chemical vapor deposition. *Macromolecules,* 42*,* 8138-8145.

Crowther, O., Meyer, B., Morgan, M., Salomon, M. (2011). Primary Li-air cell development. *Journal of Power Sources, 196*, 1498–1502.

Crowther, O., Salomon, M. (2012). Oxygen selective membranes for Li-Air (O_2) batteries. *Membranes*, *2*, 216-227.

Davydova, E.S., Atamanyuk, I.N., Ilyukhin, A.S., Shkolnikov, E.I., Zhuk, A.Z. (2016). Nitrogen-doped carbonaceous catalysts for gas diffusion cathodes for alkaline aluminum-air batteries. *Journal of Power Sources*, 306, 329-336.

Duan, B., Guo, Z., Tamirat, A.G., Ma, Y., Wang, Y., Xia, Y. (2017). Crab-shell induced synthesis of ordered macroporous carbon nanofiber arrays coupled with $MnCo_2O_4$ nanoparticles as bifunctional oxygen catalysts for rechargeable Zn–Air batteries, *Nanoscale*, 9, 11148.

Emarati, S.M., Mozammel, M. (2020). Theoretical, fundamental and experimental study of Liquid-repellency and corrosion resistance of fabricated superamphiphobic surface on Al alloy 2024. *Chemical Engineering Journal,* 387, 124046.

Feliu, S.J. (2020). Electrochemical impedance spectroscopy for the measurement of the corrosion rate of magnesium alloys: Brief review and challenges. *Metals,* 10, 775(1-22).

Flegler, A., Hartmann, S., Settelein, J., Mandel, K., Sextl, G. (2017). Screen Printed bifunctional gas diffusion electrode for aqueous metal-air batteries: Combining the best of the catalyst and binder world. *Electrochimica Acta*, 258, 495-503.

Franzen, D., Ellendorff, B., Paulisch, M. C., Hilger, A., Osenberg, M., Manke, I., Turek, T. (2019). Influence of binder content in silver-based gas diffusion electrodes on pore system and electrochemical performance. *Journal of Applied Electrochemistry*, 49, 705-713.

Fu, J., Cano, Z.P., Park, M.G., Yu, A., Fowler, M., Chen, Z. (2017a). Electrically rechargeable Zinc-Air batteries: Progress, challenges, and perspectives, *Advanced Materials,* 29, 1604685.

Fu, G., Cui, Z., Chen, Y., Xu, L., Tang, Y., Goodenough, J.B. (2017b). Hierarchically mesoporous nickel-iron nitride as a cost-efficient and highly durable electrocatalyst for Zn-Air battery, *Nano Energy*, 39, 77.

Fu, Z., Wei, Z., Lin, X., Huang, T., Yu, A. (2012). Polyaniline membranes as waterproof barriers for lithium air batteries. *Electrochimica Acta*, *78*, 195-199.

Gedde, U.W. (1999). *Polymer Physics*, 1st ed. Springer, Netherlands.

Geng, D., Ding, N., Hor, T.S.A., Chien, S.W., Liu, Z., Wuu, D., Sun, X., Zong, Y. (2016). From lithium-oxygen to lithium-air batteries: Challenges and opportunities. *Advanced Energy Materials,* 6, 1502164.

Geng, M. (2003). Development of advanced rechargeable Ni/MH and Ni/Zn batteries. *International Journal of Hydrogen Energy,* 28, 633-636.

Gilbert, R., Nguyen, H.P., Jalbert, J., Charbonneau, S. (2004). Transport properties of a mixture of permanent gases and light hydrocarbons through the polytetrafluoroethylene capillary tubes of a Gp-100 gas extractor. *Journal Membrane Science*, 236, 153-161.

Giorgi, L., Antolini, E., Pozioa, A., Passalacqua, E. (1998). Influence of the PTFE content in the diffusion layer of low-Pt loading electrodes. *Electrochimica Acta*, 43, 3675-3680.

Gleason, K.K. (2015). *CVD Polymers: fabrication of organic surfaces and devices*, 2nd ed. Wiley-VCH, Germany.

Goksel, Y., Akdogan, Y. (2019). Increasing spontaneous wet adhesion of DOPA with gelation characterized by EPR spectroscopy. *Materials and Chemistry Physics* 228, 124-130.

Graham, P., Stone, M., Thorpe, A., Nevell, T.G., Tsibouklis, J. (2000). Fluoropolymers with very low surface energy characteristics. *Journal of Fluorine Chemistry, 104*(1), 29-36.

Grignard, B., Vaillant, A., Coninck, J., Piens, M., Jonas, A.M., Detrembleur, C., Jerome, C. (2011). Electrospinning of a functional perfluorinated block copolymer as a powerful route for imparting superhydrophobicity and corrosion resistance to aluminum substrates. *Langmuir, 27*, 335-342.

Gu, P., Zheng, M., Zhao, Q., Xiao, X., Xue, H. Pang, H. (2017). Rechargeable Zinc–Air batteries: A promising way to green energy. *Journal of Materials Chemistry A*, 5, 7651-7666.

Gupta, M., Gleason, K.K. (2006). Initiated chemical vapor deposition of poly(1H,1,H,2H,2H-perfluorodecly acrylate) thin films. *Langmuir,* 22, 10047-10052.

Gupta, M., Kapur, V., Pinkerton, N.M., Gleason, K.K. (2008). Initiated Chemical Vapor (iCVD) of conformal polymeric nanocoatings for the surface modification of high-aspect-ratio pores. *Chemistry of Materials*, 20, 1646-1651.

Gupta, M., Gleason, K.K. (2009). Surface modification of high aspect ratio structures with fluoropolymer coatings using chemical vapor deposition. *Thin Solid Film*, 517, 3547-3550.

Han, D.W., Steckl, A.J. (2009). Superhydrophobic and oleophobic fibers by coaxial electrospinning. *Langmuir,* 25, 9454-9462.

Han, G., Jiang, P., Wang, J., Yan, F. (2016). Effect of NaCl concentration on wear-corrosion beviour of SAF 2507 super duplex stainless steel. *RCS Advances,* 6, 111261-111268.

Hao, Y., Xu, Y., Han, N., Liu, J., Sun, X. (2017). Boosting the bifunctional electrocatalytic oxygen activities of CoO_x nanoarrays with a porous N-doped carbon coating and their application in Zn–Air batteries. *Journal of Materials Chemistry A*, 5, 17804.

Harting, K., Kunz, U., Turek T. (2012). Zinc-Air batteries: Prospects and challenges for future improvement. *Zeitschrift für Physikalische Chemie*, 226, 151–166.

He, Y.L., Walsh, D., Shi, C. (2015). Fluoropolymer composite coating for condensing heat exchangers: Characterization of the mechanical, tribological and thermal properties. *Applied Thermal Engineering,* 91, 387-398.

Hosseini, S., Lao-Atiman, W., Han, S.J., Arpornwichanop, A., Yonezawa, T., Kheawhom, S. (2018). Discharge performance of zinc-air flow batteries under the effects of sodium dodecyl sulfate and pluronic F-127. *Scientific Report*, 8, 14909, 1-12.

Hsu, C.H., Mansfeld, F. (2001). Technical Note: Concerning the conversion of the constant phase element parameter Y_o into a capacitance. *Corrosion-Houston Tx* 57, 747-748.

Huang, H., Zhang, L., Zhang, W.K., Gan, Y.P., Shao, H. (2008). Preparation and electrochemical properties of ZnO/Conductive-ceramic nanocomposite as anode material for Ni/Zn rechargeable battery. *Journal of Power Sources*, 184(2), 663-667.

Huang, Y., Sarkar, D.K., Chen, X.G. (2015). Superhydrophobic aluminum alloy surfaces prepared by chemical etching process and their corrosion resistance properties. *Applied Surface Science,* 356, 1012-1024.

Ikezawa, A., Seki, K., Arai, H. (2021). Design of bifunctional air electrodes based on the reaction fields between oxygen reduction reaction and oxygen evolution reaction. *Electrochimica Acta,* 394, 139128 (1-10).

Ikhe, A.B., Kale, A.B., Jeong, J., Reece, M.J., Choi, S.H., Pyo, M. (2016). Perfluorinated polysiloxane hybridized with graphene oxide for corrosion inhibition of AZ31 magnesium alloy. *Corrosion Science,* 109, 238-245.

Indayaningsih, N., Zulfia, A., Priadi D., Hendrana, S. (2016). Preparation of carbon composite from coconut fiber for gas diffusion layer. *Ionics*, 1-5.

Ishizaki, T., Hieda, J., Saito, N., Saito, N., Takai, O. (2010). Corrosion resistance and chemical stability of super-hydrophobic film deposited on magnesium alloy AZ31 by microwave plasma-enhanced chemical vapor deposition. *Electrochimica Acta,* 55, 7094-7101.

Ito, Y., Nyce, M., Plivelich, R., Klein, M., Steingart, D., Banerjee, S. (2011). Zinc morphology in zinc–nickel flow assisted batteries and impact on performance. *Journal of Power Sources,* 196(4), 2340-2345.

Iwakura, C., Murakami, H., Nohara, S., Furukawa, N., Inoue, H. (2005). Charge–discharge characteristics of nickel/zinc battery with polymer hydrogel electrolyte. *Journal of Power Sources,* 152, 291-294.

ISO 8407:2009 (2009). *Corrosion of Metals and Alloys-Removal of Corrosion Products from Corrosion Test Specimens*.

Jeong, H.E., Kwak, M.K., Park, C.I., Suh, K.Y. (2009). Wettability of nanoengineered dual-roughness surfaces fabricated by UV-assisted capillary force lithography. *Journal of Colloid Interface Science,* 339(1), 202-207.

Jiang, J., Rajagopalan, K. (2011). Oxygen reduction reaction on a mini gas diffusion electrode. *Electrochimica Acta*, 58, 717-722.

Johnson, L., Li, C., Liu, Z., Chen Y., Freunberger, S.A., Tarascon, J.M., Ashok, P.C., Praveen, B.B., Dholakia, K., Bruce, P.G. (2014). The role of LiO_2 solubility in O_2 reduction in aproticsolvents and its consequences for Li-O_2 batteries. *Nature Chemistry*, 6, 1091-1099.

Jüttner, K. (1990). Electrochemical impedance spectroscopy (EIS) of corrosion processes on inhomogeneous surfaces. *Electrochimica Acta,* 35, 1501-1508.

Kaufman, F.B., Schroeder, A.H., Engler, E.M., Kramer, S.R., Chamber, J.Q. (1980). Ion and electron transport in stable, electroactive tetrathiafulvalene polymer coated electrodes. *Journal of American Chemical Society*, 102, 483–488.

Khairy, M., Mahmoud, B.G., Banks, C.E. (2018). Simultaneous determination of codeine and its co-formulated drugs acetaminophen and caffeine by utilizing cerium oxide nanoparticles modified screen-printed electrodes. *Sensors and Actuators, B: Chemical*, 259, 142-154.

Khamsanga, S., Pornprasertsuk, R., Yonezawa, T., Mohamad, A.A., Kheawhom, S. (2019). δ-MnO_2 nanoflower/graphite cathode for rechargeable aqueous zinc ion batteries. *Nature Science Report*, 9, 1-9.

Kim, H., Jeong, G., Kim, Y.U., Kim, J.H., Park, C.M., Sohn, H.J. (2013). Metallic anodes for next generation secondary batteries. *Chemical Society Reviews*, 42, 9011–9034.

Kim, J., Park, H., Lee, B., Seong, W.M., Lim, H.D., Bae, Y., Kim, H., Kim, W.K., Ryu, K.H., Kang, K. (2016). Dissolution and ionization of sodium superoxide in sodium oxygen batteries. *Nature Communications,* 7, 10670.

Kunst, S.R., Cardoso, H.R.P., Oliveira, C.T., Santana, J.A., Sarmento, V.H.V., Muller, I.L., Malfatti, C.F. (2014). Corrosion resistance of siloxane–poly(methyl methacrylate) hybrid films modified with acetic acid on tin plate substrates: Influence of tetraethoxysilane addition. *Applied Surface Science,* 298, 1-11.

Kwak, M.J., Oh, M.S., Yoo, Y., You, J.B., Kim, J., Yu, S.J., Im, S.G. (2015). Series of liquid separation system made of homogeneous copolymer films with controlled surface wettability. *Chemistry of Materials*, 27, 3441−3449.

Labbe, M., Clark, M. P., Abedi, Z., He, A., Cadien, K., Ivey, D. G. (2021). Atomic layer deposition of iron oxide on a porous carbon substrate via ethylferrocene and an oxygen plasma. *Surface and Coating Technology,* 421, 127390 (1-12)

Lau, K.K.S., Gleason, K.K. (2006). Initiated chemical vapor deposition (iCVD) of poly(alkyl acrylates): A kinetic model. *Macromolecules,* 39, 3695-3703.

Lee, H.S., Kim, H., Jeong H.L., Kwak, J.B. (2019). Fabrication of a conjugated fluoropolymer film using one-step iCVD process and its mechanical durability. *Coatings,* 9, 430 (1-9).

Lee, J.S., Kim, S.T., Cao, R., Choi, N.S., Liu, M., Lee, K.T., Cho, J. (2011). Metal–Air batteries with high energy density: Li–Air versus Zn–Air. *Advanced Energy Materials,* 1, 34-50.

Leivo, E., Wilenius, T., Kinos, T., Vuoristo, P., Mantyla, T. (2004). Properties of thermally sprayed fluoropolymer PVDF, ECTFE, PFA and FEP coatings. *Progress in Organic Coatings,* 49*,* 69-73.

Liang, J., Hu, Y.C., Wu, Y.Q., Chen, H. (2014). Facile formation of superhydrophobic silica-based surface on aluminum substrate with tetraethylorthosilicate and vinyltriethoxysilane as co-precursor and its corrosion resistant performance in corrosive NaCl aqueous solution. *Surface and Coatings Technology,* 240, 145-153.

Liang, T., Makita, Y., Kimura, S. (2001). Effect of film thickness on the electrical properities of polyimide thin films. *Polymer,* 42, 4867–4872.

Li, X.H., Ding, B., Lin, J.Y., Yu, J.Y., Sun, G. (2009). Enhanced mechanical properties of superhydrophobic microfibrous polystyrene mats via polyamide 6 nanofibers. *Journal of Physical Chemistry C,* 113, 20452-20457.

Li, C., Ji, W., Chen, J., Tao, Z. (2007). Metallic aluminum nanorods: Synthesis via vapor-deposition and applications in Al/Air batteries. *Chemistry of Mater*ilas, 19, 5812-5814.

Li, K., Zhang, J., Lin, D., Wang, D.W., Li, B., Lv, W., Sun, S., He, Y.B., Kang, F., Yang, Q.H., Zhou, L., Zhang, T.Y. (2019). Evolution of the electrochemical interface in sodium ion batteries with ether electrolytes. *Nature Communications*, 13, 725.

Li, L.F. (2010). *Non-toxic alkaline electrolyte with additives for rechargeable zinc cells*. U.S. Patent, US 2010/0062327 A1, March 11.

Lin, G., Nguyen, T.V. (2005). Effect of thickness and hydrophobic polymer content of the gas diffusion layer on electrode flooding level in a PEMFC. *Journal of Electrochemical Society*, 152, A1942-A1948.

Linden, D., Reddy, T.B. (2001). *Handbook of Batteries.* Mcgraw Hill, England.

Lim, H.K., Lim, H.D., Park, K.Y.,Seo, D.H., Gwon, H., Hong, J., Goddard, W.A., Kim, H., Kang, K. (2013). Toward a lithium-"air" battery: The effect of CO_2 on the chemistry of a lithium-oxygen cell. *Journal of the American Chemical Society*, 135, 9733-9742.

Liu, Q., Chen, D.X., Kang, Z.X. (2015). One-step electrodeposition process to fabricate corrosion-resistant superhydrophobic surface on magnesium alloy. *ACS Applied Materials & Interfaces,* 7(3), 1859-1867.

Liu, T., Chen, S., Cheng, S., Tian, J., Chang, X., Yin, Y. (2007). Corrosion behavior of super-hydrophobic surface on copper in seawater. *Electrochimica Acta,* 52, 8003–8007.

Liu, X., Ma, X., Wang, J., Liu, X., Chi, C., Liu, S., Zhao, J., Li, Y. (2016). The binder-free $Ca_2Ge_7O_{16}$ nanosheet/carbon nanotube composite as a high-capacity anode for Li-ion batteries with long cycling life. *RSC Advances*, 6, 107040.

Loveday, D., Peterson, P., Rodgers, B. (2004a). Evaluation of organic coatings with electrochemical Impedance Spectroscopy Part 1: Fundamentals of electrochemical impedance spectroscopy. *Journal of Coatings Technology and Research,* 1, 46-52.

Loveday, D., Peterson, P., Rodgers, B. (2004b). Evaluation of organic coatings with electrochemical impedance spectroscopy Part 2: Application of EIS to coatings. *Journal of Coatings Technology and Research,* 1, 88-93.

Loveday, D., Peterson, P., Rodgers, B. (2005). Evaluation of organic coatings with electrochemical impedance spectroscopy Part 3: Protocols for testing coatings with EIS. *Journal of Coatings Technology and Research,* 2, 22-27.

Lu, F., Wang, Y., Jin, C., Li, F., Yang, R., Chen, F. (2015). Microporous $La_{0.8}Sr_{0.2}MnO_3$ perovskite nanorods as efficient electrocatalysts for lithium-air battery. *Journal of Power Sources*, 293, 726-733.

Lu, Y.C., Kwabi, D.G., Yao, K.P.C., Harding, J.R., Zhou, J., Zuin, L., Shao-Horn, Y. (2011). The discharge rate capability of rechargeable Li-O_2 batteries. *Energy & Environmental Science*, 4, 2999.

Ma, M., Gupta, M., Li, Z., Zhai, L., Gleason, K.K., Cohen, R.E., Rubner, M.F., Rutledge, G.C. (2007). Decorated electrospun fibers exhibiting superhydrophobicity. *Advanced Materials*, 19, 255-259.

Ma, Z., Yuan, X., Li, L., Ma, Z.F., Wilkinson, D. P., Zhang, L., Zhang, J. (2015). A review of cathode materials and structures for rechargeable lithium-air batteries. *Energy & Environmental Science,* 8, 2144-2498.

Ma, M., Mao, Y., Gupta, M., Gleason, K.K., Rutledge, G.C. (2005). Superhydrophobic fabrics produced by electrospinning and chemical vapor deposition. *Macromolecules,* 38, 9742-9748.

Mao, Y., Gleason, K.K. (2006). Vapor-deposited fluorinated glycidyl copolymer thin films with low surface energy and improved mechanical properties. *Macromolecules*, 39, 3895-3900.

Mahadik, S.A., Pedraza, F., Vhatkar, R.S. (2016). Silica based superhydrophobic coating for long-term industrial and domestic applications. *Journal of Alloys and Compounds,* 663, 487-493.

Mainar, A.R., Colmenares, L.C., Blázquez, J.A., Urdampilleta, I. (2017). A brief overview of secondary zinc anode development: The key of improving zinc-based energy storage systems. *International Journal of Energy Research,* 1-16.

Mainar, A.R., Iruin, E., Colmenares, L.C., Kvasha, A., Meatza, I., Bengoechea, M., Leonet, O., Boyano, I., Zhang, Z. (2018). An overview of progress in electrolytes for secondary zinc-air batteries and other storage systems based on zinc. *Journal of Energy Storage*, 15, 304-328.

Mainar, A.R., Leonet, O., Bengoechea, M., Boyano, I., Meatza, I., Kvasha, A., Guerfi, A., Blázquez, J.A. (2016). Alkaline aqueous electrolytes for secondary zinc–air batteries: an overview. *International Journal of Energy Research*, 40, 1032–1049.

Martines, E., Seunarine, K., Morgan, H., Gadegaard, N., Wilkinson, C.D.W., Riehle, M.O. (2005). Superhydrophobicity and superhydrophilicity of regular nanopatterns. *Nano Letters,* 5(10), 2097-2103.

Meng, Y., Liu, L., Zhang, D., Dong, C., Yan, Y., Volinsky, A.A., Wang, L.N. (2019). Initial formation of corrosion products on pure zinc in saline solution. *Bioactive Materials,* 4, 87–96.

Mladenova, E., Slavova, M., Mihaylova-Dimitrova, E., Burdin, B., Abrashev, B., Krapchanska, M., Raikova, G., Vladikova, D. (2021). Monolithic carbon-free gas diffusion electrodes for secondary metal-air batteries. *Journal of Electroanalytical Chemistry,* 887, 115112.

Munekata, S. (1988). Fluoropolymers as coating material. *Progress in Organic Coatings* 16*,* 113-134.

Nabe, A., Staude, E., Belfort, G. (1997). Surface modification of polysulfone ultrafiltration membranes and fouling by BSA solutions. *Journal of Membrane Science*, 133, 57-72.

Nautiyal, A., Qiao, M.Y., Cook, J.E., Zhang, X.Y., Huang, T.S. (2018). High performance polypyrrole coating for corrosion protection and biocidal applications. *Applied Surface Science,* 427, 922-930.

Nestoridi, M., Pletcher, D., Wood, R.J.K., Wang, S., Jones, R.L., Stokes, K.R., Wilcock, I. (2008). The study of aluminium anodes for high power density Al/Air Batteries with brine electrolytes. *Journal of Power Sources*, 178, 445–455.

Nicodemo, L., Marcone, A., Monetta, T., Mensitieri, G., Bellucci, F. (1992). Transport of water dissolved oxygen in polymers via electrochemical technique. *Journal Membrane Science*, 70, 207-215.

Nishimoto, S., Sawai, Y., Kameshima, Y., Miyake, M. (2014). Underwater superoleophobicity of TiO_2 nanotube arrays. *Chemistry Letters,* 43(4), 518-520.

Onoe, H., Matsumoto, K., Shimoyama, I. (2004). Three-dimensional micro-self-assembly using hydrophobic interaction controlled by self-assembled monolayers. *Journal of Microelectromechanical Systems,* 13, 603-611.

Opitz, M., Yue, J., Wallauer, J., Smarsly, B., Roling, B. (2015). Mechanisms of charge storage in nanoparticulate TiO_2 and $Li_4Ti_5O_{12}$ anodes new insights from scan rate-dependent cyclic voltammetry. *Electrochimica Acta,* 168, 125-132.

O'Shaughnessy, W.S., Gao, M.L., Gleason, K.K. (2006). Initiated chemical vapor deposition of trivinyltrimethylcyclotrisiloxane for biomaterial coatings. *Langmuir* 22, 7021-7026.

Ozpirin, M., Ebil, O. (2018). Transparent block copolymer thin films for protection of optical elements via chemical vapor deposition. *Thin Solid Films*, 660, 391–398.

Pan, J., Thierry, D., Leygraf, C. (1996). Electrochemical impedance spectroscopy study of the passive oxide film on titanium for implant application. *Electrochimica Acta* 41*,* 1143-1153.

Pan, J.; Xu, Y. Y.; Yang, H.; Dong, Z.; Liu, H., Xia, B. Y. (2018). Advanced architectures and relatives of air electrodes in Zn-Air batteries. *Advanced Science,* 5, 1700691.

Park, J.H., Sudarshan T.S. (2001). *Chemical Vapor Deposition* (1st Ed): ASM International, USA.

Park, S.B., Park, Y.I. (2012). Fabrication of gas diffusion layer (GDL) containing microporous layer using fluorinated ethylene prophylene (FEP) for proton

exchange membrane fuel cell (PEMFC). *International Journal of Precision Engineering and Manufacturing*, 13, 1145

Parker, T.C., Baechle, D., Demaree J.D. (2011). Polymeric barrier coatings via initiated chemical vapor deposition. *Surface & Coatings Technology*, 206, 1680-1683.

Pawar, P., Gaikwad, A.B., Patil, P.P. (2007). Corrosion protection aspects of electrochemically synthesized poly(o-anisidine-co-o-toluidine) coatings on copper. *Electrochimica Acta,* 52, 5958–5967.

Payer, G. (2014). *An Investigation of Electrochemical Stability of Zinc Electrodes for Battery Applications.* MSc. of Thesis, Izmir Institute of Technology, Turkey.

Payer, G., Ebil, O. (2016). Zinc electrode morphology evolution in high energy density nickel-zinc batteries. *Journal of Nanomaterials*, 2016, 1-9.

Pei, P., Wang, K., Ma, Z. (2014). Technologies for extending zinc–air battery's cyclelife: A review. *Applied Energy,* 128, 315-324.

Peng, Z., Freunberger, S.A., Chen, Y., Bruce, P.G. (2012). A reversible and higher-rate Li-O_2 battery. *Science*, 337, 563.

Polu, A.R., Kumar, R., Joshi, G.M. (2014). Effect of zinc salt on transport, structural, and thermal properties of peg-based polymer electrolytes for battery application. *Ionics*, 20, 675.

Qi, Z., Lefebvre, M.C., Pickup, P.G. (1998). Electron and proton transport in gas diffusion electrodes containing electronically conductive proton-exchange polymers. *Journal of Electroanalytical Chemistry*, 459, 9-14.

Rahman, M., A., Wang, X., Wen, C. (2013). High energy density metal-air batteries: A review. *Journal of Electrochemical Society*, 160, A1759-A1771.

Rajitha, K., Mohana, K.N. (2020). Application of modified graphene oxide - Polycaprolactone nanocomposite coating for corrosion control of mild steel in saline medium. *Materials Chemistry and Physics,* 241, 122050.

Ravishankar, H., Christy, J., Jegatheesan, V. (2018). Graphene Oxide (GO)-blended polysulfone (PSf) ultrafiltration membranes for lead ion rejection. *Membranes*, 8, 77-90.

Read, J., Mutolo, K., Ervin, M., Behl, W., Wolfenstine, J., Driedger, A., Foster, D. (2003). Oxygen transport properties of organic electrolytes and performance lithium/oxygen battery. *Journal of Electrochemical Society*, 150, A1351-A1356.

Redondo, M.I., Sánchez de la Blanca, E., García, M.V., González-Tejera, M.J. (2009). Poly(N-methyl pyrrole) electrodeposited on copper: Corrosion protection properties. *Progress in Organic Coatings*, 65, 386–391.

Rocha, R.S., Reis, R.M., Lanza, M.R.V., Bertazzoli, R. (2013). Electrosynthesis of methanol from methane: The role of V_2O_5 in the reaction selectivity for methanol of a $TiO_2/RuO_2/V_2O_5$ gas diffusion electrode. *Electrochimica Acta*, 87, 606–610.

Rocket, A. (2008). *The Materials Science of Semiconductors* (1st Ed): Springer, USA.

Roldughin, V.I., Vysotskii, V.V. (2000). Percolation properties of metal-filled polymer films, structure and mechanisms of conductivity. *Progress in Organic Coatings,* 39, 81–100.

Ruan, Y., Sun, J., Song, S., Yu, L., Chen, B., Li, W., Qin, X. (2018). A perfluorocarbon–silicone oil oxygen–selective membrane for ambient operation of aprotic Li–air batteries. *Electrochemistry Communications*, 96, 93-97.

Sadagopan, S., Muthukrishnan, S., Venkatachari, G., Trivedi, D.C. (2005). Corrosion protection of steel by polyaniline (PANI) pigmented paint coating. *Progress in Organic Coatings,* 53*,* 297–301.

Sahapatsombut, U., Cheng, H., Scott, K. (2014). Modelling of operation of lithium-air battery with ambient air and oxygen-selective membrane. *Journal of Power Sources*, 249, 418-430.

Sakai, R.T., Di L. da Cruz, F.M., Meloc, H.G., Benedetti, A.V., Santilli, C.V., Suegama, P.H. (2012). Electrochemical study of TEOS, TEOS/MPTS, MPTS/MMA and TEOS/MPTS/MMA films on tin coated steel in 3.5% NaCl solution. *Progress in Organic Coatings,* 74, 288-301.

Sasikumar, G., Ihm, J.W., Ryu, H. (2004). Dependence of optimum Nafion content in catalyst layer on platinum loading. *Journal of Power Sources*, 132, 11–17.

Scheirs, J. (1997). *Modern Fluoropolymers: High Performance Polymers for Diverse Applications.* 1st ed. John Wiley & Sons, Chichester, UK.

Schröder, D., Laue, V., Krewer, U. (2016). Numerical simulation of gas-diffusion-electrodes with moving gas-liquid interface: A study on pulse-current operation and electrode flooding. *Computers & Chemical Engineering*, 84, 217-225.

Semiletov, A.M., Chirkunov, A.A., Kuznetsov, Y.I. (2020). Protection of aluminum alloy AD31 from corrosion by adsorption layers of trialkoxysilanes and stearic acid. *Materials and Corrosion,* 71(1), 77-85.

Seok, J.H., Kim, S.H., Cho, S.M., Yi, G.R., Lee, J.Y. (2018). Crosslinked organosilicon-acrylate copolymer moisture barrier thin film fabricated by initiated Chemical Vapor Deposition (iCVD). *Macromolar Resources,* 26, 1257-1264.

Shao, Y., Ding, F., Xiao, J., Zhang, J., Xu, W., Park, S., Zhang, J.G., Wang, Y., Liu, J. (2013). Making Li-Air batteries rechargeable: Material challenges. *Advanced Functional Materials*, 23, 987–1004.

Shen, Y., Sun, D., Yu, L., Zhang, W., Shang, Y., Tang, H., Wu, J., Cao, A., Huang, Y. (2013). A high-capacity lithium–air battery with Pd modified carbon nanotube sponge cathode working in regular air. *Carbon*, 62, 288.

Shivkumar, R., Kalaignan, G. P., Vasudevan, T. (1995). Effect of additives on zinc electrodes in alkaline battery systems. *Journal of Power Sources*, 55, 53-62.

Slater, M. D., Kim, D., Lee, E., Johnson, C. S. (2013). Sodium ion batteries. *Advaced Functional Materials,* 23, 947.

Steele, A., Nayak, B.K., Davis, A., Gupta, M.C., Loth, E. (2013). Linear abrasion of a titanium superhydrophobic surface prepared by ultrafast laser microtexturing. J*ournal of Micromechanics and Microengineering,* 23(11), 115012.

Sumboja, A., Chen, J., Zong, Y., Lee, P.S., Liu, Z. (2017). NiMn layered double hydroxides as efficient electrocatalysts for the oxygen evolution reaction and their application in rechargeable Zn–Air batteries. *Nanoscale*, 9, 774.

Sun, S., Miao, H., Uue, Y., Wang, Q., Li, S., Liu, Z. (2016). Oxygen reduction reaction catalysts of manganese oxide decorated by silver nanoparticles for aluminum-air batteries. *Electrochimica Acta*, 214, 49-55.

Szostak, R. (1992). *Handbook of Molecular Sieves: Structures.* (1st Ed): Van Nostrand Reinhold, New York.

Tada, S., Privatananupunt, P., Iwasaki, T., Kikuchi, R. (2017). Gas diffusion electrode with large amounts of gas diffusion channel using hydrophobic carbon fiber: For oxygen reduction reaction at gas/liquid interfaces. *Journal of Electrochemical Energy Conversion and Storage,* 14, 020903-1-9.

Takechi, K., Shiga, T., Asaoka, T. (2011). A Li-O_2/CO_2 battery. *Chemical Communication*, 47, 3463-3465.

Toussaint, G., Stevens, P., Akrour, L., Rouget, R., Fourgeot, F. (2010). *Metal/Air and Metal/Water Batteries*. Vol. *28* (Ed: Dudney, N.), Electrochemical Soc. Inc., Pennington.

Trujillo, N.J., Baxamusa, S.H., Gleason, K.K. (2009). Grafted functional polymer nanostructures patterned bottom-up by colloidal lithography and initiated Chemical Vapor Deposition (iCVD). *Chemistry of Materials,* 21, 742-750.

Trujillo, N.J., Wu, Q.G., Gleason, K.K. (2010). Ultralow dielectric constant tetravinyltetramethylcyclotetrasiloxane films deposited by initiated chemical vapor deposition (iCVD). *Advanced Functional Materials,* 20, 607-616.

Tsibouklis, J., Graham, P., Eaton, P.J., Smith, J.R., Nevell, T.G., Smart, J.D., Ewen, R.J. (2000). Poly(perfluoroalkyl methacrylate) film structures: Surface organization phenomena, surface energy determinations, and force of adhesion measurements. *Macromolecules,* 33*,* 8460-8465.

Ugalde, A.R, Naguib, H.E. (2017). Double-layer membrane cathode with improved oxygen diffusivity in zinc-air batteries. *Energy Starage Materials*, 8, 1-9.

Wan, H., Mao, Y., Liu, Z., Bai, Q., Peng, Z., Bao, J., Wu, G., Liu, Y., Wang, D., Xie, J. (2017). Influence of enhanced O_2 provision on the discharge performance of Li–air batteries by incorporating fluoroether. *ChemSusChem*, 10, 1385.

Wang, K., Pei, P., M, Z., Xu, H., Li, P., and Wang, X. (2014). Morphology control of zinc regeneration for zinc-air fuel cell and battery. *Journal of Power Sources,* 271, 65-75.

Wang, N., Han, Z., Cao, X., Fu, J., Chen, Y., Xiong, D. (2021). Designing long-term cycle life for a lithium–air battery with a modified gas diffusion layer in terms of the moisture ıntrusion and electrolyte volatilization. *The Journal of Physical Chemistry C*, 125, 24787−24795.

Wang, Q.Y., Zhang, Q.H., Zhan, X.L., Chen, F.Q. (2010). Structure and surface properties of polyacrylates with short fluorocarbon side chain: Role of the main chain and spacer group. *Journal of Polymer Science Part A: Polymer Chemistry,* 48, 2584-2593.

Wijaya, O., Hartmann, P., Younesi, R., Markovits, I.I.E., Rinaldi, A., Janek, J., Yazami, R. (2015). A gamma fluorinated ether as an additive for enhanced oxygen activity in Li–O_2 batteries. *Journal of Materials Chemistry A*, 3, 1961.

Winckler, G.A.F., Reinhardt, M., Reinhar, O.K. (1953). *Cell*. U.S. Patent, 2,641,624, June 9.

Xie, M., Huang, Z., Lin, X., Li, Y., Huang, Z., Yuan, L., Shen, Y., Huang, Y. (2019). Oxygen selective membrane based on perfluoropolyether for Li-Air battery with long cycle life. *Energy Storage Materials*, 20, 307-314.

Xu, M., Ivey, D.G., Xie, Z., Qu, W. (2015). Rechargeable Zn-Air batteries: Progress in electrolyte development and cell configuration advancement. *Journal of Power Sources*, 283, 358-371.

Yang, M.K., French, R.H., Tokarsky, E.W. (2008). Optical properties of Teflon-AF amorphous fluoropolymers. *Journal of Microlithography Microfabrication and Microsystems,* 7(1), 1-9.

Yang, C.C., Yang, J.M., Wu, C.Y. (2009). Poly(vinyl alcohol)/poly(vinyl chloride) composite polymer membranes for secondary zinc electrodes. *Journal of Power Sources,* 191(2), 669-677.

Yang, R., Xu, J., Ozaydin-Ince, G., Wong, S.Y., Gleason, K.K. (2011). Surface-Tethered zwitterionic ultrathin antifouling coatings on reverse osmosis membranes by initiated chemical vapor deposition. *Chemistry of Materials*, 23, 1263-1272.

Yang, X.Y., Xu, J.J., Bao, D., Chang, Z.W., Liu, D.P., Zhang, Y., Zhang, X.B. (2017). High performance integrated self-package flexible Li-O_2 battery based on stable composite anode and flexible gas diffusion layer. *Advanced Materials*, 29, 1700378.

Yap, W.T., Doane, L.M. (1982). Determination of diffusion coeffcients by chronoamperometry with unshielded planar stationary electrodes. *Analaytical Chemistry*, 54, 1437-1439.

Yatagai, T., Ohkawa, Y., Kubo, D., Kawase, Y. (2016). Hydroxyl radical generation in electro-Fenton process with a gas-diffusion electrode: Linkages with electro-chemical generation of hydrogen peroxide and iron redox cycle. *Journal of Environmental Science and Health: Part A*, 52, 1-10.

Yin, X., Song, Y.Z., Liang, Z.Y., Zhang, B., Fang, L.F., Zhu, L.P., Zhu, B.K. (2017). Synthesis of sulfonyl fluorinated macro emulsifier for low surface energy emulsion polymerization application. *Journal of Applied Polymer Science,* 134, 1-9

Yoo, Y., You, J.B., Choi, W., Im, S.G. (2013). A stacked polymer film for robust superhydrophobic fabrics. *Polymer Chemistry,* 4, 1664-1671.

Yuan, Y.F., Tu, J.P., Wu, H.M., Li, Y., Shi, D.Q. (2005). Size and morphology effects of ZnO anode nanomaterials for Zn/Ni secondary batteries. *Nanotechnology*, 16(6), 803-808.

Zhang, G.Q., Zhang, X.G., Wang, Y.G. (2004). A new air electrode based on carbon nanotubes and Ag–MnO_2 for metal air electrochemical cells. *Carbon*, 42, 3097–3102.

Zhang, J., Xu, W., Liu W. (2010a). Oxygen-selective immobilized liquid membranes for operating of lithium-air batteries in ambient air. *Journal of Power Sources*, 195, 7438-7444.

Zhang, J.G., Wang, D., Xu, Xiao, J., Williford, R.E. (2010b). Ambient operation of Li/Air batteries. *Journal of Power Sources*, 195, 4332-4337.

Zhang, G.Q., Zheng, J.P., Liang, R., Zhang, C., Wang, B., Hendrickson, M., Plichta, E.J. (2010c). Lithium-air batteries using SWNT/CNF Bucky papers as air electrodes. *Journal of the Electrochemical Society*, 157, A953–A956.

Zhang, J., Xu, W., Li, X., Liu, W. (2010d). Air dehydration membranes for nonaqueous Lithium–Air batteries. *Journal of the Electrochemical Society*, 157, A940.

Zhang, Q.H., Wang, Q.Y., Zhan, X.L., Chen, F.Q. (2014a). Synthesis and performance of novel fluorinated acrylate polymers: Preparation and reactivity of short perfluoroalkyl group containing monomers. *Industrial & Engineering Chemistry Research, 53*, 8026-8034.

Zhang, T., Tao, Z., Chen, J. (2014b) Magnesium–air batteries: from principle to application. *Materials Horizons,* 1, 196-206.

Zhang, X.G. (1996). *Corrosion and Electrochemistry of Zinc.* Springer, New York.

Zhao, J., Wang, M., Jebutu, M.S., Zhu, M., Gleason, K.K. (2019). Fundamental nanoscale surface strategies for robustly controlling heterogeneous nucleation of calcium carbonate. *Journal of Material Chemistry A,* 7, 17242-17277.

Zhou, D.B., Vander Poorten, H. (1995). Electrochemical characterization of oxygen reduction on teflon-bonded gas diffusion electrodes. *Electrochimica Acta*, 40, 1819-1826.

Zhu, Q.C., Xu, S.M., Cai, Z.P., Harris, M.M., Wang, K.X., Chen, J.S. (2017a). Towards real Li-air batteries: A binder-free cathode with high electrochemical performance in CO_2 and O_2. *Energy Storage Materials*, 7, 209-215.

Zhu, J., Yang, J., Zhou, J., Zhang, T., Li, L., Wang, J., Nuli, Y. (2017b). A stable organic-inorganic hybrid layer protected lithium metal anode for long-cycle lithium-oxygen batteries. *Journal of Power Sources*, 366, 265–269.

Zhu, H.B., Hu, W.H., Zhao, S.P., Zhang, X., Pei, L., Zhao, G.Z., Wang, Z. (2020). Flexible and thermally stable superhydrophobic surface with excellent anti-corrosion behavior. *Journal of Material Science,* 55, 2215-2225.

Zhu, H.F., Hou, J., Qiu, R., Zhao, J., Xu, J.K. (2014). Perfluorinated lubricant/polypyrrole composite material: Preparation and corrosion inhibition application. *Journal of Applied Polymer Science,* 131, 40184(1-5).

Zhu, Q.C., Xu, S.M., Cai, Z.P., Harris, M.M., Wang, K.X., Chen, J.S. (2017a). Towards real Li-air batteries: A binder-free cathode with high electrochemical performance in CO_2 and O_2. *Energy Storage Materials*, 7, 209-215.

Zhu, J., Yang, J., Zhou, J., Zhang, T., Li, L., Wang, J., Nuli, Y. (2017b). A stable organic-inorganic hybrid layer protected lithium metal anode for long-cycle lithium-oxygen batteries. *Journal of Power Sources*, 366, 265–269.

APPENDIX A

PERMISSIONS TO REPRODUCE FIGURES AND TEXTS

Permission has been taken to reproduce the full text presented in Chapters 5 through the Copyright Clearance Center. Documentation of the approval is given on the following pages.

CHAPTER 5

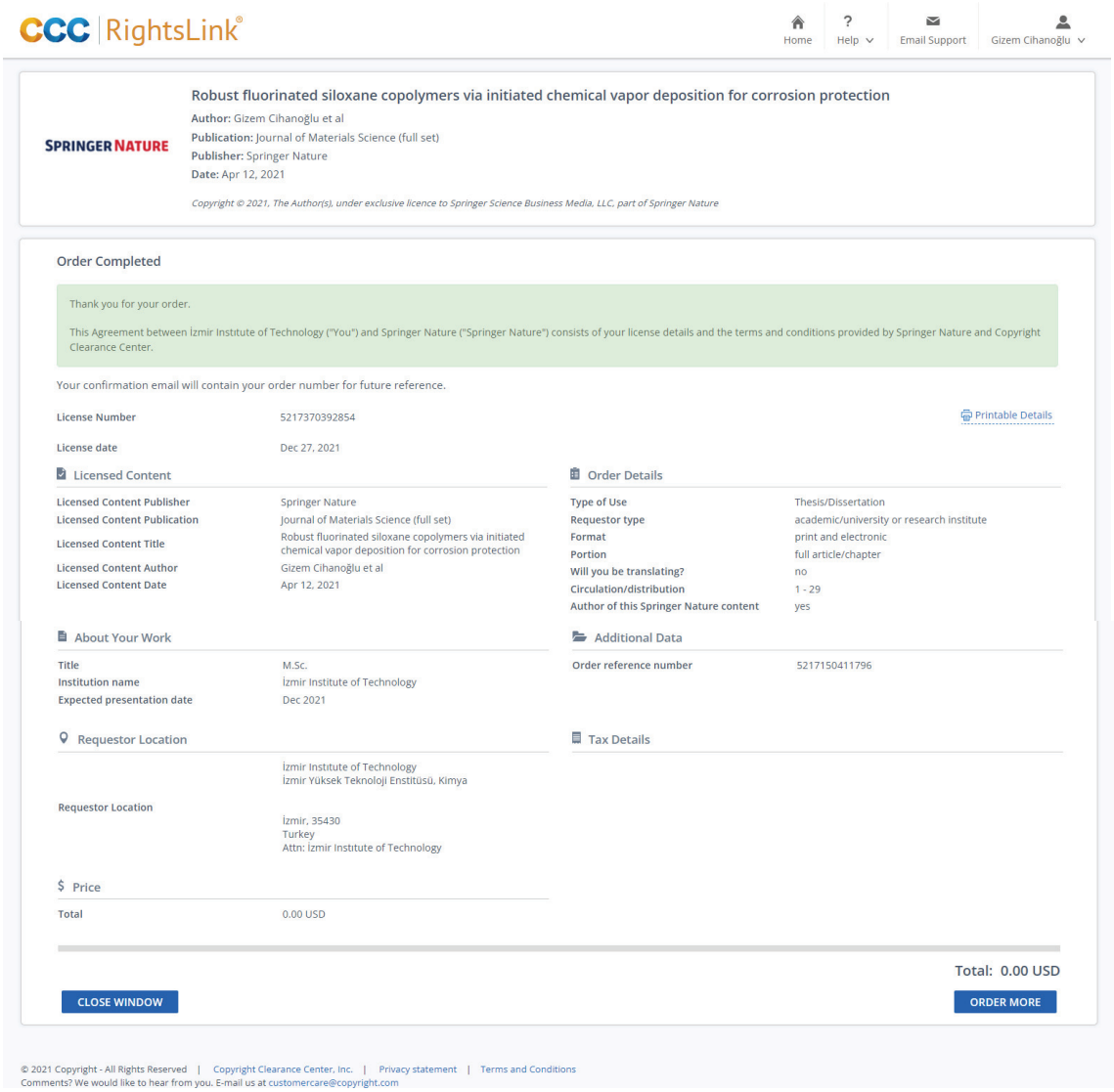

CCC | RightsLink®

Home | Help | Email Support | Gizem Cihanoğlu

SPRINGER NATURE

Robust fluorinated siloxane copolymers via initiated chemical vapor deposition for corrosion protection

Author: Gizem Cihanoğlu et al
Publication: Journal of Materials Science (full set)
Publisher: Springer Nature
Date: Apr 12, 2021

Copyright © 2021, The Author(s), under exclusive licence to Springer Science Business Media, LLC, part of Springer Nature

Order Completed

Thank you for your order.

This Agreement between İzmir Institute of Technology ("You") and Springer Nature ("Springer Nature") consists of your license details and the terms and conditions provided by Springer Nature and Copyright Clearance Center.

Your confirmation email will contain your order number for future reference.

Printable Details

License Number	5217370392854
License date	Dec 27, 2021

Licensed Content

Licensed Content Publisher	Springer Nature
Licensed Content Publication	Journal of Materials Science (full set)
Licensed Content Title	Robust fluorinated siloxane copolymers via initiated chemical vapor deposition for corrosion protection
Licensed Content Author	Gizem Cihanoğlu et al
Licensed Content Date	Apr 12, 2021

Order Details

Type of Use	Thesis/Dissertation
Requestor type	academic/university or research institute
Format	print and electronic
Portion	full article/chapter
Will you be translating?	no
Circulation/distribution	1 - 29
Author of this Springer Nature content	yes

About Your Work

Title	M.Sc.
Institution name	İzmir Institute of Technology
Expected presentation date	Dec 2021

Additional Data

Order reference number	5217150411796

Requestor Location

İzmir Institute of Technology
İzmir Yüksek Teknoloji Enstitüsü, Kimya

Requestor Location

İzmir, 35430
Turkey
Attn: İzmir Institute of Technology

Tax Details

$ Price

Total	0.00 USD

Total: 0.00 USD

CLOSE WINDOW | ORDER MORE

SPRINGER NATURE LICENSE
TERMS AND CONDITIONS

Dec 27, 2021

This Agreement between İzmir Institute of Technology -- Gizem Cihanoğlu ("You") and Springer Nature ("Springer Nature") consists of your license details and the terms and conditions provided by Springer Nature and Copyright Clearance Center.

License Number	5217150626633
License date	Dec 27, 2021
Licensed Content Publisher	Springer Nature
Licensed Content Publication	Journal of Materials Science (full set)
Licensed Content Title	Robust fluorinated siloxane copolymers via initiated chemical vapor deposition for corrosion protection
Licensed Content Author	Gizem Cihanoğlu et al
Licensed Content Date	Apr 12, 2021
Type of Use	Thesis/Dissertation
Requestor type	non-commercial (non-profit)
Format	print and electronic
Portion	full article/chapter
Will you be translating?	no
Circulation/distribution	1 - 29

VITA

Education

Ph.D.	Chemical Engineering, *Izmir Institute of Technology*, Izmir, Turkey *Thesis:* "Electrochemical And Oxygen/Water Permeation Behavior of Fluorinatedsiloxane Copolymers Synthesized via Initiated Chemical Vapor Depostion" *Advisor:* Assoc. Prof. Özgenç EBİL	2021
M.Sc.	Chemical Engineering, *Izmir Institute of Technology*, Izmir, Turkey *Thesis:* "An Investigation of Electrochemical Stability of Zinc Electrodes for Battery Applications" *Advisor:* Assoc. Prof. Özgenç EBİL	2014
B.S.	Chemical Engineering, *Yıldız Technical University*, Istanbul, Turkey *Senior thesis:* "The Production of Kefir Grains" *Advisor:* Prof. Dr. Belma KIN OZBEK	2010

Academic Experience

Research Assistant	Chemical Engineering, *Izmir Institute of Technology*, Izmir, Turkey	2013-2022 (8 years)

Honors and Awards

- The Honour Student of the Chemical Engineering Department, Yıldız Technical University, Istanbul, Turkey, 2010.
- TUBITAK 2224-International Scientific Meetings Fellowship Programme 2019/4.

Publications

- Cihanoglu G., Ebil O., *"*CVD Deposited Oxygen Selective Fluorinated Siloxane Copolymers as Gas Diffusion Layers", *Industrial & Engineering Chemistry Research* (revision).
- Cihanoglu G., Ebil O., *"*Robust Fluorinated Siloxane Copolymers via Initiated Chemical Vapor Deposition for Corrosion Protection"*, Journal of Materials Science*, 56 (2021) 11970-11987.
- Cihanoglu G., Ebil O., "Binder Effect on Electrochemical Performance of Zinc Electrodes for Nickel-Zinc Batteries", *Journal of the Turkish Chemical Society, Section A: Chemistry*, 5(sp.is. 1), (2017) 65-84.
- Payer G., Ebil O., "Zinc Electrode Morphology Evolution in High Energy Density Nickel-Zinc Batteries", *Journal of Nanomaterials*, 2016 (2016) 1-9.

❖ Demirhan E., Apar D.K., Payer G., Özbek B., "A Modelling Study on Kefir Grain Biomass Growth: Influence of Various Minerals*",* I*nternational Journal of Dairy Technology*, 64 (2011) 402-407.

Conferences

❖ Cihanoglu G., Ebil O., "*Fluorinated-O_2 Selective Membranes as Gas Diffusion Electrodes for Metal-Air Batteries*", 2019 MRS Fall Meeting Exhibit, December 1-6, 2019, Boston, Massachusetts.

❖ Cihanoglu G., Ebil O., "*Hydrophobic-O_2 Selective Membrane for Gas Diffusion Electrodes in Metal-Air Batteries*", e-MRS 2019 Fall Meeting, September 16-19, 2019, Warsaw, Poland.

❖ Cihanoglu G., Ebil O., "*Effect of Zn Electrode Morphology Change on NiZn Battery Performance*", e-MRS 2019 Fall Meeting, September 16-19, 2019, Warsaw, Poland.

❖ Aisel Ajalova, Aytaj Zeynalova, Cihanoglu G., Ebil O., "*Synthesis of Nickel Hydroxide Powder for Secondary Ni-Zn Batteries*", Electrochemistry Conference-2019 (Electrochem2019), September 30-October 2, 2019, Istanbul, Turkey.

❖ Cihanoglu G., Ebil O., "*Binder Effect on Electrochemical Performance of Zinc Electrodes for Nickel-Zinc Batteries*", International Porous Powders & Materials Symposium and Exhibition, September 12-15, 2017, Aydin, Turkey.

❖ Payer G., Ebil O., "*Investigation of Zinc Electrodes on NiZn Battery Performance*", 12th National Chemical Engineering Meeting, August 23-26, 2016, Izmir, Turkey.

❖ Ebil O., Payer G., Ocali O., "*Shape stabilized composite zinc electrode for secondary batteries*", 247th ACS National Meetings and Exposition, March 16-18, 2014 Dallas, Texas.

❖ Ebil O., and Payer G., "*Nanomembrane Based Fabrication Processes*", NanoTR VIII- 8th, Nanoscience and Nanotechnology Conference, June 22-29, 2012 Ankara, Turkey.

❖ Payer G., Apar D.K., Demirhan E. and Özbek B., "*Experimental Study on the Effect of Mg^{2+}, Zn^{2+}, Ca^{2+} and Fe^{3+} Ions on Kefir Grain Biomass Propagation*", European Biotechnology Congress 2011, September 28-October 1, 2011 Istanbul, Turkey.